Modeling of Lithium-ion Battery Considering Temperature and Aging Uncertainties

by

Xianzhi Gong

A dissertation submitted in partial fulfillment
of the requirements for the degree of
Doctor of Philosophy
(Automotive Systems Engineering)
in the University of Michigan-Dearborn
2016

Doctoral Committee:

Professor Chris Mi, Chair
Assistant Professor Wencong Su, Co-Chair
Professor Yi Lu Murphey
Assistant Professor Zhimin Xi

DEDICATION

This thesis is dedicated to my parents, Jinghong Bai and Ruijin Gong, to my wife, Yifei Lin, and to my son, Maxwell Junbo Gong.

ACKNOWLEDGMENTS

First and foremost, I wish to express my gratitude towards my advisor, Prof. Chris Mi. His astute mentorship, thoughtful guidance, and unwavering support is deeply appreciated. In particular, his ability to distill the important facts, find technical weaknesses and recommend creative solutions that are simply uncanny. More than anything else, Prof. Chris Mi always believed in me.

I am thankful to my committee members, Prof. Wencong Su, Prof. Yi Lu Murphey, and Zhimin Xi, for asking questions and providing helpful feedback. Their insightful advice has been crucial toward creating a solid foundation for the work in this dissertation.

All my colleagues in the DTE power electronics and motor drive laboratory deserve recognition for their mentorship and friendship during my doctoral studies. I thank Rui Xiong for his knowledge on battery experimental facilities. I thank Bing Xia and Sung-Yoon Jung for their support, technical discussions. I thank Junjun Deng for his great friendship and hospitality. I learned more from him than he could imagine. All my colleagues are my mentors, and this work would not be possible without them.

TABLE OF CONTENTS

LIST OF TABLES

LIST OF FIGURES

LIST OF ABBREVIATIONS

CC	Constant Current
BMS	Battery Management Systems
CV	Constant Voltage
EV	Electric Vehicle
PHEV	Plug-in Hybrid Electric Vehicle
EIS	Electrochemical Impedance Spectroscopy
HEV	Hybrid Electric Vehicle
PITT	Potentiostatic Intermittent Titration Technique
GITT	Galvanostatic Intermittent Titration Technique
UDDS	Urban Dynamometer Driving Schedule
SEI	Solid Electrolyte Interface
SOC	State-Of-Charge
SOH	State-Of-Health
USABC	United States Automotive Battery Consortium
EC	Ethylene Carbonate
OCV	Open Circuit Voltage
HPPC	Hybrid Pulse Power Characterization
ICA	Incremental Capacity Analysis
ICE	Internal Combustion Engine
CPE	Constant Phase Element

DOD	Depth Of Discharge
FUDS	Federal Urban Driving Schedule

LIST OF APPENDICES

ABSTRACT

This dissertation provides a systematic methodology for analyzing and solving the temperature and aging uncertainties in Li-ion battery modeling and states estimation in the electric vehicle applications. This topic is motivated by the needs of enhancing the performance and adaptability of battery management systems. In particular, temperature and aging are the most crucial factors that influence battery performance, modeling, and control.

First, the basic theoretical knowledge of Li-ion battery modeling and State of Charge (SoC) estimation are introduced. The thesis presents an equivalent circuit battery model based SoC estimation using Adaptive Extended Kalman Filter (AEKF) algorithm to solve the initial SoC problem and provide good estimation result.

Second, the thesis focuses on the understanding of the temperature-dependent performance of Li-ion battery. The temperature influence is investigated through Electrochemical Impedance Spectroscopy (EIS) tests to enhance the theoretical basis understanding and to derive model compensation functions for better model adaptability at different temperatures.

Third, the battery aging mechanisms are revisited first and then a series of aging tests are conducted to understand the degradation path of Lithium-ion battery. Moreover, the incremental capacity analysis (ICA) based State of Health (SoH) estimation method

are applied to track battery aging level and develop the bias correction modeling method for aged battery.

In the final phase, the study of parallel-connected battery packs is presented. The inconsistency problem due to different battery aging levels and its influence to parallel-connected packs are discussed. Based on simulation and experimental test results, it shows that the current difference in parallel connected cells is increased significantly at low SoC, despite the battery aging levels and the number of cells in parallel.

In total, this dissertation utilizes physics-based battery modeling and states estimation method to optimize battery management under temperature and aging uncertainties in electric vehicle applications. The unique contributions include developing analytical compensation functions to improve equivalent circuit battery model adaptability under temperature uncertainty and developing ICA based SoH estimation and battery modeling method to overcome aging uncertainty.

CHAPTER 1

Introduction

1.1 Background

The air pollution, global climate change and heavy demand on petroleum are major environmental issues caused by traditional internal combustion engine (ICE) based vehicles [45]. According to the 2013 annual energy report from the US Department of Energy (DoE), depicted in Fig. 1.1, the transportation consumes approximately one-third of the total energy in the US while gasoline-powered ICE vehicles occupy a considerable proportion in the transportation area [45].

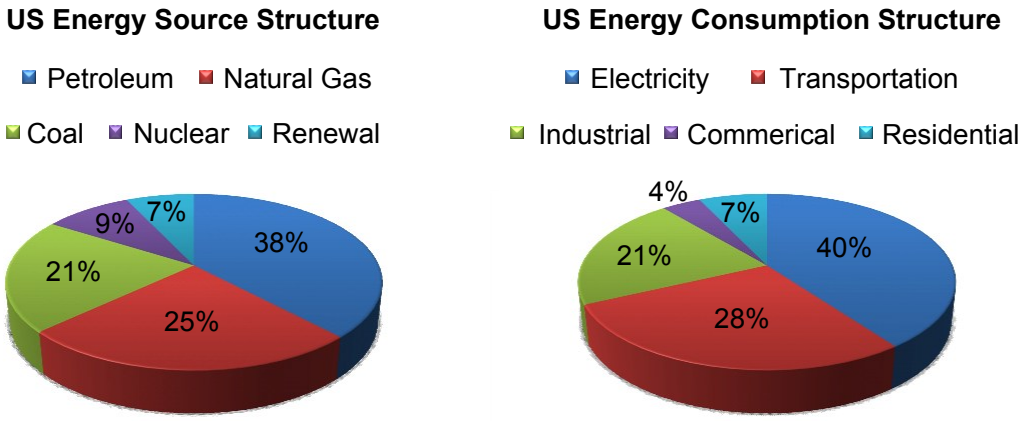

Figure 1.1 US energy source and consumption structures, 2013 [46]

Because of the inherent limitation in the traditional ICE vehicles, there are mainly two inevitable shortcomings which cause these environment issues mentioned above. First, the main energy sources of ICE vehicles are non-renewable fossil fuel, such as

gasoline, diesel, or nature gas. The fossil fuel combustions not only cause a huge amount of greenhouse gas emission but also result in serious air pollution due to impurities in the fossil fuel. Second, the operation efficiency of ICEs is poor due to the thermodynamic theoretical limitation. There are enormous difficulties to improve the efficiency while keeping the engine size small under current technology. As shown in Fig. 1.2, the highest efficiency ICE in the world, Wärtsilä-Sulzer RTA96-C diesel engine, only has a peak efficiency of 57% [47]. The efficiency of a typical vehicle used gasoline engine is lower than 40% [45]. To overcome these shortcomings, the electric drive system based vehicles (EVs) are considered as a feasible solution.

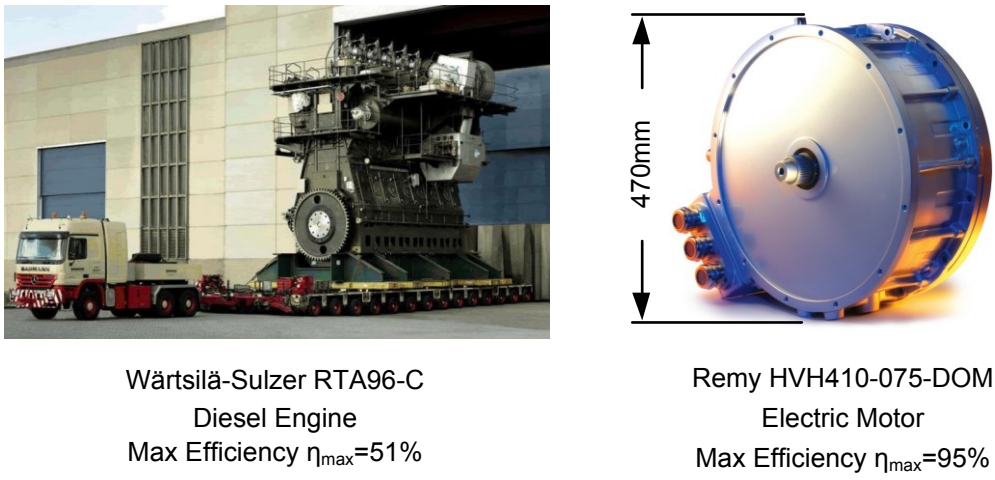

Figure 1.2 The highest efficiency ICE in the world (left) and a typical permanent magnet synchronous motor (PMSM) for EV application (right)

Invented by Serbian-American inventor Nikola Tesla in 1888, and as the core of electric drive system, the electric motor not only has superior performance in power

density and torque but also can maintain high efficiency in wide operation range, as shown in Fig. 1. 2. Thus, the transmission design of its associated electric drive system can be simplified and result in better reliability. Based on the operation principle of electric motors, electricity is the main energy form of EVs. Unlike fossil fuels, electric energy could be collected from multiple ways, including renewable sources such as solar power, wind power or hydropower [45].

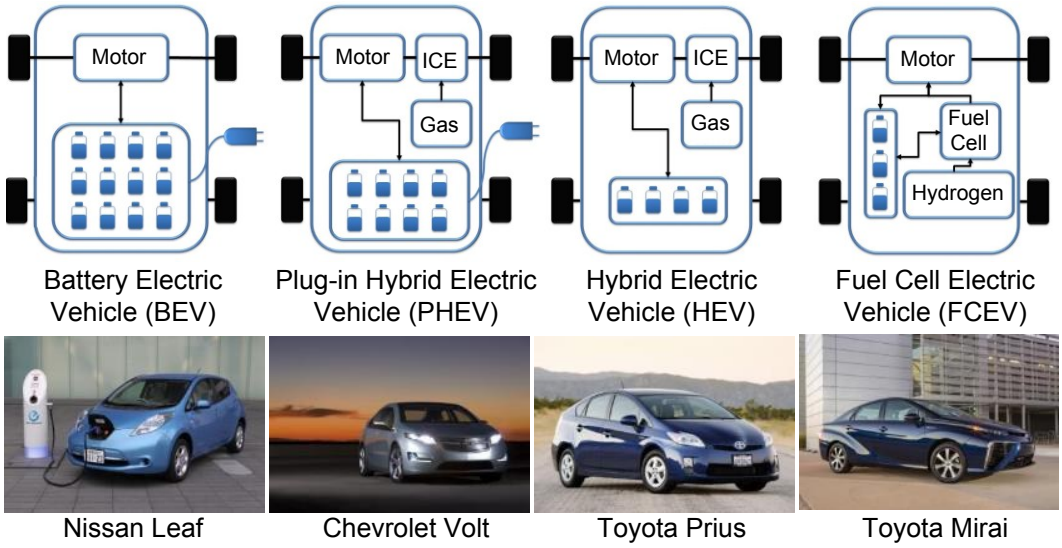

Figure 1.3 Comparison of various EVs and representative vehicles [50-52]

In general, EVs can be divided into four categories: pure battery electric vehicle (BEV), plug-in hybrid electric vehicle (PHEV) or extended-range electric vehicle (EREV), hybrid electric vehicle (HEV) and fuel cell electric vehicle (FCEV). As shown in Fig. 1.3, the battery is the major part in all types of EVs. A battery is a transducer that converts chemical energy into electrical energy and vice versa. In EV applications, the

battery has two major functions: Provide the electric energy to drive vehicles, and recycle the regenerative energy from vehicle braking. For HEVs, the ICE is used as the main power source, and the electric motor is used as the assist power to improve vehicle fuel efficiency. Typically, the battery in HEVs is used as an energy buffer, which cannot be charged from external power source. PHEVs/EREVs are developed on the basis of HEVs. They are equipped with high power electric motors which are capable of driving the vehicle alone, and high capacity battery which can be charged from external power sources, such as a household AC source or a high power DC charging station. FCEVs use hydrogen as the fuel to generate electric energy for electric motors. The function of the battery equipped in FCEVs is similar to HEVs'. For BEVs and PHEVs, the equipped batteries should be able to store a significant amount of energy, so that the mileage requirement of EVs/PHEVs can be satisfied.

There are mainly three types of batteries used in vehicles: Lead-acid battery, Nickel-metal hydride (NiMH) battery, and Li-ion battery. Lead-acid battery was invented in 1859 as the first rechargeable battery used in vehicles [51]. Advantages of the Lead-acid battery include low cost, high reliability, and anti-abuse ability. It has been well developed and widely used in vehicles as the engine-start power source. However, the energy density, power density, and lifetime of the Lead-acid battery are relatively low. Besides, the Lead-acid battery is composed of lead element and sulfuric acid electrolyte, which are toxic and harmful to the environment and human. NiMH battery has advantages of high power density and environmental friendly. It has been widely used in

HEVs, such as Toyota Prius and Honda Insight. The drawbacks of NiMH battery include low energy density, high self-discharge rate, and memory effect, which limit its application in BEVs and PHEVs.

Table 1.1 Comparison of Lead-acid, NiMH and Li-ion batteries

Items	Lead-acid battery	NiMH battery	Li-ion battery
Voltage (V)	2.0	1.2	3.3~3.7
Energy density (Wh/kg)	35~40	60~80	100~200+
Specific energy (Wh/L)	60~80	180~200	300~400+
Life time (cycles)	300~500	500~1000+	800~1500+
Self-discharge rate (%/month)	5~10%	10~30%	<3%
Memory effect	No	Yes	No
Anti-abuse	Excellent	Good	Fair
Environment friendly	Toxic	Yes	Yes
Cost	Low	Medium	High

From the comparison of three batteries shown in Table 1.1, at present, Li-ion battery is considered as the most suitable solution for energy storage in EVs. Compared with other batteries, Li-ion battery is the only battery meets to Freedom CAR goal set by the United States Council for Automotive Research (USABC) [52], as shown in Fig. 1.4. Advantages of Li-ion battery include high voltage, high energy density, long life, no memory effect and low self-discharge rate.

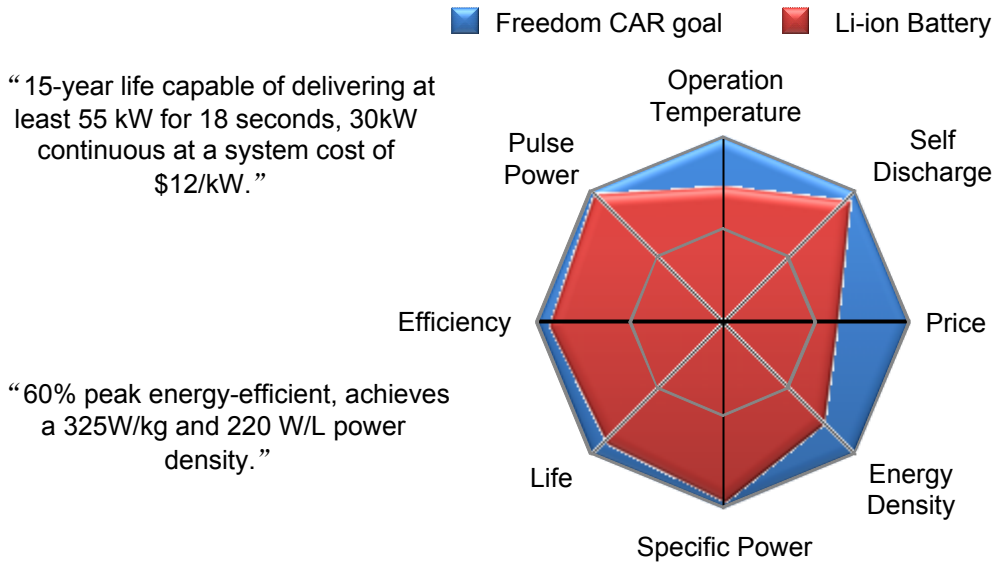

Figure 1.4 Status of Li-ion battery compared to the energy storage goals set up by FreedomCAR

1.2 Overview of Li-ion battery and its application in EVs

Lithium element has low density and the lowest potential to the standard hydrogen electrode. Its theoretical specific capacity is as high as 3861mAh/g [54-55]. Therefore, lithium based battery has been considered as an excellent energy storage solution for decades. In 1958, William Sidney Harris proposed the idea of a battery system based on lithium metal and a non-aqueous electrolyte in his Ph.D. thesis [53]. Based on his idea, several lithium metal batteries are developed, such as Li-SO_2 battery and Li-MnO_2 battery. However, during the charging process, the active lithium deposit on the surface of

electrodes to form the lithium dendrite, which may penetrate the separator and cause the short circuit. To solve this problem, the key is to avoid the deposition of lithium. Lithium intercalation compounds are selected as the electrode so that Lithium ions can quickly migrate into the electrode and prevent the deposition. Therefore, the Li-ion battery is also called Rocking Chair Battery to describe the behavior of ion transportation.

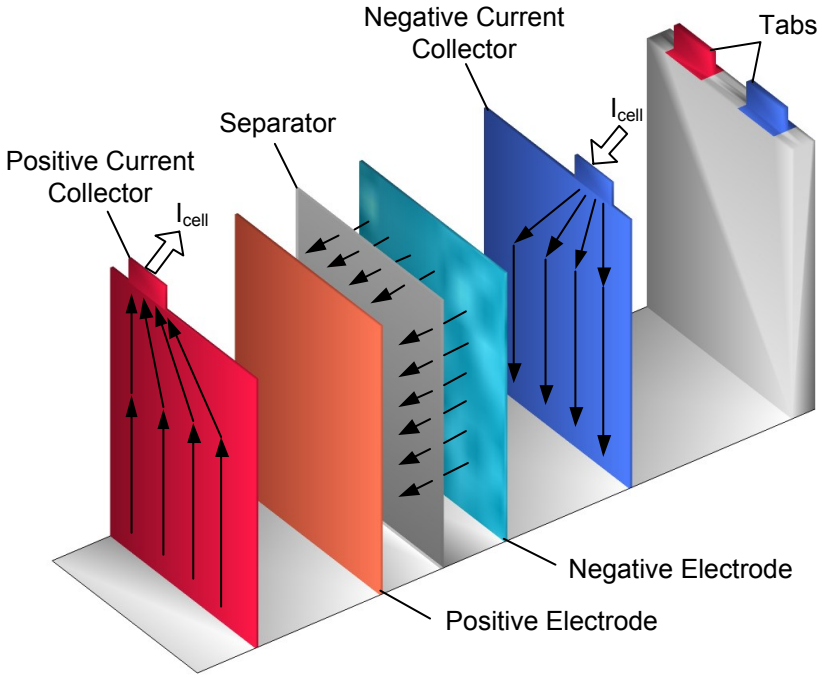

Figure 1.5 Structure of Laminated Li-ion Battery

In the 1980s, Goodenough research group discovered that LiCoO2 can be used as the positive electrode in Li-ion battery. Later on, the first commercial Li-ion battery was produced by Sony Company in 1991 [51]. This Li-ion battery consists of carbon graphite-based negative electrode, $LiCoO_2$-based positive electrode, and $LiFP_6$-based

electrolyte. The electrolyte acts as a good ionic conductor that provides a transport medium for Li-ions to travel from electrodes**.** For example, during the charging process, Li-ions de-insert from $LiCoO_2$ solid particles, and travel through the electrolyte solution to intercalate into LiC_6. Electrons are forced to follow an opposite path through an external circuit to form the current. The battery potential is determined by the difference between the chemical potential of the lithium in the anode and cathode, $\Delta G = -EF$. The reactions in electrodes can be described as:

$$LiCoO_2 \leftrightarrow Li_xCoO_2 + xLi^+ + xe^-$$

$$C_6 + xLi^+ + xe^- \leftrightarrow Li_xC_6$$

$LiCoO_2$ contains layered compounds with an anion close-packed lattice. Because of that, $LiCoO_2$ based Li-ion battery has an inherent advantage in energy stored per unit of volume. However, in the actual use, the specify energy of $LiCoO_2$ battery only reaches half of the ideal specify energy (270mAh/g). In 1999, Cho improved the specify energy to 170mAh/g by coating a metal oxide on the surface of $LiCoO_2$ particles [55]. Although $LiCoO_2$ battery has the advantage of superior energy density, the price of Cobalt is very high. Researchers and battery manufacturers develop the Cobalt based electrode with Nickel, Manganese and Aluminum doping to reduce the use of Cobalt. Typically, this kind of battery is called ternary Li-ion battery. Usually, the prefixed name is determined by the name of element doping. For example, if the positive electrode is composed of Nickel, Cobalt, and Manganese, we call this battery NCM Li-ion battery. The mass fraction of Cobalt in ternary Li-ion battery is around 20%; the entire cost is significantly

reduced. Other than $LiCo_2$, Goodenough research group also discovered that spinel lithium manganese oxide ($LiMn_2O_4$/LMO) and olivine lithium iron phosphate ($LiFePO_4$/LFP) can be used as the positive electrode in 1983 and 1996. These two materials have advantages of low cost, long life, and non-toxic, which draws lots of attention in both academic and industry area [56-57].

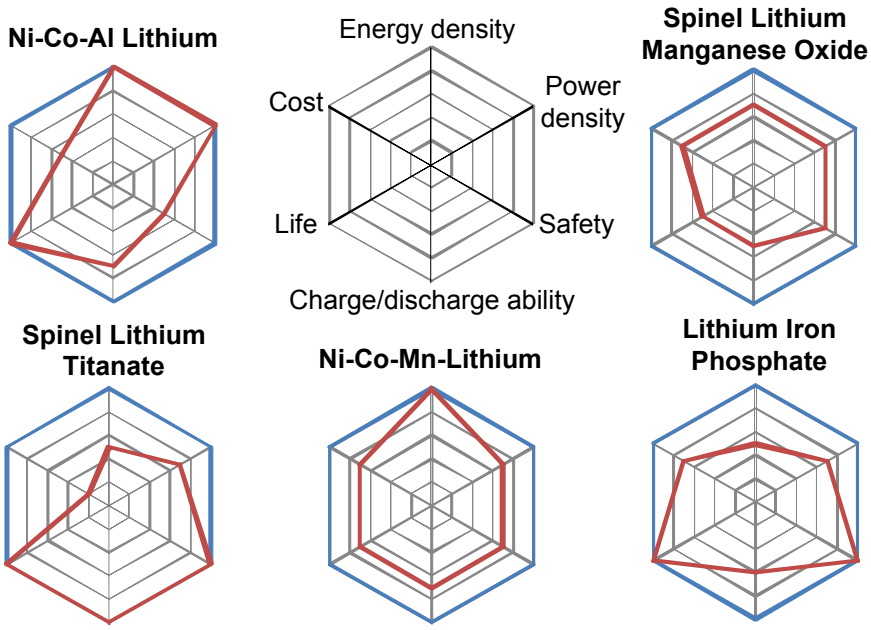

Figure 1.6 Comparison of different Li-ion batteries

For EV applications, the LMO, LFP, and Ternary Li-ion battery are widely used. For example, Nissan Leaf, Mitsubishi i-MiEV, Chevrolet Volt, Ford Focus EV, Hyundai Sonata Hybrid and others are equipped with the LMO based Li-ion battery [58-61]. The luxury EV Tesla Model S is equipped with 8142 NCA Li-ion battery cells [62]. The LFP battery has the lowest price and advantages in safety and lifetime. The Honda Accord

PHEV, Chevrolet Spark EV, Fisker Karma and BYD EVs are equipped with the LPF battery [63].

The high energy density of Li-ion battery is a two-edged sword. It causes the poor anti-abuse ability of Li-ion battery. Improper operations such as overcharge, over-discharge, overcurrent or operation at high/low environmental temperatures could significantly harm the Li-ion battery lifetime, even cause fire or explosion. Moreover, unlike other electronic devices equipped with Li-ion battery, such as laptop and cell phone, the operation environment of EV is very harsh. Therefore, a battery management system (BMS) is needed in EVs to manage the Li-ion battery properly and ensure the safety and reliable operation.

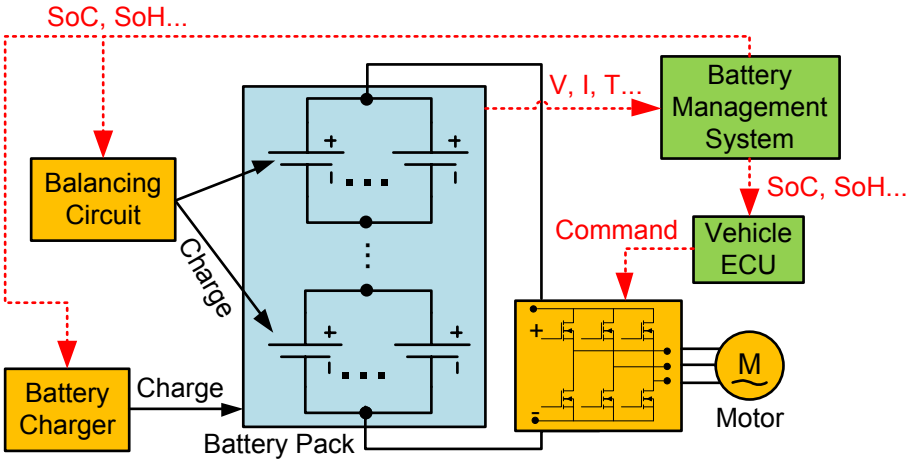

Figure 1.7 Main functions of battery management system

As shown in Fig. 1.7, the specific functions of a BMS include monitoring the voltage, current, temperature of each cell in the battery pack, and estimate battery states such as

the SoC, SoH. Additionally, BMS also controls the balancing circuit and the battery charger:

1. Voltage monitoring: Prevent overvoltage and under voltage.
2. Current monitoring: Control the maximum current and prevent short circuit.
3. Temperature monitoring: Prevent overheat and high-temperature gradient.
4. States estimation: Estimate the SoC, SoH based on the voltage, current and temperature information; send the estimation results to vehicle controller (ECU) and driver.
5. Balancing control: Control the balancing circuit and charger to minimize the inconsistency of individual cells based on the SoC estimation result and current.

From the functions listed above, the core task of a BMS is to estimate the internal states of the battery such as SoC and SoH. Due to the difficulty in direct measurement, the states estimation is based on the battery model and control algorithms in the BMS software, which is considered as one of the key technologies of EVs. In practice, incorrect SoC estimation usually results in high SoC variation of Li-ion battery, which may decrease vehicle lifetime and energy efficiency. Moreover, incorrect SoC also influences the drivers' decision on the vehicle acceleration and mileage performance. Incorrect SoH not only causes trouble in vehicle maintenance but also produce negative impacts on SoC estimation. Hence, reliable and accurate battery models are desired for estimation and control functionalities in the BMS.

1.3 Temperature and aging influence on Li-ion battery

As a complex electrochemical system, the performance of Li-ion battery can be influenced by multiple factors such as environmental temperature, driving pattern, and aging effect. Among these factors, temperature and aging effect are the two most crucial factors. With various levels of aging or temperatures, a fixed Li-ion battery model and states estimation algorithm may not be able to predict the behavior and provide estimation result correctly.

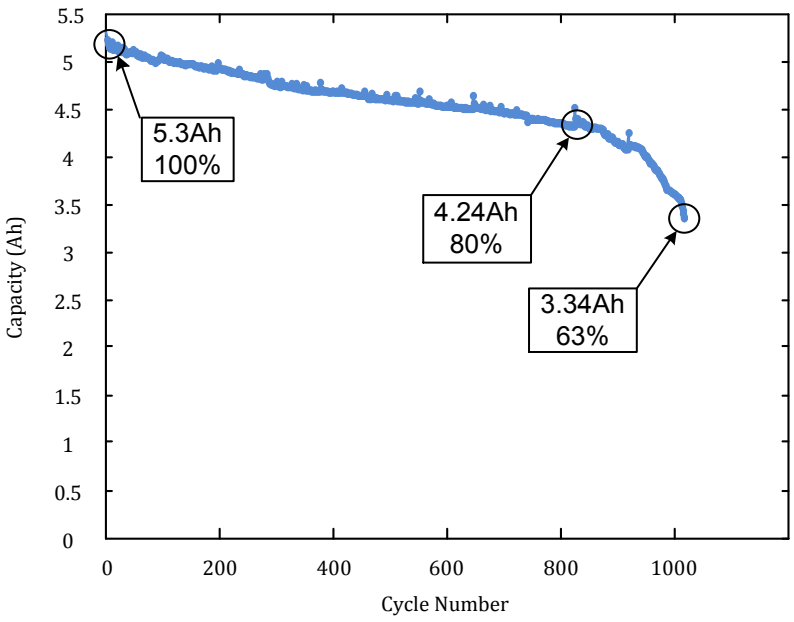

Figure 1.8 Li-ion battery capacity degradation as cycles increase

As the EV mileage increasing, the battery performance gradually declines. Consequently, the performance of EVs is also influenced. The main causes of the poor performance are the reduced capacity and the increased internal resistance of the aged

battery. A typical cycle life curve of Li-ion battery is plotted in Fig. 1.8. The capacity of Li-ion battery decreases as cycles increase. On the one hand, the EV available range is shortened due to the capacity loss. On the other hand, the increased internal resistance not only limits the peak power for acceleration and regenerative braking but also generates extra heat to accelerate the aging process.

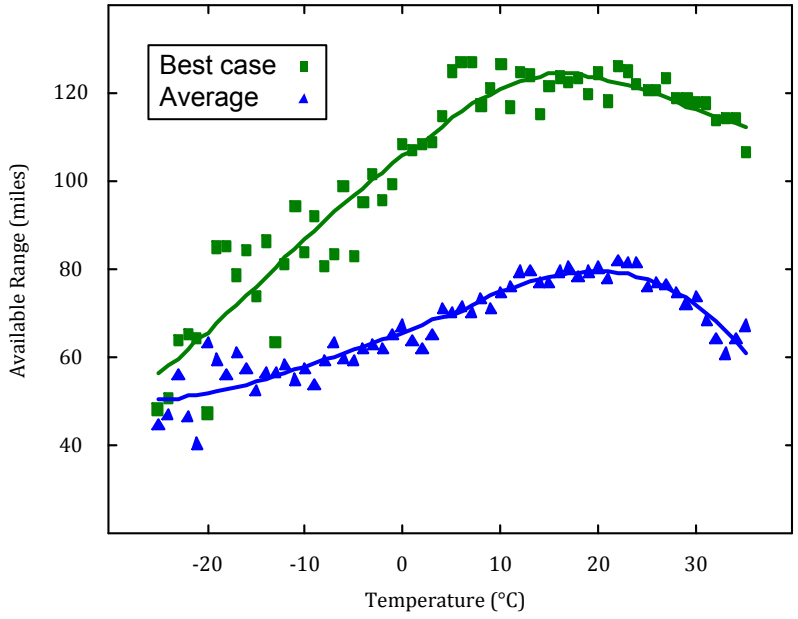

Figure 1.9 Nissan Leaf EV available range at various temperatures

The other factor affecting Li-ion battery is the environmental temperature. At low temperature, the performance of battery decreases significantly, which causes the available range reduction in EVs. As shown in Fig. 1.9, collected from 7,375 individual trips of Nissan Leaf EV national wide in the United States, the statistic result indicates that the available range is reduced up to 30% at low temperatures.

Therefore, to realize accurate battery states estimation and improve the performance of EVs, it is necessary to understand the temperature and aging uncertainties to Li-ion battery modeling and the techniques of overcoming these uncertainties.

1.4 Literatures Review

A number of researchers from various research areas have developed a wide variety of Li-ion battery models and states estimation algorithms at varying degrees of complexity. The influence of battery aging and temperature is also a popular research topic in academia. Some studies have been conducted to investigate these two problems.

The Li-ion battery models in most literature can be mainly divided into three categories: the electrochemical models, the black box models, and the equivalent circuit models. The electrochemical models mainly focus on modeling the internal chemical reactions in the Li-ion battery. These models not only present battery's external performance but also express the variation of internal parameters such as electrolyte concentration and electric current density on surface quality. The porous electrode model and analytical method proposed by J. S. Newman [64] are widely used in electrochemical models [65-67]. C. Y. Wang [68] proposed a computational battery dynamics (CBD) based multi-scale battery model to predict EVs and HEVs performance. A one-dimension isothermal electrochemical model for multiple battery types is developed by [69] M. Doyle. V. R. Subramanian [70] built a mathematical battery model considering the galvanostatic boundary conditions.

The black box modeling method can model a system when its internal structures are unknown or unclear. The black box model only cares the external behavior of a system. The black box based battery models are essentially a set of linear or nonlinear functions that are used to describe the battery behaviors. J. P. Wang built nonlinear black box battery models based on support vector machine (SVM) [75] and stochastic fuzzy neural network [76].

The equivalent circuit models use electric elements such as resistors, capacitors and voltage sources to describe the battery behaviors. State-space equations of these models can be easily derived so that they are suitable for simulation and control in the BMS applications. Min Chen [73] proposed an electrical battery model which can predict the I-V performance. G. L. Plett proposes a series of equivalent circuit models [74]. In his studies, the combined model with hysteresis and self-correction has the best performance.

G. L. Plett mentioned the dual-Kalman filter method to implement SoC and SoH estimation simultaneously in [74]. One observer is used to estimate the SoC and the other is to renew the model parameters and estimate the SoH. From the point view of system identification, this method does not consider the stability problem and lack of theory proof.

P. Bentley [82] used a similar method, the joint extended Kalman filter, to estimate the SoH of the Lead-acid battery. They use the capacitor in the equivalent circuit model from ADVISOR software as the pattern of battery capacity. The capacitance and other states formed an extended states vector. Then the extended Kalman filter is used to

estimate those states. There is a similar problem in this method with [76], the lack of stability. The system identification results during operation may change dramatically so that the simultaneous estimation of both parameters and state variables can be questionable.

C. Weng [75] studied the SoH through investigating changes in the open circuit voltage (OCV) curves. They applied the incremental capacity analysis (ICA) and support vector regression (SVR) algorithm to extract this OCV change signature for onboard SoH monitoring. However, this method requires high resolution and high sampling rate as well as data post-processing, which is hard to realize in practice.

Hussein, A.A [76] used an artificial neural network (ANN) based approach to estimate the capacity fade in batteries for EVs. W. He [77] used Dempster-Shafer and Bayesian Monte Carlo theory to build a battery capacity estimation model. The problem of these kinds of approaches is that they usually require a large scale of training data from experimental tests, and did not consider the theory basic of battery aging mechanism.

Yan Ji et al. [78] proposed a combined experimental and modeling approach to build an electrochemical-thermal coupled model. The proposed model is applied and validated by testing 2.2Ah 18650 cylindrical cells at low temperatures (−20°C).

Noboru Sato [79] carried out the thermodynamics experiment for the lithium-ion battery for EVs and confirmed that the thermal generation factors can be decomposed into three elements: reaction heat value Q_r, polarization heat value Q_p, and Joule heat value Q_J.

Jaeshin Yi et al. [80] built the two-dimensional mathematical model for the Li-ion battery discharge behavior at low temperature. They also calculated the heat generation from chemical reactions and Ohmic resistance to predict the temperature variations of the Li-ion battery as a function of the discharge time.

S.S. Zhang et al. [81] evaluated the low-temperature performance of 18650 Li-ion batteries through EIS test and cycling test. They found the delithiated graphite and lithiated cathode have a very high charge-transfer resistance R_{ct} when the battery is being charged. Therefore, the Li-ion battery in the discharged state suffers a higher polarization.

In summary, the aging and temperature problems in battery models and states estimations are not well considered in the most of literature. Other researchers focus on the two problems are usually theoretical based and did not consider the practicability for EV applications.

1.5 Dissertation Organization

The remainder of this dissertation is organized as follows. Next four chapters have a logical progression, but they may be read independently. The first of these, Chapter 2 introduces the basic knowledge about Li-ion battery modeling and focus on the equivalent circuit model and associated parameter identification. The last part of this chapter presents the model based SoC estimation with AEKF method. In Chapter 3, we focus on the understanding of the temperature-dependent performance of Li-ion battery through EIS experimental tests and theoretical analysis. The temperature influence to

equivalent circuit modeling is discussed and the model compensation functions are derived from experimental data. In Chapter 4, the battery aging mechanisms are revisited firstly, and then a series of aging tests are conducted to understand the Li-ion battery degradation path. In the latter part of this chapter, the incremental capacity analysis is applied to experimental data for SoH estimation. A bias correction modeling method is developed for the aged battery. Study of parallel-connected battery packs is presented in Chapter 5. First, the inconsistency problem in battery cells with different aging level and its influence to parallel-connected packs are discussed. Then, based on analysis and experimental data, the parallel connected battery pack model are developed to simulate the current distribution in parallel connected cells. Finally, Chapter 6 is the conclusion and future work.

CHAPTER 2

Li-ion Battery Modeling and States-of-Charge Estimation

2.1 Background

As mentioned in chapter 1, it is not practical to directly measure the battery states, i.e. the SoC and SoH, by using sensors. These states are usually estimated through model-based estimation algorithm in a BMS. Therefore, battery models are considered as the core of estimation algorithm. Previous researchers propose various battery models. In general, these battery models can be divided into two categories: principle-based models and behavior based models.

Principle based models, also known as the electrochemical models, are based on the electrochemical principles which reflect the chemical and thermal process in the Li-ion battery. The research of microcosmic behavior plays a major role in the process of building electrochemical models. Compared with behavior models, the electrochemical models contain lots of Partial Differential Equations (PDEs), non-linear equations and more parameters. Thus, the electrochemical models require higher computational costs and large memory storage space. Researchers have put efforts of numerical simplification and model order reduction to reduce the high complexity of the electrochemical model [33]. The typical mathematical model of the positive electrode in a Li-ion battery can be expressed in Table. 2.1.

Table 2.1 Mathematical model of the positive electrode of Li-ion battery

Mathematical model of positive electrode		
Solid phase	PDE equation	$\frac{\partial}{\partial \mathrm{x}}(D_{s,3}^{eff}\frac{\partial}{\partial \mathrm{x}}\varphi_{s,3}^{eff}(\mathrm{x},\mathrm{t})) = j_{s,3}(x,t)$
	Boundary condition	$\frac{\partial}{\partial \mathrm{x}}\varphi_{s,3}(x,t) = \frac{J}{\sigma_{s,3}^{eff}}, \mathrm{x}=0, \frac{\partial}{\partial \mathrm{x}}\varphi_{s,3}(x,t) = 0, \mathrm{x} = \mathrm{L}_c$
Liquid phase	PDE equation	$j_{s,3}(\mathrm{x},\mathrm{t}) = \frac{\partial}{\partial \mathrm{x}}K_{e,3}^{D,eff}\left[\frac{\partial \ln C_{e,3}(x,t)}{\partial x}\right] + \frac{\partial y}{\partial x}K_{e,3}^{D,eff}(x,t)\frac{\partial \varphi_{e,3}(x,t)}{\partial x}$
	Boundary condition	$\frac{\partial}{\partial \mathrm{x}}\varphi_{e,3}(x,t) = 0, x=0, \frac{\partial}{\partial x}\varphi_{e,3}(x,t) = \frac{J}{K_{s,3}^{eff}}, x = L_c$

where $\varphi_{s,3}, \varphi_{e,3}$ are potential in solid and liquid phase, $\sigma_{s,3}$ is the conductivity of solid phase, $\mathrm{D}_{s,3}^{eff}$ is the diffusion coefficient, $J(x,t)$ is the current density in x position, *K* is conductivity of liquid solution.

Behaviors based models refer to that, on the basis of a massive scale of experimental and statistical data, build the battery models through various methods of data mining and numerical simulation. Typical behavior based models include resistance model [34~35], equivalent circuit model, fuzzy logic model, artificial neuron network (ANN) model and so on. This kind of models has a simple structure and ease of use in the BMS. However, it needs numerous of training data to build the model. Some static nonlinear model, such as the ANN model, suffers from the poor performance and weak robustness due to limited training data set in practice. Researchers have also put lots of effort to combine the

electrochemical model and behavior model together to develop battery models with both advantages from electrochemical model and behavior model.

Nevertheless, the purpose of building Li-ion battery models are to help the application of Li-ion battery. For the large-scale systems, such as EVs, there are some prerequisites in the Li-ion battery models. The one with the highest priority is the requirement of stability and reliability. Due to the safety concern, the battery models used in practical EV applications must be very robust and stable. The existence of nonlinear equations and uncertain parameters cause the stability of electrochemical battery model cannot be effectively ensured. Therefore, the behavior-based models are adopted to carry out tasks such as battery pack optimal design, SoC estimation, system level simulation, battery cells balancing, and protection [36~39].

2.2 Li-ion Battery Equivalent Circuit Models

The typical voltage response of Li-ion battery is shown in Fig. 2.1. In the initial stage, the battery terminal voltage remains a constant voltage OCV_0, which is determined by the initial SoC. Once the battery is being discharged, the terminal voltage drops instantly due to the internal resistance R_o. During the discharge, the cumulative effect of OCV drop and polarization keeps the terminal voltage decreasing. Once the discharge current is removed, the terminal voltage increases instantly and then slowly returns to a new voltage OCV_1 through depolarization process. The voltage response during the charging process is similar to discharging.

Among all behavior battery models, the lumped equivalent circuit models have simple structures with fewer parameters. This kind of model idealizes the battery as the combination of a voltage source in series with a resistor and other dynamic elements such as capacitors. With simple structures, the model accuracy is usually insufficient. By modifying the model structure and adding additional compensation functions, the accuracy can be improved.

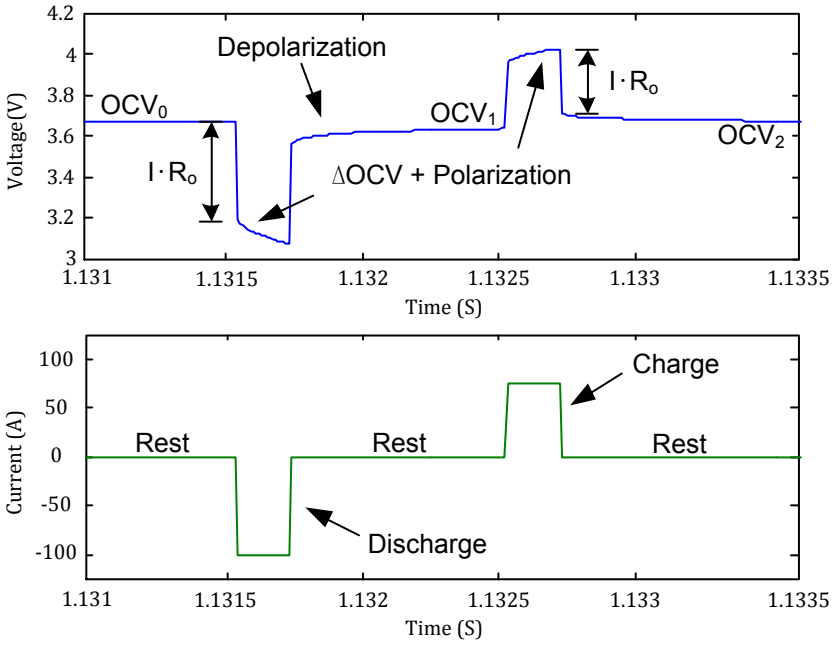

Figure 2.1 Voltage response of Li-ion battery

Six typical equivalent circuit battery models from the literatures are illustrated in Fig. 2.2. Three models in the first row are based on [40], as following: simple model, zero state hysteresis model, one state hysteresis with second order low pass filter (LPF) model.

Models in the second row are RC networks based lumped equivalent circuit models: one order RC model, two orders RC model, one order RC model with one state hysteresis.

These models can be regard as a model subset which contains most lumped equivalent circuit models in the literatures. SoC, charge/discharge current, and hysteresis effects are all considered in these models. Discrete form dynamic equations and mathematical descriptions of each model are presented as follow:

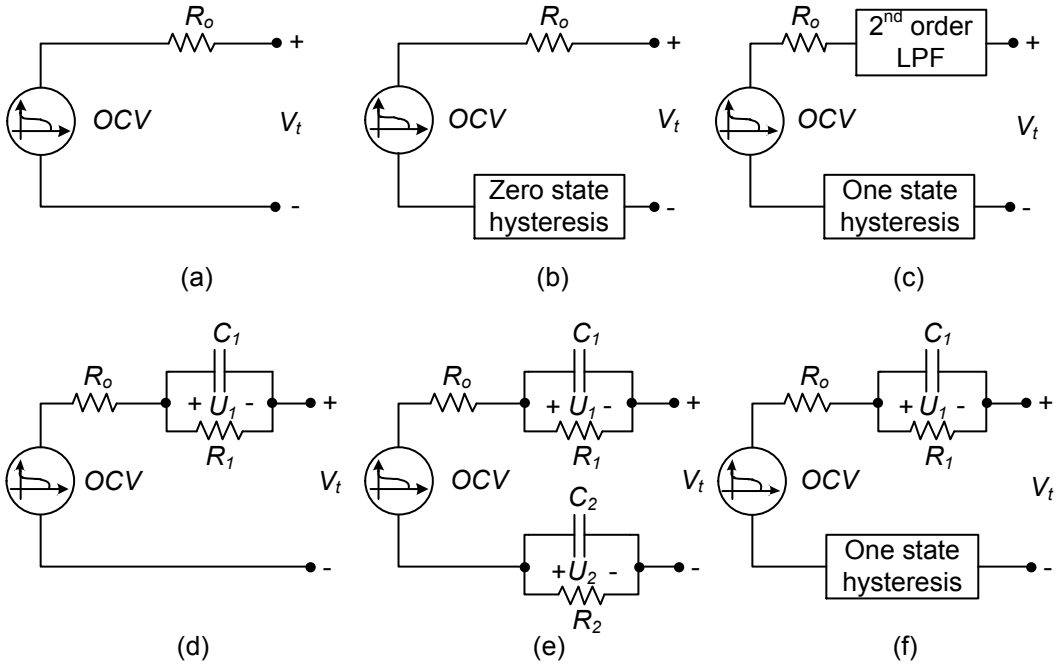

Figure 2.2 Six typical equivalent circuit models

Simple model:

$$V_t(n) = OCV\big(SoC(n)\big) - I(n)R_o \tag{2.1}$$

$$OCV(SoC(n)) = K_0 - \frac{K_1}{SoC(n)} - K_2 SoC(n) + K_3 \ln(SoC(n)) + K_4 \ln(1 - SoC(n)) \tag{2.2}$$

where n is the discrete step; $V_t(n)$ stands for terminal voltage of battery; $OCV(SoC(n))$ stands for the OCV as a function of SoC; $I(n)$ stands for input current, where positive is for discharge and negative is for charge; R_o stands for internal resistance; K_0, K_1, K_2, K_3, K_4 are parameters used to describe the correspondence between OCV and SoC. In some cases, lookup tables are used to describe the OCV-SoC function for better accuracy.

Zero state hysteresis model:

$$V_t(n) = OCV\big(SoC(n)\big) - I(n)R_o - s(n)M \tag{2.3}$$

$$s(n) = \begin{cases} 1, & I(n) > \varepsilon \\ -1, & I(n) < -\varepsilon \\ s(n-1) \end{cases} \tag{2.4}$$

where M is a constant used to describe the hysteresis effect; ε is a small positive constant for dead band.

One-state hysteresis with second order LPF model:

$$V_t(n) = OCV\big(SoC(n)\big) - I(n)R_o + h(n) + g_1 f_1(n) + g_2 f_2(n) \tag{2.5}$$

$$\begin{bmatrix} f_1(n+1) \\ f_2(n+1) \\ h(n+1) \end{bmatrix} = \begin{bmatrix} \alpha_1 & 0 & 0 \\ 0 & \alpha_2 & 0 \\ 0 & 0 & e^{-|kI(n)\Delta t|} \end{bmatrix} \begin{bmatrix} f_1(n) \\ f_2(n) \\ h(n) \end{bmatrix} + \begin{bmatrix} 1 & 0 \\ 1 & 0 \\ 0 & 1 - e^{-|kI(n)\Delta t|} \end{bmatrix} \begin{bmatrix} I(n) \\ H \end{bmatrix} \tag{2.6}$$

where h stands for the hysteresis voltage; H is the maximum hysteresis voltage; k is the fading factor; f_1 and f_2 stand for the states of LPF; a_1 and a_2 are the diagonal elements of

filter states transfer matrix; g_1 and g_2 are the element of filter output transfer matrix; Δt is the sampling interval.

One-order RC circuit model:

$$V_t(n) = OCV\big(SoC(n)\big) - I(n)R_o - U_1(n) \tag{2.7}$$

$$U_1(n+1) = e^{\left(-\frac{\Delta t}{\tau_1}\right)}U_1(n) + R_1\left(1 - e^{\left(-\frac{\Delta t}{\tau_1}\right)}\right)I(n) \tag{2.8}$$

$$\tau_1 = R_1C_1$$

Two-orders RC circuit model:

$$V_t(n) = OCV\big(SoC(n)\big) - I(n)R_o - U_1(n) - U_2(n) \tag{2.9}$$

$$U_1(n+1) = e^{\left(-\frac{\Delta t}{\tau_1}\right)}U_1(n) + R_1\left(1 - e^{\left(-\frac{\Delta t}{\tau_1}\right)}\right)I(n) \tag{2.10}$$

$$U_2(n+1) = e^{\left(-\frac{\Delta t}{\tau_2}\right)}U_2(n) + R_2\left(1 - e^{\left(-\frac{\Delta t}{\tau_2}\right)}\right)I(n) \tag{2.11}$$

$$\tau_1 = R_1C_1 \tag{2.12}$$

$$\tau_2 = R_2C_2 \tag{2.13}$$

where U_1 ,U_2, τ_1, and τ_2 are the voltage and time constant of RC networks, respectively.

One-order RC circuit with one state hysteresis model:

$$V_t(n) = OCV\big(SoC(n)\big) - I(n)R_o - U_1(n) - U_2(n) \tag{2.14}$$

$$U_1(n+1) = e^{\left(-\frac{\Delta t}{\tau_1}\right)} U_1(n) + R_1\left(1 - e^{\left(-\frac{\Delta t}{\tau_1}\right)}\right) I(n) \tag{2.15}$$

$$h(n+1) = e^{-|kI(n)\Delta t|} h(n) + \left[1 - e^{-|kI(n)\Delta t|}\right] H \tag{2.16}$$

2.3 Model Parameters Identification

To apply models into simulation and states estimation, all unknown parameters in the model must be identified separately from training data. Because these models involve nonlinear functions and discrete states, common parameters identification approaches used for linear systems such as least squares method [41] and subspace identification method [42] are not easily applicable. Genetic Algorithm (GA) is used for parameters identification to balance the performance of accuracy and computation time. GA algorithm provides a global optimal solution with superior effective on multi-targets and provides excellent convergence speed.

Select the two orders RC model as an example and set the current *I* and voltage V_t as the input/output, its transfer function can be written as:

$$V_t(s) = OCV(SoC(s)) - I(s)\left(R_o + \frac{R_1}{1+R_1C_1s} + \frac{R_2}{1+R_2C_2s}\right) \tag{2.17}$$

This recurrence equation can be rewritten to an autoregressive model and the target vector is built as shown below:

$$\varphi_n(k) = [1 \quad V_t(k) \quad \dots \quad V_t(k-n) \quad I(k) \quad \dots \quad I(k-n)\,] \tag{2.18}$$

$$\theta_n(k) = [(1 - \sum_{i=1}^{n} C_i)OCV(k) \quad C_1 \quad \dots \quad C_{2n+1}]^T \tag{2.19}$$

The goal of parameters identification is to minimize the error between measured data and model output. The cost function to be minimized is the sum of squared errors at the sample points:

$$min\{\Gamma(\zeta_j^g)\}, \Gamma(\zeta_j^g) = \frac{1}{N}\sum_{k=1}^{N}\left(V_{t,k} - \hat{V}_{t,k}\left(\widehat{\zeta_j^g}\right)\right)^2 \tag{2.20}$$

where $\Gamma(\zeta_j^g)$ is the mean-squared error between the measured voltage and predicted voltage of the current individual *j* of population g. ζ_j^g is the estimated parameter of the current individual *j* of population g. ζ represents the optimized parameter and $\zeta = [R_o \quad R_1 \quad R_2 \quad C_1 \quad C_2]$. $\hat{V}_{t,k}$ denotes the estimation value of V_t at index k. N is the length of measured data. The maximum generations is set to be 100 in this optimization process.

Fig 2.3 shows an example of two-order RC model fitting result. The data is collected from the depolarization process of an NCM Li-ion battery cell after 10A discharge at SoC=60%. The top part plots the model output and measured data together. The bottom part plots the estimation error. The goodness of fit and identified parameters is shown in Table 2.2.

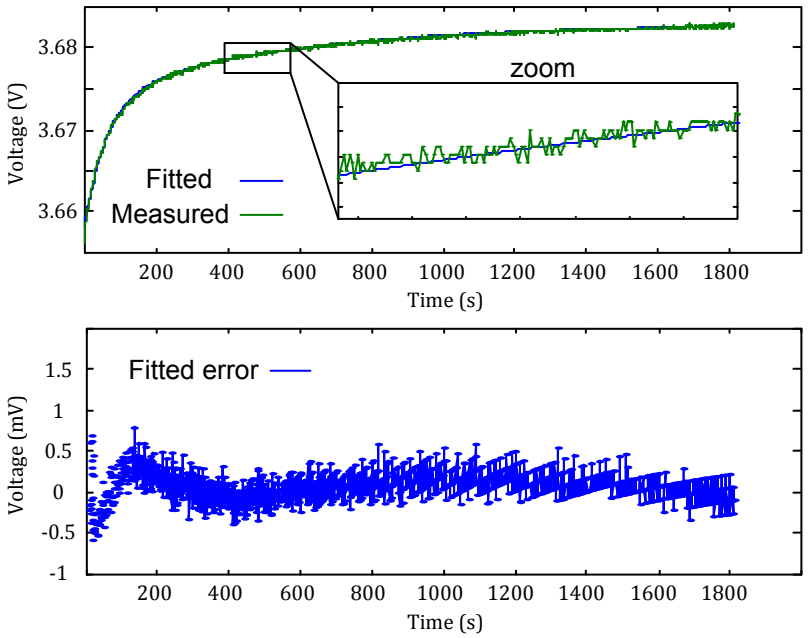

Figure 2.3 Fitting and measured data of two-order RC battery model (Top). Estimation error (Bottom)

Table 2.2 Goodness of fit and identified parameters

Goodness of fit		Identified parameters	
SSE	$5.819 \cdot 10^{-5}$	OCV	3.683V
R-square	0.9979	U1	0.015.54mV
Adjusted R-square	0.9979	T1	0.01627
RMSE	$1.801 \cdot 10^{-4}$	U2	9.265mV
		T2	0.001833

2.4 State-Of-Charge Estimation via AEKF method

As we discussed in Chapter 1.3, providing accurate SoC estimation result to the vehicle controllers and drivers is the most important function of a BMS. Incorrect or inaccurate SoC estimation may cause SoC variation, lower the vehicle efficiency and reduce lifetime. In general, the SoC of Li-ion battery is defined as the ratio of current capacity to nominal capacity at a certain current rate. The nominal capacity is given by the battery manufacturer and represents the maximum amount of charge can be stored. Ampere-hour counting is the most widely used method based on the material conservation during charge or discharge reactions. This approach simply integrates current with time to calculate the SoC. The discrete form of SoC calculation can be written as:

$$SoC(n+1) = SoC(n) + \frac{i(n)\cdot\Delta t}{Capacity} \tag{2.21}$$

where i is the current flow into or out from the Li-ion battery. Δt is the sampling period. $SoC(n+1)$ at the time n+1 is determined by the previous $SoC(n)$ at time n and the product of sampling period Δt and current $i(n)$ at time n. There are three obvious disadvantages in this method. First, it is difficult to determine the $SoC(0)$ in the initial stage. Inaccurate initial $SoC(0)$ could cause future estimation error. Second, in practice, the measurement accuracy of current sensor is influenced by several issues, including environmental electromagnetic noise, temperature, limited bandwidth and others. Moreover, these current sensor errors will accumulate due to the integration operation and then cause

higher estimation error in the further. Third, as mentioned in Chapter 1, rather than a constant, the nominal Li-ion capacity changes with current rate, aging and temperature.

To solve the initial state estimation problem, one may use the OCV-SoC lookup table to calibrate the initial $SoC(0)$. Originally from the application of lead-acid battery [43], the approximately linear relationship between SoC and OCV can be given as:

$$OCV(SoC) = a_0 + a_1 \cdot SoC \tag{2.22}$$

where a_0 is the battery cutoff voltage and a_1 is the fitting parameter to fit the maximum voltage when SoC equals 100%.

However, the approximately linear relation of OCV and SoC cannot be simply applied to Li-ion battery. For Li-ion battery not in the equilibrium state or LFP battery with flat OCV-SoC curve, this calibration method is not reliable. Furthermore, the OCV-SOC relationship is also nonlinear with hysteresis and can be influenced by temperature.

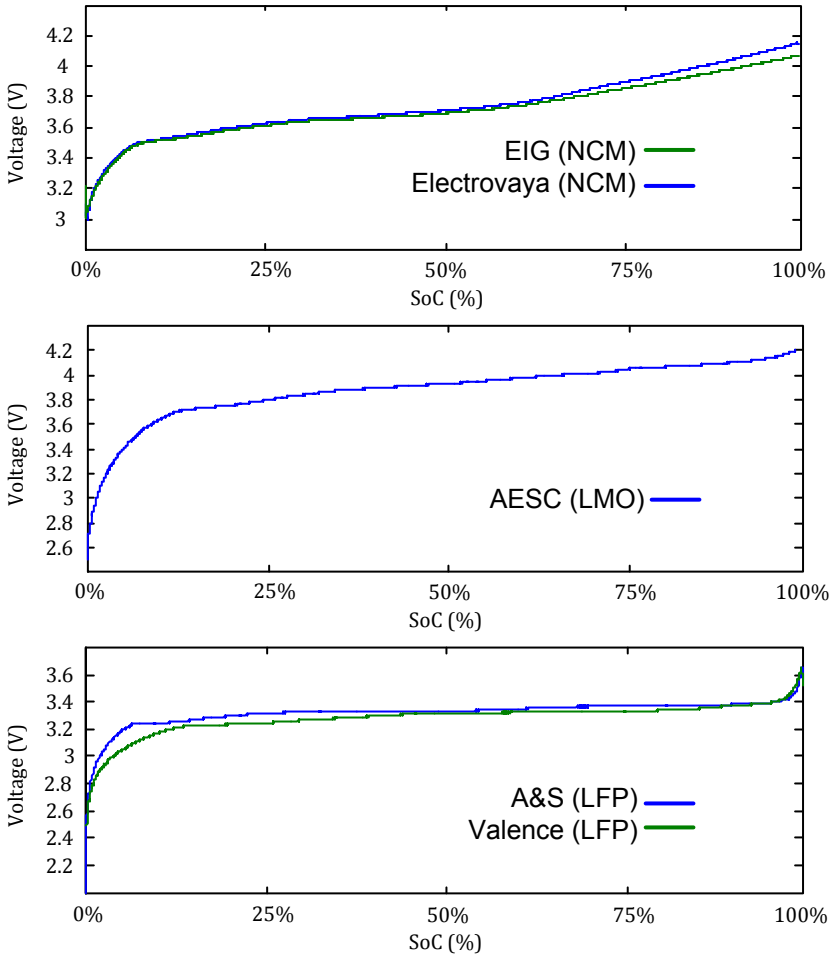

Figure 2.4 OCV-SoC curves of five Li-ion batteries

Fig. 2.4 shows the OCV-SoC plots of five different Li-ion batteries used in this study. Notice that these OCV-SoC plots are obtained through continuous low current charging (1/20 C). Thus, the OCV at the end (0%) and beginning (100%) of SoC should be ignored. Although both Electrovaya and EIG, A&S and Valence batteries have the same NCM/LFP positive electrode, their OCV-SoC plots are slightly different. That is because even with same electrode material, manufacturers may have different battery design, such

as the different doping ratio of the Nickel, Cobalt, Manganese, and Aluminum elements in the positive electrode. We may see that a flat voltage plateau exists in the LFP battery OCV-SoC curves at around 3.3V. Compared with NCM battery (2.5V/3V to 4.05V/4.15V) and LMO battery (2.5V to 4.2V), LFP battery also has a narrow voltage range (2.5V to 3.6V). For typical voltage sensor with ±5mV error, the sensor error will cause up to 35% SoC calibration error.

Researchers proposed several state observers and battery model based SoC estimation methods to improve the performance of SoC estimation function. Plett uses the extended Kalman filter (EKF) to estimate SoC adaptively based on a simplified model [38]. Xu uses the proportion-integration (PI) observer with one order RC circuit model to estimate the SoC [3]. He also compares the performance of SoC estimation by using different observers including Luenberger Observer, Sliding Mode, PI observer and Kalman filter based observer. However, this kind of observer based methods strongly depends on the model and the predetermined parameters. To improve the model accuracy is a more efficient way compared to using some advanced algorithms.

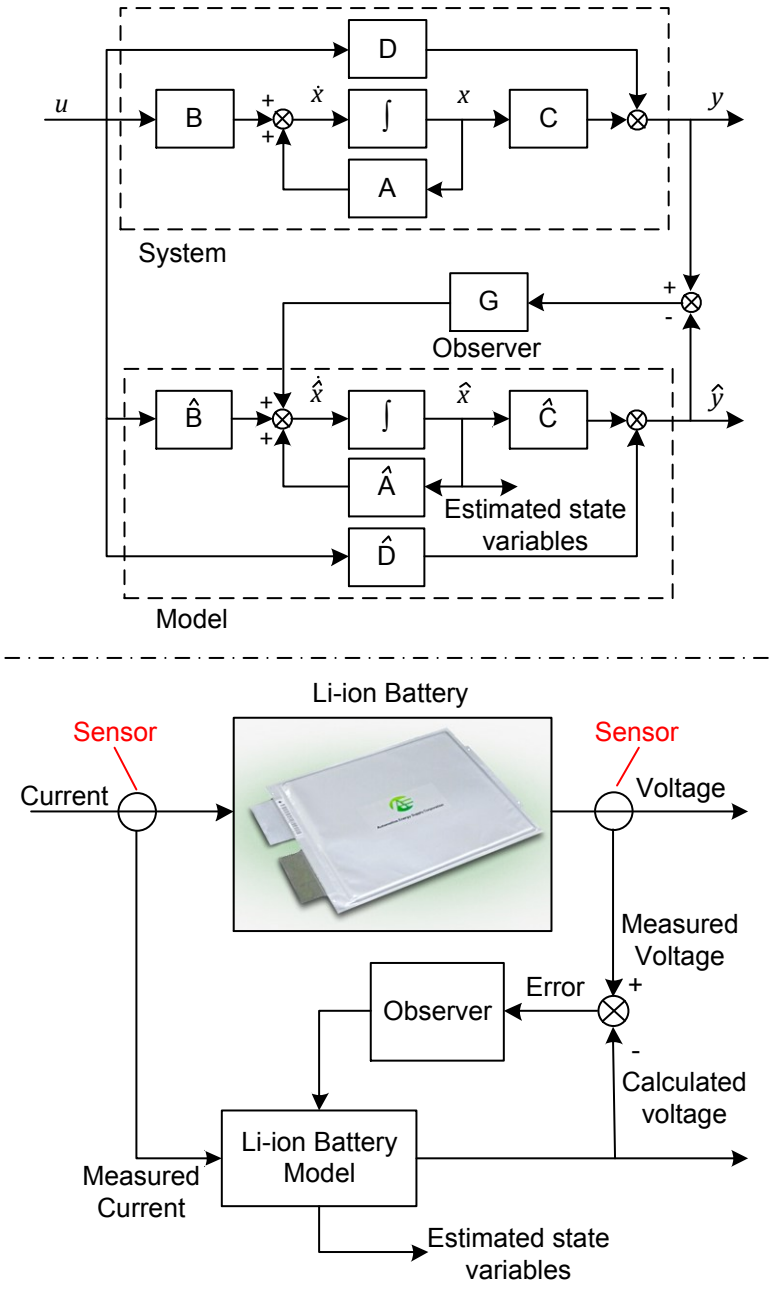

Figure 2.5 Model observer based Li-ion battery states estimation

For a given linear time-invariant system, its state space equation and discrete form can be described as:

$$\begin{cases} \dot{x} = Ax + Bu \\ y = Cx + Du \end{cases} \tag{2.23}$$

$$\begin{cases} x(n+1) = Ax(n) + Bu(n) \\ y(n) = Cx(n) + Du(n) \end{cases} \tag{2.24}$$

where x is the state variable; u is system input; y is the system out; A, B, C, D are the system matrices. Based on the second equation, system output y is the combination of states variable x and system input u. Therefore, if the system input u, output y, system matrices C and D are known, the state variable x can be derived. This non-measurable state variable x can be either used for feedback control or just for observation purpose. Ideally, we may build the identical model of an actual system and send the same input u as the real system does to calculate the estimated state variable $\hat{x}$. This method is called the open loop observer or open loop estimator. However, the open loop observer method is not feasible in practice. If the initial state of variable $\hat{x}(0)$ is incorrect, the further estimation will be also incorrect. Besides, the noise contained in the measured input will cause further error in the estimation. To solve this problem, we add a feedback loop to the system, use the difference between estimated system output y and actual system output y to correct the estimated state variable x. The observer system can be rewritten as:

$$\begin{cases} \dot{\hat{x}} = \hat{A}\hat{x} + \hat{B}u + G(y - \hat{y}) \\ \hat{y} = \hat{C}\hat{x} + \hat{D}u \end{cases} \tag{2.25}$$

$$\begin{cases} \hat{x}(n+1) = \hat{A}\hat{x}(n) + \hat{B}u(n) + G(y(n) - \hat{y}(n)) \\ \hat{y}(n) = \hat{C}\hat{x}(n) + \hat{D}u(n) \end{cases} \tag{2.26}$$

where G is the observer matrix. The G can be either Luenberger observer, sliding-mode observer, Kalman filter, or any other controller or algorithm. The goal of such an observer system is to force the calculated output y to converge to the measured output and eventually force the estimated states variable $\hat{x}$ converge to the true value.

In the case of Li-ion battery SoC estimation, input u is the current i in the battery. Output y is the battery terminal voltage. State variable vector x is the internal states in selected battery model. Notice that the Li-ion battery model contains nonlinear item such as the OCV-SoC function. Thus, the state space equation of Li-ion battery model is in nonlinear form. Select one order RC network model as the example; the following discrete state space equations can be obtained:

$$\begin{cases} \begin{bmatrix} SoC(n+1) \\ U_1(n+1) \end{bmatrix} = \begin{bmatrix} 1 & 0 \\ 0 & e^{\left(\frac{-\Delta t}{R_1 C_1}\right)} \end{bmatrix} \cdot \begin{bmatrix} SoC(n+1) \\ U_1(n+1) \end{bmatrix} + \begin{bmatrix} \frac{-\Delta t}{Capacity} \\ R_1 - R_1 e^{\left(\frac{-\Delta t}{R_1 C_1}\right)} \end{bmatrix} \cdot I(n) \\ V_t(n) = \begin{bmatrix} OCV(\dots) & 0 \\ 0 & -1 \end{bmatrix} \cdot \begin{bmatrix} SoC(n) \\ U_1(n) \end{bmatrix} + [-R_o] \cdot I(n) \end{cases} \tag{2.27}$$

For the selection of observer, Kalman filter has the unique advantage of optimal converge speed and anti-noise ability, especially in harsh environments. Moreover, the Kalman filter is a discrete algorithm in nature, which is easy to implement in the BMS. For nonlinear systems, the nonlinear version of the Kalman filter called adaptive extended Kalman filter (AEKF) should be used. AEKF uses the first item of the Taylor Series expansions of system matrix to linearize model at each sampling period. AEKF

algorithm can improve the prediction precision by adaptively updating the noise covariance. The time-series based calculation process is shown in Table 2.2.

Table 2.3 Calculation process of AEKF algorithm

Nonlinear state-space model

Transition: $\boldsymbol{X}_{k+1} = f(\boldsymbol{X}_k, \boldsymbol{u}_k) + \omega_k$ (1)

Measurement: $\boldsymbol{Y}_{k+1} = h(\boldsymbol{X}_k, \boldsymbol{u}_k) + \upsilon_k$ (2)

Step I: Initialization

For k=0, set: $\widehat{\boldsymbol{X}}_0^+ = E[X_0]\boldsymbol{P}_0^+ = E\left[\left(X_0 - \widehat{\boldsymbol{X}}_0^+\right)\left(X_0 - \widehat{\boldsymbol{X}}_0^+\right)^T\right]$ (3)

Step II: Computation: For k=1, 2, …, compute

State estimate time update $\widehat{\boldsymbol{X}}_k^- = f(\widehat{\boldsymbol{X}}_{k-1}^+, \boldsymbol{u}_k)$ (4)

Error Innovation: $\boldsymbol{e}_k = \boldsymbol{Y}_k - g(\widehat{\boldsymbol{X}}_k^-, \boldsymbol{u}_k)$ (5)

Adaptive law-covariance matching:

$$\boldsymbol{H}_k = \frac{1}{M}\sum_{i=k-M+1}^{k} \boldsymbol{e}_k \boldsymbol{e}_k^T, \cdot\ \boldsymbol{R}_k = \boldsymbol{H}_k - \boldsymbol{C}_k \boldsymbol{P}_k^- \boldsymbol{C}_k^T \quad (6)$$

Error covariance time update: $\boldsymbol{P}_k^- = \boldsymbol{A}_k \boldsymbol{P}_{k-1} \boldsymbol{A}_k^T + \boldsymbol{Q}_k$ (7)

Kalman gain matrix: $\boldsymbol{K}_k = \boldsymbol{P}_k^- \boldsymbol{C}_k^T (\boldsymbol{C}_k \boldsymbol{P}_k^- \boldsymbol{C}_k^T + \boldsymbol{R}_k)^{-1}$ (8)

State estimate measurement update: $\widehat{\boldsymbol{X}}_k^+ = \widehat{\boldsymbol{X}}_k^- + \boldsymbol{K}_k \boldsymbol{e}_k$ (9)

Noise and error covariance measurement update:

$$\boldsymbol{Q}_k = \boldsymbol{K}_k \boldsymbol{H}_k \boldsymbol{K}_k^T \boldsymbol{P}_k^+ = (\boldsymbol{I} - \boldsymbol{K}_k \boldsymbol{C}_k)\boldsymbol{P}_k^- \quad (10)$$

where, $\boldsymbol{A}_k = \left.\frac{\partial f(\boldsymbol{X}_k, \boldsymbol{u}_k)}{\partial \boldsymbol{X}}\right|_{\boldsymbol{X}=\widehat{\boldsymbol{X}}_k^-}$, $\boldsymbol{C}_k = \left.\frac{\partial h(\boldsymbol{X}_k, \boldsymbol{u}_k)}{\partial \boldsymbol{X}}\right|_{\boldsymbol{X}=\widehat{\boldsymbol{X}}_k^-}$ (11)

where $\boldsymbol{X}_k$ is the system state vector at the kth sampling time, which represents the total effect of system inputs $\boldsymbol{u}_k$ on the present system operation. ω_k describes the process noise and υ_k is the measurement noise which does not affect the system state, but can be reflected in the system output estimates $\boldsymbol{Y}_k$. And ω_k is assumed to be Gaussian white noise with zero mean and covariance $\boldsymbol{Q}_k$; υ_k is assumed to be Gaussian white noise with zero mean and covariance $\boldsymbol{R}_k$. $f(\boldsymbol{X}_k, \boldsymbol{U}_k)$ and $h(\boldsymbol{X}_k, \boldsymbol{U}_k)$ are the state transition and measurement functions, respectively.

Select the one order RC circuit model as the example, the complete flow chart of SoC estimation based on AEKF and experimental verification are shown in Fig. 2.6 and Fig. 2.7. The discharge and charge current are loaded on the Li-ion battery cell and the one order RC model built in MATLAB/Simulink simultaneously. Terminal voltage error between the estimation and the experimental data is reduced by adaptively updating the AEKF observer gain. Then the observer with the updated gain is used to compensate for the state estimation error. The estimation of SoC is then fed back to update the parameters of the battery model for the next SoC estimation.

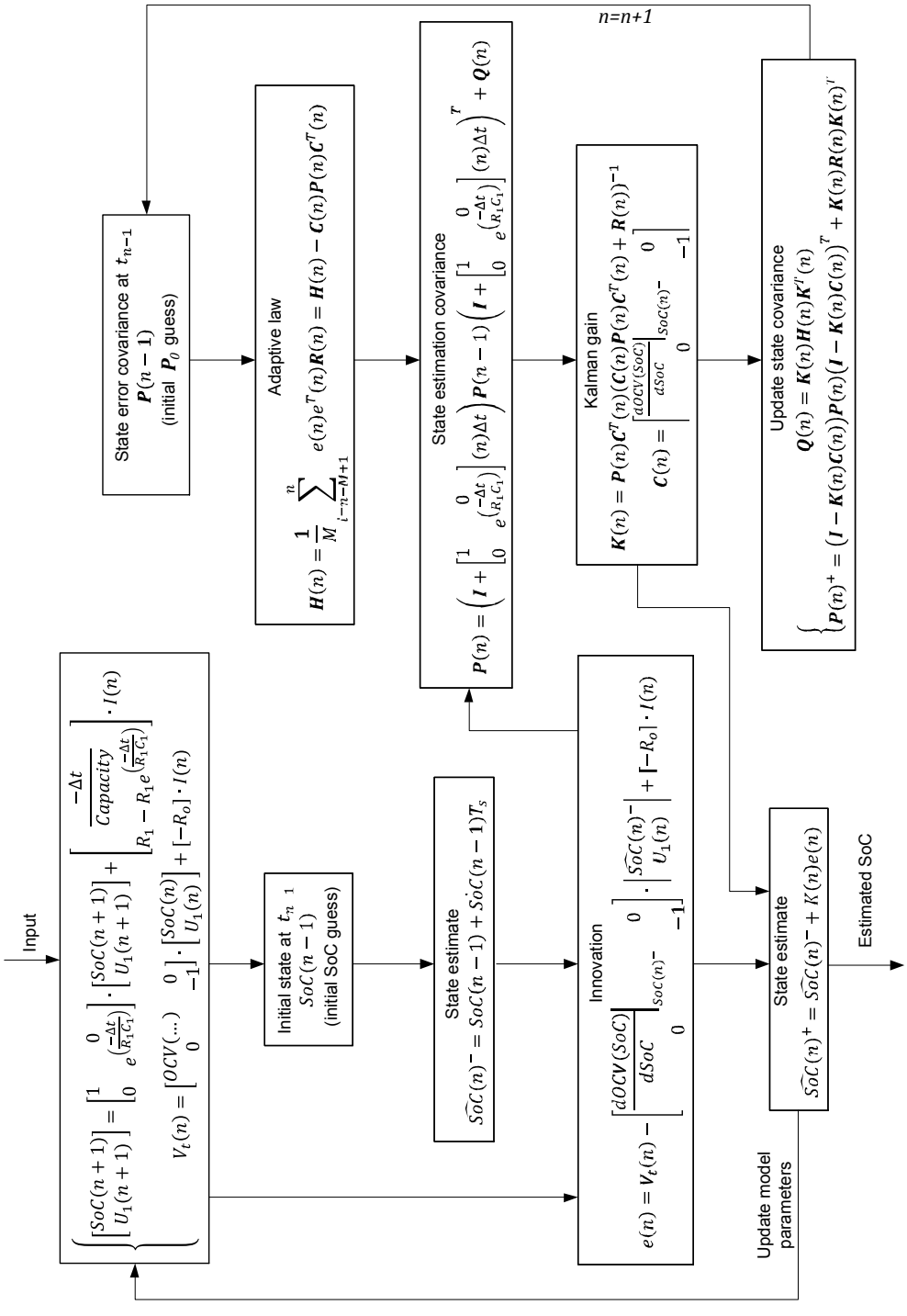

Figure 2.6 Implementation flowchart of the AEKF algorithm

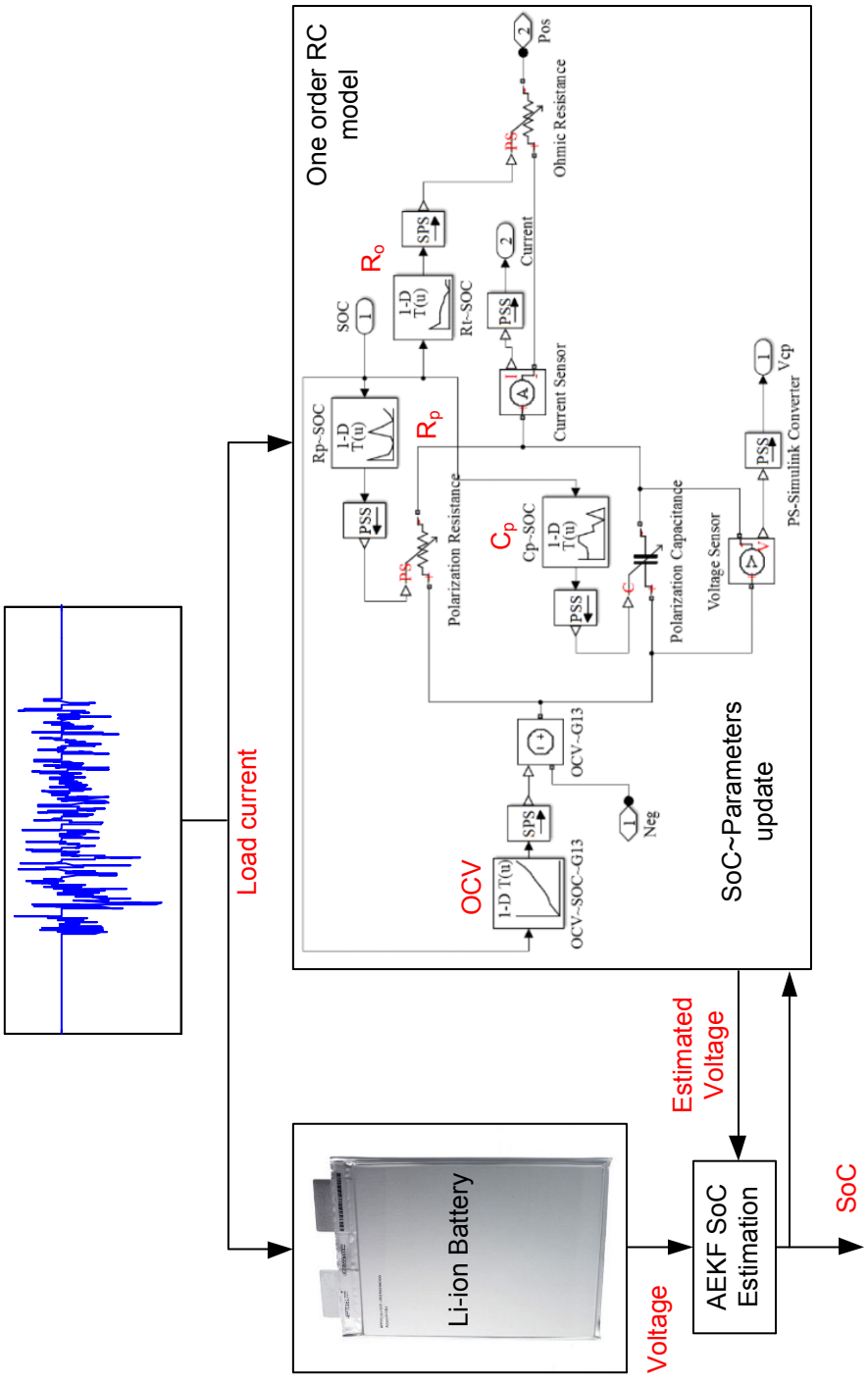

Figure 2.7 AEKF SoC estimation with one RC circuit model

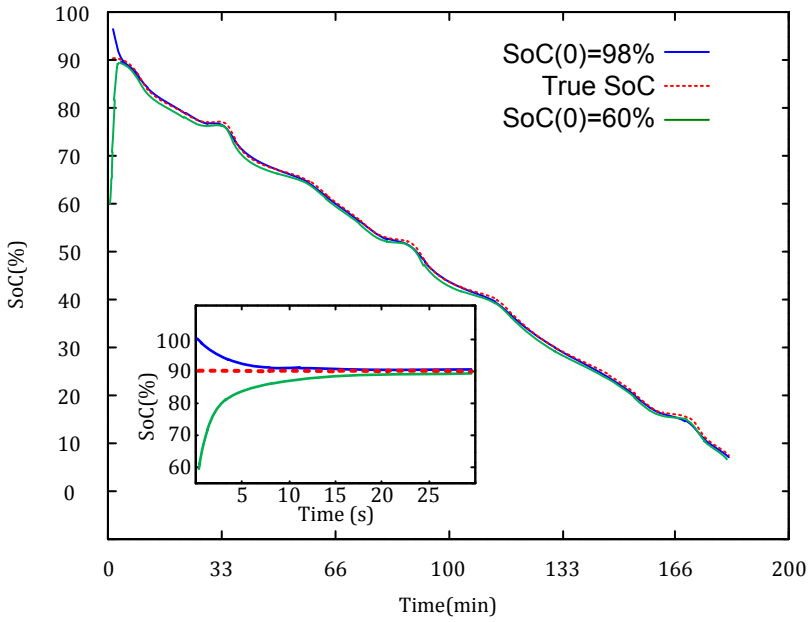

Figure 2.8 AEKF SoC estimation results

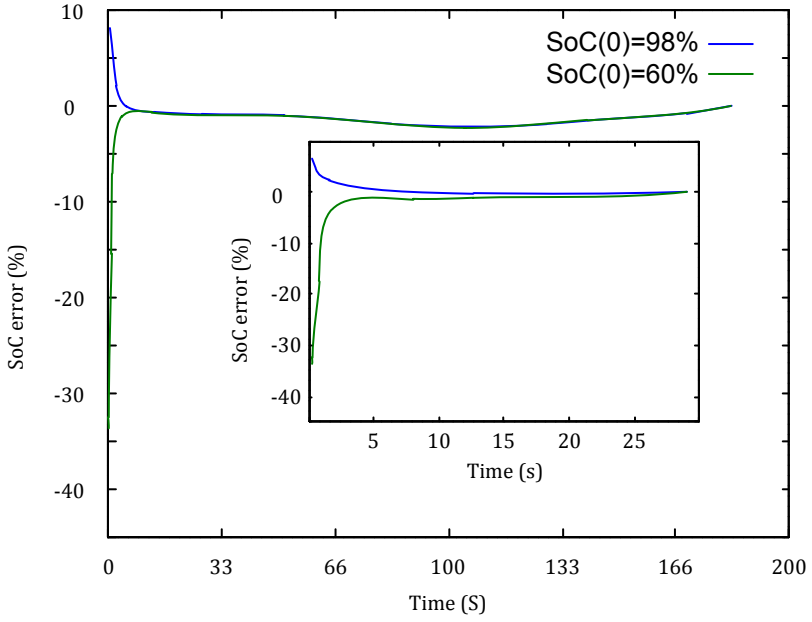

Figure 2.9 SoC estimation error

The SoC estimation results and their estimation errors are plotted in Fig. 2.8 and Fig. 2.9. Two wrong initial SoC(0) are set to be 98% and 60% in purpose to evaluate the robustness performance. From these two figures, the SoC estimation can trace the true trajectory accurately and quickly especially with a larger initial SoC error. Furthermore, the SoC estimation can converge to the reference SoC trajectory with several sampling intervals. For different large initial SoC errors, the SoC estimation can converge to the true value after several sampling intervals. That is because the proposed approach can precisely estimate the voltage and adjust timely the Kalman gain according to the error between the measured and estimated terminal voltage. The error SoC brings bigger terminal voltage errors, which will in turn cause a large Kalman gain matrix and then compensate the SoC estimation in an efficient closed loop feedback.

2.5 Summary

In this chapter, we introduce the basic knowledge of Li-ion battery modeling first and then focus on the lumped equivalent circuit modeling method. The associated parameters identification method is also introduced. A second order RC equivalent circuit model is selected to demonstrate the modeling procedure. Finally, we apply the one order RC circuit model with AEKF algorithm to implement the SoC estimation. The result shows if battery model is accurate, the closed-loop AEKF SoC estimation method can solve the initial SoC value problem and provide good estimation results.

CHAPTER 3

Temperature Uncertainty in Li-ion Battery Performance and Modeling

3.1 Background

Temperature is one of the crucial factors that affect the performance of Li-ion battery. As discussed in chapter 1, the available mileage of an EV highly depends on the environmental temperature. At low temperature, the mileage decrease significantly [1-4]. Similar to any ICE vehicles, EVs have to be able to operate in various harsh environments, including the low-temperature environment. Besides, unlike ICE vehicles which can be refueled in minutes at gas stations, EVs need several hours to charge the battery while suffering the low temperature, as demonstrated in Fig 3.1.

Figure 3.1 Tesla Model S EV (left) and Nissan Leaf EV (right) at public charging stations under low-temperature environment

Compared to the battery aging, which is considered as a long-term process, the influence of temperature is a transient process that cannot be neglected. The initial

motivation of this temperature study is from the observation of battery aging tests. Fig. 3.2 plots capacity-time curves of 29 cycles during aging tests (EIG NCM Li-ion battery, 1C charge/discharge; detail will be discussed in Chapter 4.3). It clearly shows that the measured capacity varies periodically in a certain pattern. The recorded environmental temperature during the tests, i.e. the laboratory temperature, is plotted in Fig. 3.2 bottom part. We can tell from the plot that the laboratory temperature changes regularly every 24 hours. That is because the air conditioner system automatically turns on/off at 6:00 AM and 18:30 PM every day.

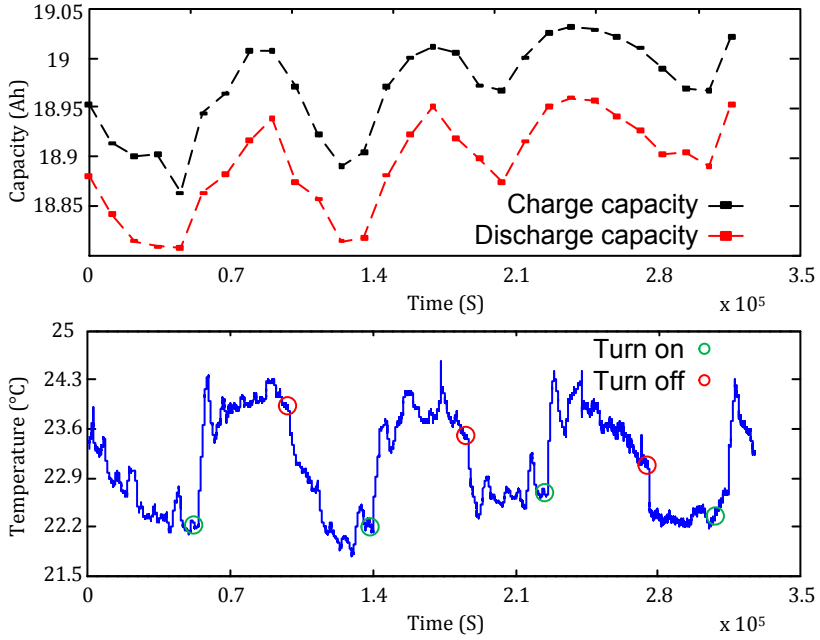

Figure 3.2 Charge/discharge capacity curves in the aging test.

By using statistic tools to analyze these temperature and capacity data, it turns out there is an approximately linear correlation between the capacity and temperature, as

shown in Fig. 3.3. Although the maximum temperature variation is only 4 °C, the capacity variation is up to 0.2 Ah/1%. We may infer that the capacity variation will be larger in a realistic environment.

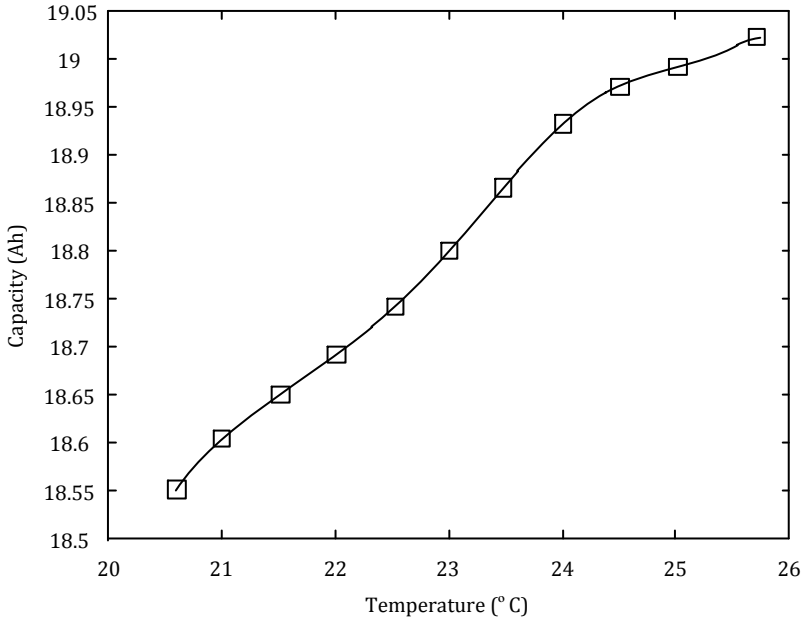

Figure 3.3 Approximate linear correlation between temperature and capacity, derived from the data in Fig. 3.2

This chapter focuses on the temperature influence on Li-ion batteries and associated modeling techniques. A series of experimental tests, including electrochemical and electrical tests, are designed to investigate the temperature influence and build the equivalent circuit model. The heat generation mechanism of Li-ion battery and its relation with SoH is also discussed.

3.2 Temperature Dependent Electrochemical Impedance Spectroscopy Test and Theoretical Analysis

Electrochemical Impedance Spectroscopy (EIS) is an effective electrochemical test tool to analyze the kinetic process of battery [5~6]. The operating principle of EIS is illustrated in Fig. 3.4. A set of sinusoidal current is generated from the EIS equipment and injected into Li-ion battery. Voltage response of the battery is recorded to calculate the battery impedance. The typical frequency range of the EIS test is from mHz to kHz, which associates with different time-scale reaction stages in the battery.

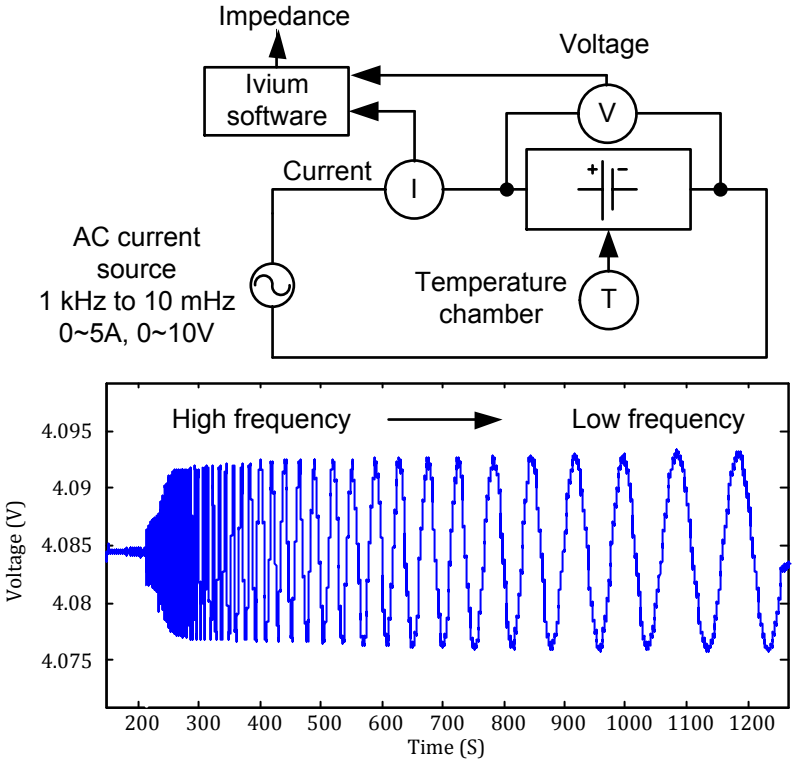

Figure 3.4 Operating principle of EIS equipment (electrochemical workstation, Ivium n-stat, 5A/10V, 0~300kHz) and voltage data in the EIS test.

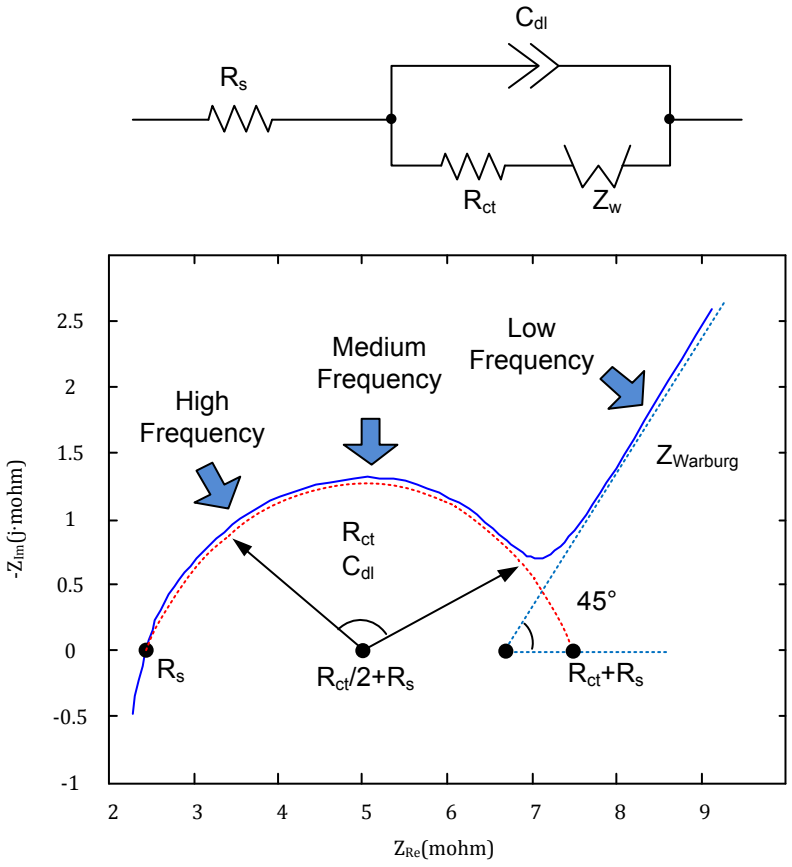

Figure 3.5 Impedance of Li-ion battery in Nyquist form (Bottom) and associated equivalent circuit electrochemical model (Top).

Fig. 3.5 plots a typical EIS test result of an NCM Li-ion battery cell and its equivalent electrical circuit electrochemical model. Notice that in this figure, the imaginary axis is reversed for convenient. The equivalent electrical circuit electrochemical model is usually used to interpret the EIS result and describe the electrochemical reactions. Several factors that determine Li-ion battery performance, including electrode conductivity, charge-transfer rate, diffusion rate and others, can be

expressed by the parameters in the equivalent circuits [45-46]. Some special elements such as constant phase element (CPE) and Warburg impedance are used in the equivalent circuit:

$$Z_{CPE} = \frac{1}{T(j \cdot 2\pi f)^P} \tag{3.1}$$

The CPE is defined by two values: CPE-T and CPE-P. If CPE-P equals 1, then the CPE is identical to a capacitor. When a CPE is placed in parallel to a resistor, a Cole-Element is produced to present the charge transfer process. If CPE-P equals 0.5, a 45-degree line is produced on the Complex-Plane graph. In this study, a CPE with CPE-P value of 0.5 is used to produce the Infinite Length Warburg element. Double layer capacitance C_{dl} and coating capacitance are usually modeled by using the CPE. An electrical double layer exists at the electrode/electrolyte interface. This double layer is formed as ions from the solution approaching the electrode surface. Charges in the electrode are separated from the charges of these ions. The separation is of the order of angstroms. The value of the double layer capacitance depends on many variables including electrode potential, temperature, ionic concentrations, types of ions, oxide layers, electrode roughness, impurity adsorption.

A Warburg element occurs when charge carrier diffuses through a material. In electrochemical systems, diffusion of ionic species at the interface is common. The Warburg impedance is developed to model this phenomenon. Several expressions, based on different assumptions, are used to describe diffusion impedance. Under the assumption of semi-infinite diffusion layer, the impedance is:

$$Z_W = \frac{1}{Y_0\sqrt{j\cdot 2\pi f}} \tag{3.2}$$

where Y_0 is the diffusion admittance. A Warburg impedance is characterized by having identical real and imaginary contributions, resulting in a phase angle of 45 degree, as shown in the right part of Fig. 3.5.

Based on the test frequency, EIS are divided into three parts to express the different processes in the Li-ion battery: high-frequency part, medium frequency part, and low-frequency part. For the high frequency and medium frequency parts of EIS, the semicircle represents the charge transfer process in Li-ion battery. The radius of the semicircle is determined by the Ohmic resistance R_s, double layer C_{dl} and charge transfer resistance R_{ct} in the equivalent circuit. Due to the dispersion effect and other non-ideal characteristics of Li-ion battery, capacitor element cannot be present the C_{dl}. Instead, a CPE is used in the circuit.

The low frequency (10m~1 Hz) part in the EIS represents the material diffusion process in Li-ion battery. It is represented by a slope of approximately 45 degrees in the plot. Typically, Warburg impedance Z_w is used to describe this part. The ion concentration (~1 mole/L) and diffusion coefficient (D~10^{-5} cm2/s) in solvent (ethylene carbonate, EC) is much higher than in intercalation compound (~10^{-2} mole/L, D~10^{-10} cm2/s). Thus, it is considered that Z_w only represents the lithium ion solid diffusion process in the active material.

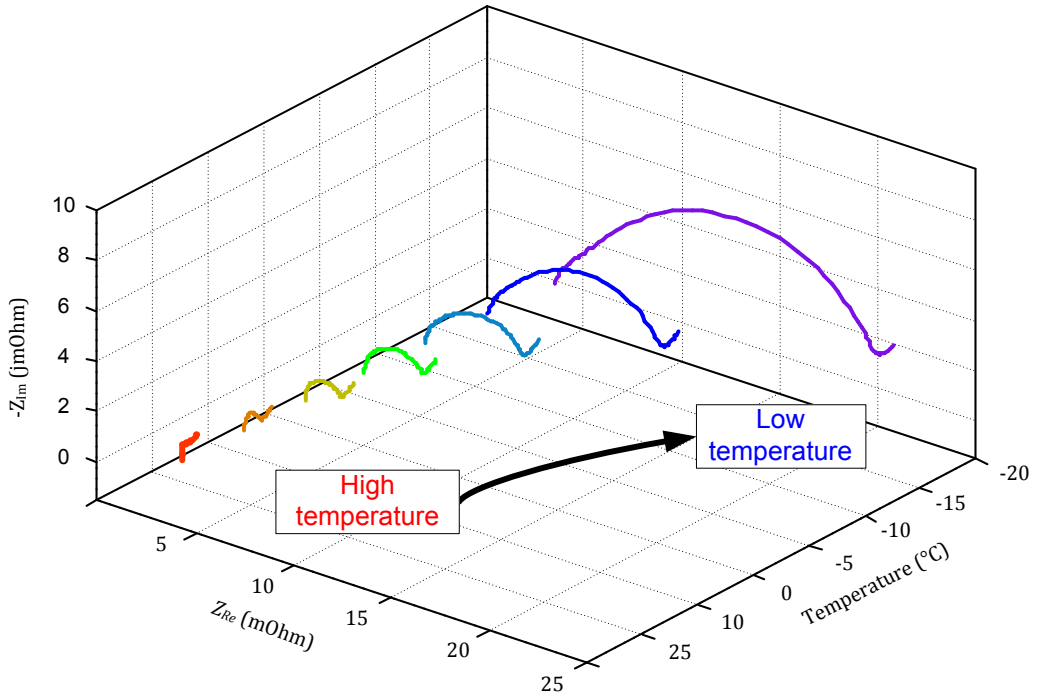

Figure 3.6 EIS test result at different temperatures. AESC LMO battery, SoC=50%.

A series of EIS tests are carried out on AESC LMO battery at different temperatures and SoCs. EIS dispersions are measured and recorded in the temperature range from 25°C to -20°C. The test frequency is from 1k Hz to 10 mHz with five mV AC signal. The LMO battery EIS test result at 50% SoC is plotted in Fig 3.6, with an additional temperature dimension. Significant EIS difference appears when temperature changes, especially in subzero temperatures. The radius of the semicircle exponentially increases when temperature decreases. At lower temperatures, the semicircle shifts to the right side, which means the internal resistance/Ohmic resistance is increased. It can be explained as follows: Materials that compose the Li-ion battery, such as electrode, electrolyte, and

separator, have the semiconductor feature and follow the Ohm's law and Arrhenius type relation:

$$R = \frac{l}{S \cdot \sigma} \tag{3.3}$$

$$\sigma T = \sigma_o e^{\left(\frac{-E_a}{k_B T}\right)} \tag{3.4}$$

where σ is the conductivity of material, l is the thickness of material, σ_o is the pre-exponential factor, E_a is the activation energy/potential, k_B is the Boltzmann constant, and T is the temperature. Substitute eq. (3.3) into (3.4), we can get:

$$R = \frac{lT}{S\sigma_0} e^{\left(\frac{E_a}{k_B T}\right)} \tag{3.5}$$

Write the Logarithm form of both sides of the eq. (3.5):

$$\ln R = \ln \frac{l}{S\sigma_0} + \frac{E_a - k_B}{k_B T} + 1 \tag{3.6}$$

Eq (3.6) clearly shows that ln$R$ is in linear with T^{-1} when the potential E_a is stable. For the charge transfer resistance R_{ct} which determines the radius of the semicircle, it is also temperature dependent. The formula derived from [5] shows that ln R_{ct} and T^{-1} is also in linear relationship:

$$\ln R_{ct} = \ln \frac{R}{n_e{}^2 F^2 c_{max} A_f \left(M_{Li^+}\right)^{(1-\alpha)} (1-SoC)^{(1-\alpha)} SoC^{\alpha}} + \frac{\Delta G - R}{RT} + 1 \tag{3.7}$$

where n_e is the number of transferred electrons, c_{max} is the maximum concentration of lithium ion in intercalation electrode, A_f is the variable related to forward reaction rate, α represents the symmetry factor for the reaction, M_{Li^+} is the concentration of Li-ion in the electrolyte.

The EIS tests results at 5% SoC, 50% SoC and 100% SoC are shown in in Fig. 3.7. Radiuses of the semicircles in these plots are increased at low temperatures. However, for slopes which represent the material diffusion process, the gradients remain the same at different temperatures. It means that the temperature influence on the material diffusion rate is relatively small. Therefore, the charge transfer rate is the primary factor that limits the battery performance at low temperatures [7].

Table 3.1 Identified EIS equivalent circuit parameters at SoC=5%, 50%, 100%.

Temperature	-20	-10	-5	0	10
			SoC=5%		
R_S	$1.67 \cdot 10^{-3}$	$1.83 \cdot 10^{-3}$	$1.99 \cdot 10^{-3}$	$2.19 \cdot 10^{-3}$	$\cdot 10^{-3}$
C_{dl}, T	20	18.55	17.8	16.58	12.93
C_{dl}, P	0.79	0.70	0.65	0.63	0.6014
R_{ct}	$9.33 \cdot 10^{-4}$	$2.22 \cdot 10^{-3}$	$3.91 \cdot 10^{-3}$	$6.64 \cdot 10^{-3}$	$2.46 \cdot 10^{-2}$
Z_w, T	3159	2675	2415	1839	1611
			SoC=50%		
R_S	$2.02 \cdot 10^{-3}$	$2.23 \cdot 10^{-3}$	$2.41 \cdot 10^{-3}$	$2.67 \cdot 10^{-3}$	$3.05 \cdot 10^{-3}$
C_{dl}, T	14.9	12.22	11.96	12.21	12.22
C_{dl}, P	0.87	0.77	0.72	0.68	0.64
R_{ct}	$6.48 \cdot 10^{-4}$	$1.63 \cdot 10^{-3}$	$2.76 \cdot 10^{-3}$	$4.86 \cdot 10^{-3}$	$1.74 \cdot 10^{-2}$
Z_w, T	4777	3721	3315	3042	3013
			SoC=100%		
R_S	$1.91 \cdot 10^{-3}$	$2.06 \cdot 10^{-3}$	$2.19 \cdot 10^{-3}$	$2.42 \cdot 10^{-3}$	$3.17 \cdot 10^{-3}$
C_{dl}, T	18.7	13.9	12.8	12.76	12.15
C_{dl}, P	0.81	0.76	0.72	0.67	0.61
R_{ct}	$6.80 \cdot 10^{-4}$	$1.56 \cdot 10^{-3}$	$2.60 \cdot 10^{-3}$	$4.48 \cdot 10^{-3}$	$1.60 \cdot 10^{-2}$
Z_w, T	2531	1844	1498	1194	813.2

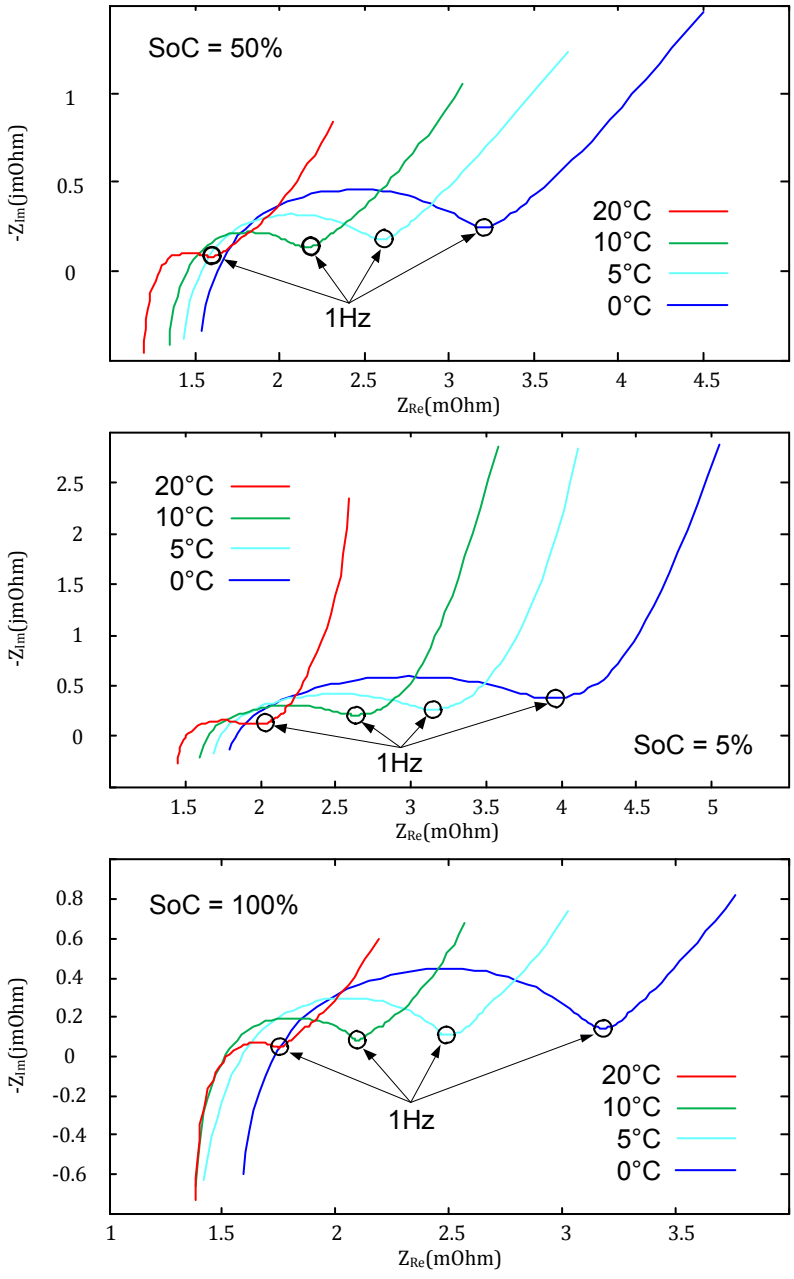

Figure 3.7 EIS test results at different SoCs and temperatures

The equivalent circuit parameters identification results are listed in Table 3.1. The goodness of fitting results is fair. For R_S R_{ct}, C_{dl} T, C_{dl} P, and Z_w T, the fitting errors are

within 2%, 1.8%, 13%, 6.1% and 7.2%, respectively. At SoC=100%, 50% and 5%, the Ohmic resistance R_s and charge transfer resistance R_{ct} as functions of temperature are shown in Fig. 3.8. As expected, these two functions can be fitted by approximately quadratic functions. The growth of R_s is within 200% in the range from 20°C to -20°C. The charge transfer resistance R_{ct} exponentially increases. R_{ct} increases to 2600% at -20° C compare to 20° C.

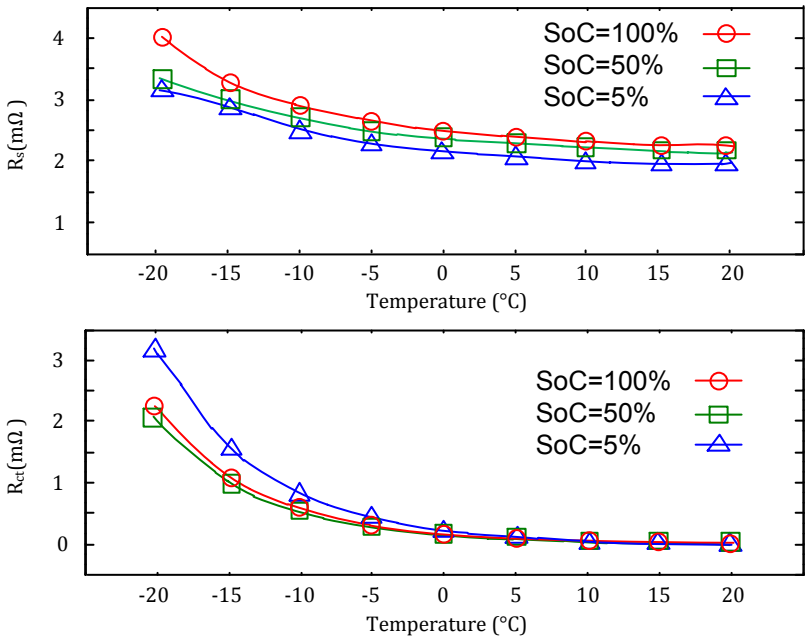

Figure 3.8 Ohmic resistance R_s and charge transfer resistance R_{ct} vs. temperatures at different SoCs

In conclusion, EIS test results show that both Ohmic resistance and charge transfer resistance increase at low temperatures. Moreover, the charge transfer kinetics is the major factor that limits battery performance at low temperatures. Severe polarizations

cause the battery voltage reaches the cutoff voltage earlier at low temperatures and results in capacities losses.

3.3 Temperature Consideration in the Equivalent Circuit Modeling of Li-ion Battery

Since the temperature dependent battery performance have been discussed and explained through EIS test and electrochemical principle in the last section, in this section, a series of temperature tests are carried out to review the consideration in equivalent circuit modeling of Li-ion battery for further BMS application. Temperature compensation functions for equivalent circuit modeling will be given in the analytical form.

Open Circuit Voltage

Open Circuit Voltage (OCV) is the internal potential of Li-ion battery, which can be obtained by measuring the terminal voltage at the no-load condition and chemical equilibrium state. Typically, it takes tens of hours to relax the battery completely after charging or discharging, depending on the battery chemistry type and SoC. For LFP battery, the relaxation time is up to 40 hours. OCV is also considered as the equilibrium potential of the Li-ion battery. According to thermodynamics and electrochemical principle, OCV has the correlation with its temperature. According to the second law of thermodynamics, the potential of a battery is in proportion to Gibbs free energy, while the Gibbs free energy is related to temperature, entropy and enthalpy:

$$\Delta G = n_e F E \tag{3.8}$$

$$\Delta G = \Delta H - T\Delta S \tag{3.9}$$

where G is the Gibbs free energy, E is the potential, H is the enthalpy, T is the temperature, S is the entropy. Substitute (3.8) into (3.9):

$$E = \frac{\Delta H - T\Delta S}{n_e F} \tag{3.10}$$

Eq (3.10) shows that the potential or the OCV of a battery is temperature dependent. However, it is hard to give the quantitative descriptions of the OCV-temperature influence due to various non-ideal effects such lattice defects and complicated chemical characteristics in an actual battery. Therefore, a series of tests are conducted to explore how temperature influences the OCV in practical situations.

First, the battery is discharged to the desired SoC through low current (1/6 C, 5 A) and rest 10 hours to ensure its equilibrium state. Then the battery is placed in the temperature chamber, and the environmental temperature is controlled. Meanwhile, the battery terminal voltage is recorded continuously. The temperature ranges from 20°C to -20°C with 5°C intervals. Measured OCV and temperature data at different SoCs are plotted in Fig. 3.9. The dotted lines in the plots are the fitted voltage response assuming that temperatures are not controlled. Notice that there is slight voltage changing in the fitted data because of the battery is still getting the equilibrium state. These voltage changes are relatively small and can be negligible.

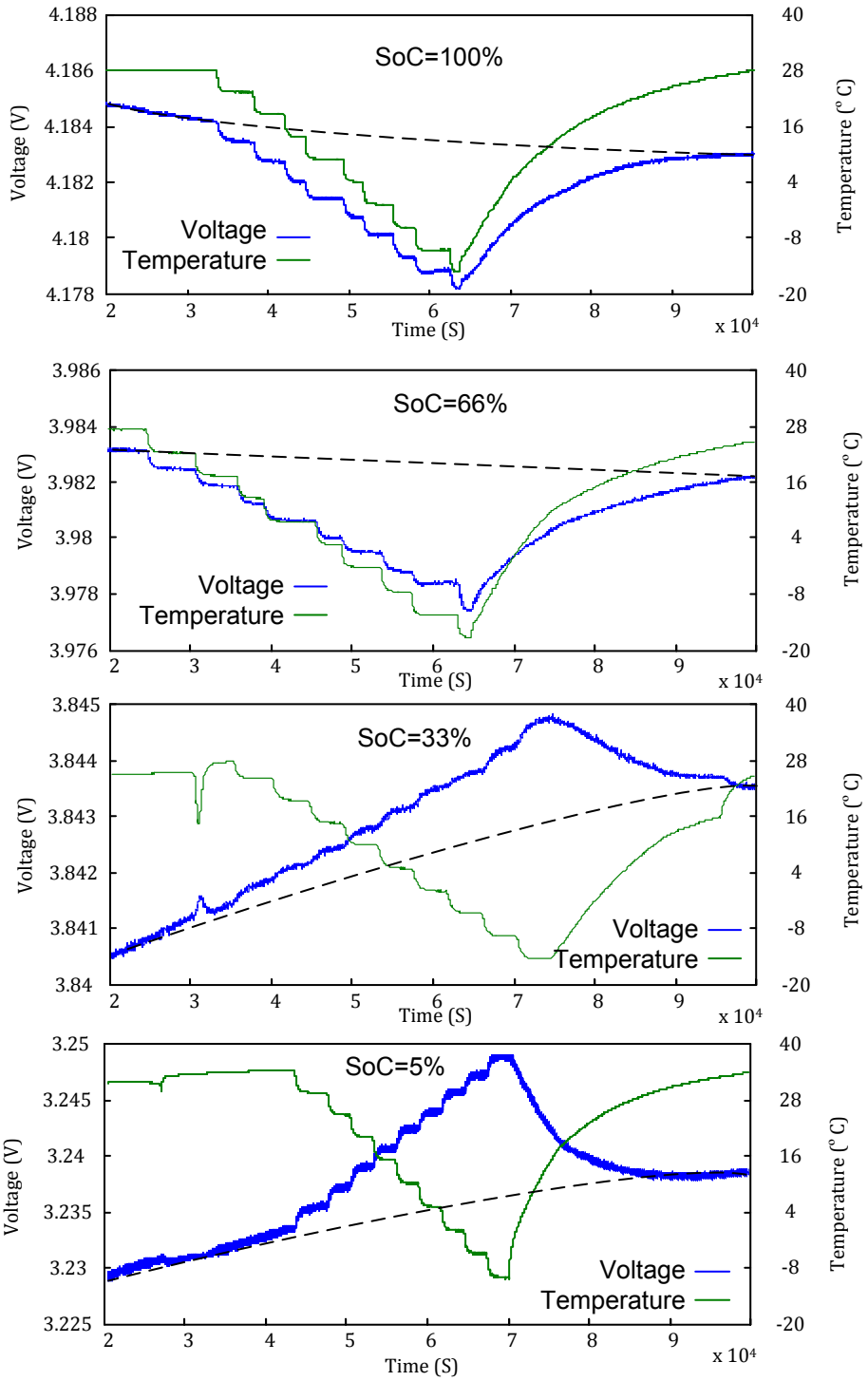

Figure 3.9 OCV~temperature tests at SoC=100%, 66%, 33%, and 5%

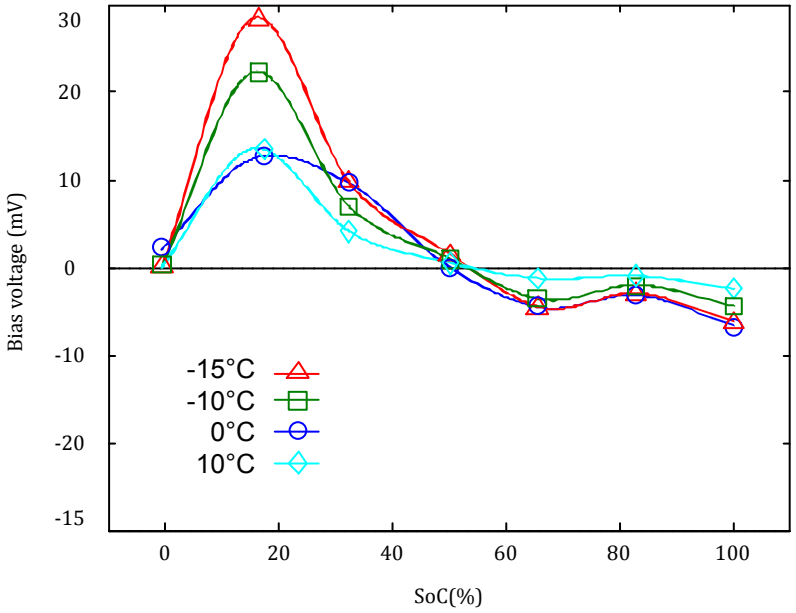

Figure 3.10 Bias voltage of OCV-Temperature

Test results show that the temperature influence to OCV is highly SoC-dependent and nonlinear. At high SoCs, OCVs decrease as temperatures decrease, as shown in Fig. 3.9 upper part. On the contrary, at low SoCs, OCVs increase as temperatures decrease, as shown in Fig. 3.9 lower part. Fig. 3.10 plots the overall map of OCV variation, temperature, and SoC based on the collected data. At low SoCs (10~40%), the OCV variation is as high as 30 mV at -15°C. At high SoCs (60~100%), the OCV variation is within 10mV. Notice that the OCV variations disappear at around 45~55% SoCs.

We may build the analytical OCV-temperature compensation function based on the above test results through nonlinear least squares fitting method. Compared with a look-up table, the analytical expression has superiority in both numerical calculation and

accuracy. Furthermore, the derivative and the Taylor expansion of the analytical expression is easier to obtain for AEKF based SoC estimation, as mentioned in chapter 2. Table 3.2 shows the four typical OCV-SoC analytical functions.

Table 3.2 OCV-SoC analytical functions

#	OCV-SoC analytical function and parameters description
(1)	$OCV = K_0 - \frac{K_1}{SoC} - K_2 \cdot SoC + K_3 \cdot ln(SoC) + K_4 \cdot ln(1 - SoC)$ $\theta = [K_0, K_1, K_2, K_3, K_4]$
(2)	$OCV = K_0 + K_1 \cdot SoC + K_2 \cdot (1 - e^{-K_3 \cdot SoC}) + K_4 \cdot \left(1 - e^{-K_5/(1-SoC)}\right)$ $\theta = [K_0, K_1, K_2, K_3, K_4]$
(3)	$OCV = K_0 - \frac{K_1}{SoC} + K_2 \cdot e^{-K_3/(1-SoC)}$ $\theta = [K_0, K_1, K_2, K_3]$
(4)	$OCV = K_0 + K_1 \cdot SoC + K_2 \cdot SoC^2 + K_3 \cdot SoC^3 + K_4 \cdot SoC^4 + K_5 \cdot SoC^5 + K_6 \cdot SoC^6$ $\theta = [K_0, K_1, K_2, K_3, K_4, K_5, K_6]$

Among these functions, function (4) has the best fitting precision. For actual OCV-SoC curves, the derivative $\mathrm{d}Q/\mathrm{d}V$ is very high at the beginning and end of SoC. Therefore, a high-order polynomial function is more suitable to describe the actual OCV-SoC relation. The fitting parameters results for function (4) are given in Table 3.3

Table 3.3 Parameters fitting results of OCV-SoC function

#	Parameters description
(1)	$K_0 = 0.013505 \cdot \mathrm{T}^2 - 0.5634 \cdot T + 7.429$
(2)	$K_1 = -0.02452 \cdot \mathrm{T}^2 + 1.095 \cdot T - 14.73$
(3)	$K_2 = 0.0085 \cdot \mathrm{T}^2 - 0.4394 \cdot T + 4.999$
(4)	$K_3 = 0.01266 \cdot \mathrm{T}^2 - 0.4583 \cdot T + 8.706$
(5)	$K_4 = -0.01141 \cdot \mathrm{T}^2 + 0.4504 \cdot T - 8.05$
(6)	$K_5 = 0.00326 \cdot \mathrm{T}^2 - 0.1304 \cdot T + 2.614$
(7)	$K_6 = -0.0003 \cdot \mathrm{T}^2 - 0.01204 \cdot T + 3.465$

Internal Resistance

As mentioned in section 3.2, the conductivity of electrode and electrolyte in Li-ion battery decrease at low temperatures. In the point view of battery performance, the internal resistance, or Ohmic resistance, is increased. The battery may reach the cutoff voltage earlier at high rate current and exhibit false capacity reduction. The reserved capacity can be discharged at low rate current. Looking from the perspective of EV applications, the available range can be extended by improving control strategy and using the Hybrid Energy Sources System (HESS) to lower the current rate in the battery. Therefore, to develop advanced HESS and associated control strategy, the Li-ion battery internal resistance temperature variation must be well understood.

The temperature-dependent internal resistance tests can be divided into two parts. Part one is to measure the resistance continuously by injecting current pulses when the

battery is charging or discharging. The Li-ion battery is discharged at a fixed rate of 1/3C and measure the internal resistance every 15 seconds. The current pulse is 2C with 15 milliseconds duration. Due to the short time duration, the measurement error caused by polarization effect is minimized. Fig. 3.11 plots the internal resistance as a function of SoC at different temperatures. Among overall SoC range, internal resistance is relatively flat, except at the SoC of 100%~90% and SoC of 10%~0%.

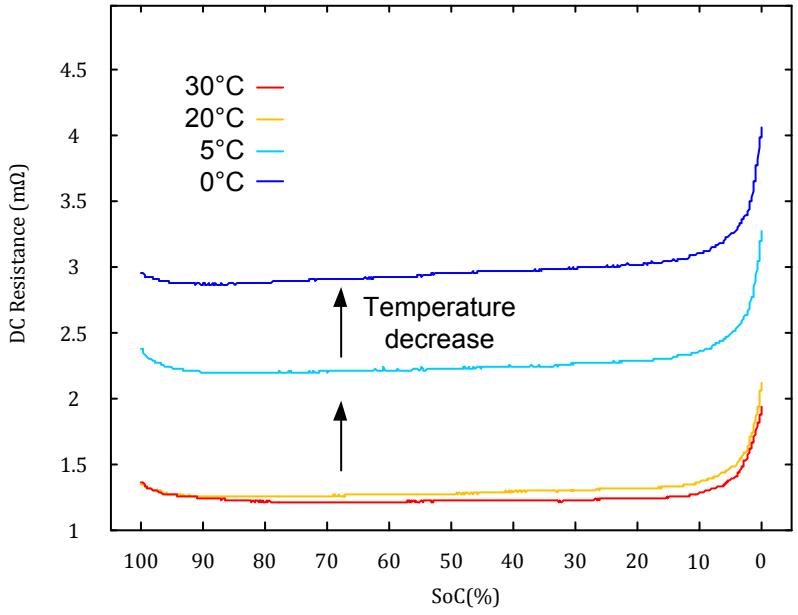

Figure 3.11 Internal resistance vs. SoC at different temperatures.

Part two of test measured the internal resistance at fixed SoC at temperatures from 20° C to -20° C. First, Li-ion battery is discharged to assigned SoCs and rest at least 12 hours to ensure the battery is in a chemical equilibrium state to exclude the polarization effect. Then the battery is placed in the temperature chamber for 2 hours before measuring the

internal resistance. The internal resistance results at different SoCs are illustrated in Fig. 3.12.

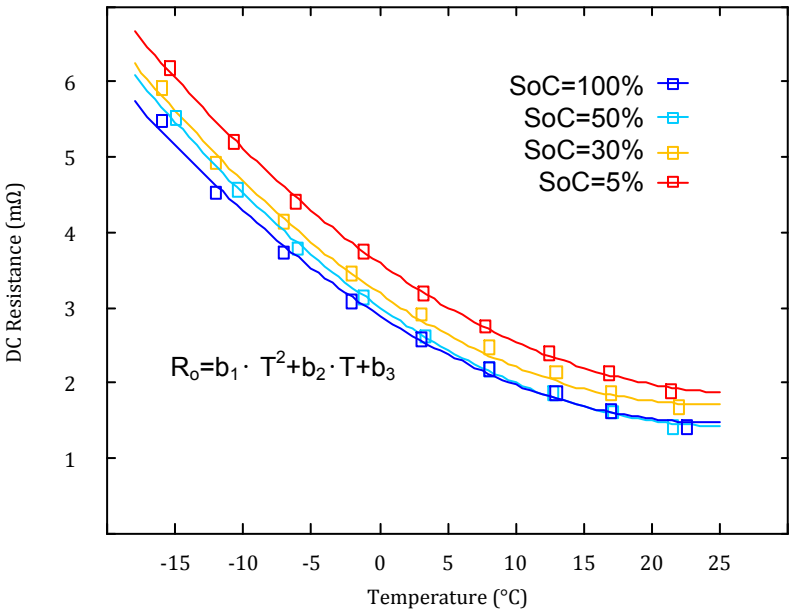

Figure 3.12 Internal resistance vs. temperature at various SoCs.

Based on the test results from the part one and part two, we can conclude that temperature and SoC influence to internal resistance are not correlated. The analytical function of internal resistance can be written as:

$$R_o = \mathrm{f}(SoC, T) = f_{R_o,Soc}(SoC) + f_{R_O,T}(T) \tag{3.11}$$

$$f_{R_o,SoC}(SoC) = \begin{cases} a_1 \cdot e^{(\tau_1 \cdot SoC)} + a_2 \cdot e^{(\tau_2 \cdot SoC)} & SoC > 0.9 \\ a_3 \cdot SoC & 0.1 \leq SoC \leq 0.9 \\ a_4 \cdot e^{(\tau_1 \cdot SoC)} + a_5 \cdot e^{(\tau_2 \cdot SoC)} & SoC < 0.1 \end{cases} \tag{3.12}$$

$$f_{R_o,T} = b_1 \cdot T^2 + b_2 \cdot T + b_3 \tag{3.13}$$

It is noticed that the function $f_{Ro,SoC}$ and $f_{Ro,T}$ are separated. The increasing internal resistance can be calculated individually by measuring the temperature. The test result of Part II signifies that the DC internal resistance increasing at different SoC can be described by a quadratic function $f_{Ro,T}$. It also verified that EIS R_s analysis results in Chapter 3.2. Parameters in the analytical function are given in Table 3.4.

Table 3.4 Parameters fitting results of internal resistance function

a_1	1.921·10-3	b_1	2.263·10-6
a_2	1.596·10-14	b_2	-1.263·10-4
a_3	0.003	b_3	3.776·10-3
a_4	4.642·10-3		
a_5	1.433·10-3		

Polarization effect of Li-ion battery

When Li-ion battery is under charging or discharging at high current rates, its terminal voltage is always higher or lower than the OCV. After charging or discharging is finished, the terminal voltage slowly returns to the new OCV. This phenomenon is due to the polarization effect of the Li-ion battery. The polarization effect is mainly attributed to following reasons: when Li-ion battery is discharging or charging at a high current rate, the electrochemical reaction rate is lower than the electron transfer rate determined by the current. Electrons accumulate in the positive and negative electrodes and then cause the

polarization. If the electrode active material diffusion rate is lower than electrochemical reaction rate, the polarization effect happens too.

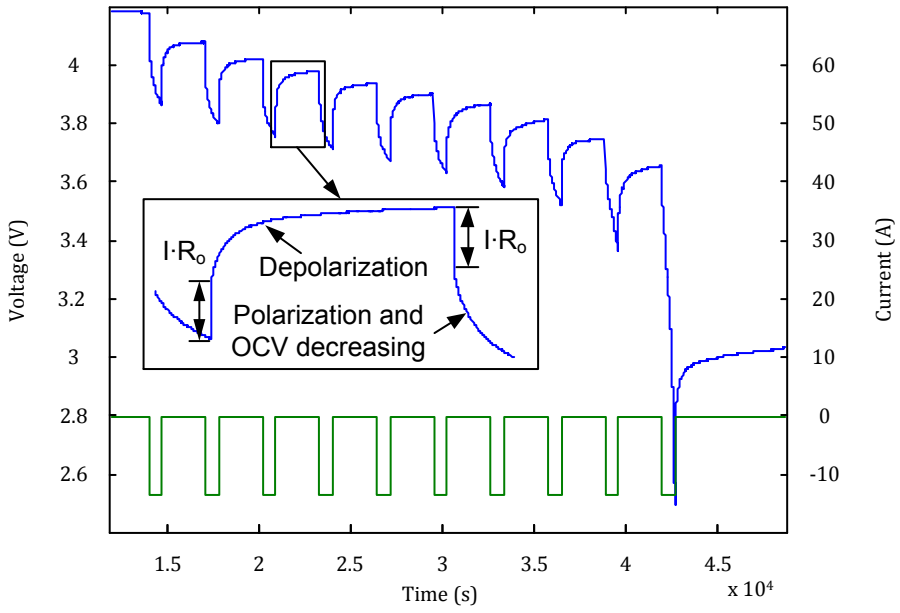

Figure 3.13 Voltage and current in polarization test

Similar to the internal resistance, polarization may cause false capacity losses due to the polarization voltage drop. Furthermore, the charging time of Li-ion battery is prolonged due to the long CV charging stage caused by polarization. As discussed in Chapter 3.2, polarization effect becomes severer when the temperature is low. The following tests are designed to explore the temperature and SOC influence to the polarization: First, fully charge the battery at 25°C. Then remove 10% capacity by 0.5C discharging and rest 40 minutes. Repeat this step until the battery reaches the cutoff voltage. Fig. 3.13 plots the voltage and current measurement in the tests.

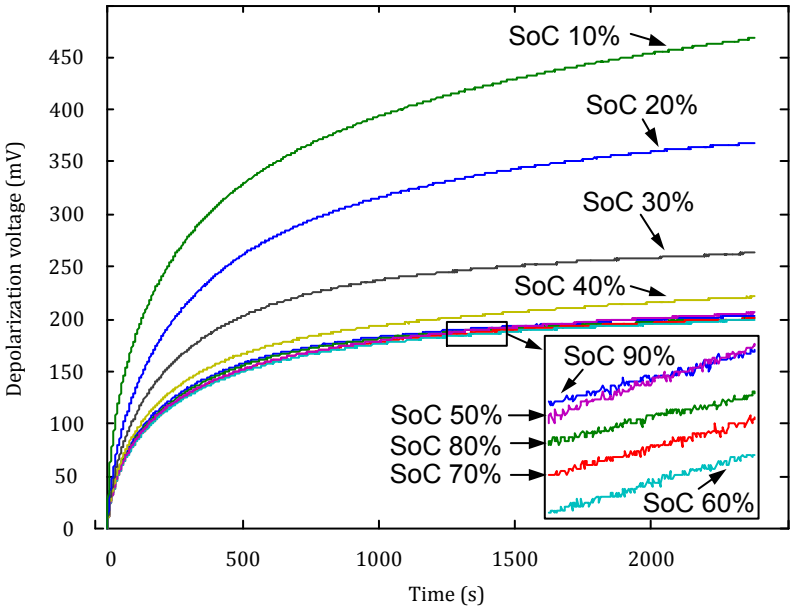

Figure 3.14 Depolarization voltage curve at -20°C

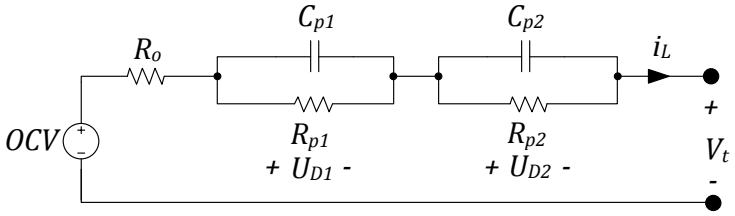

Figure 3.15 Two order RC equivalent circuit Li-ion battery model

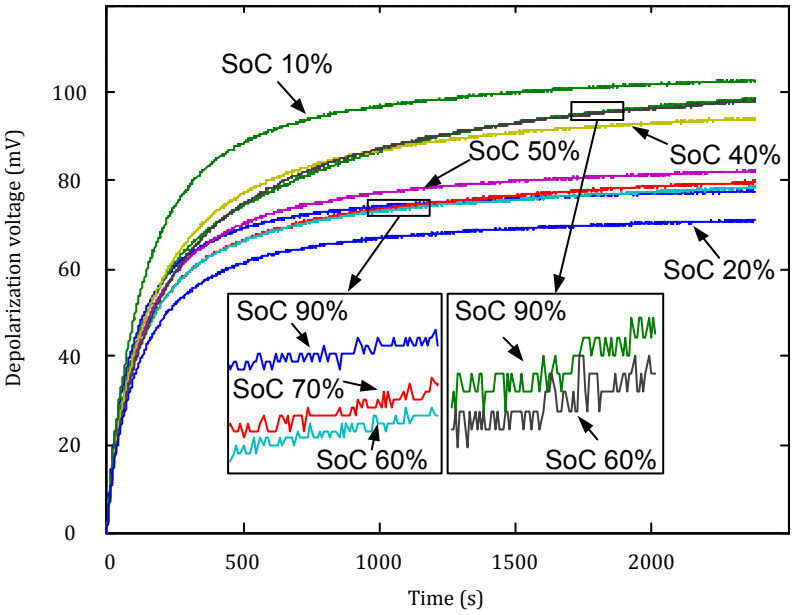

Figure 3.16 Depolarization voltage curve at 0°C

Fig 3.14 and 3.16 show the comparison of depolarization voltage curves extracted from raw voltage data at 0ºC and -20ºC. A two order RC equivalent circuit model shown in Fig 3.15 is used to evaluate the depolarization polarization effect in numerical form. The sum of U_{D1} and U_{D2} represents the polarization voltage and the RC time constant can be used to describe the depolarization speed. In this model, the depolarization voltage f_{U_D} can be calculated when load current is zero (i_L=0):

$$\begin{cases} \dot{U}_{D1} = \frac{U_{D1}}{\tau_1} + \frac{i_L}{C_{p1}} \\ \dot{U}_{D2} = \frac{U_{D2}}{\tau_2} + \frac{i_L}{C_{p2}} \\ V_t = OCV(SoC) - U_{D1} - U_{D2} - R_o \cdot i_L \end{cases} \tag{3.15}$$

$$f_{U_D}(t) = U_{D1} + U_{D2} = \alpha \cdot e^{\left(-\frac{t}{\tau_1}\right)} + b \cdot e^{\left(-\frac{t}{\tau_2}\right)} \tag{3.16}$$

Eq (3.16) shows that the depolarization voltage is the sum of two exponential functions of time. Parameters *a* and *b* are related to the polarization voltage and time constants τ_1 and τ_2 are related to the depolarization speed. For all measured depolarization voltage, the goodness (R-square) of curve fitting is higher than 98%. Therefore, these four parameters can be used to evaluate the polarization accurately. The variables are plotted in Fig. 3.18 and 3.17.

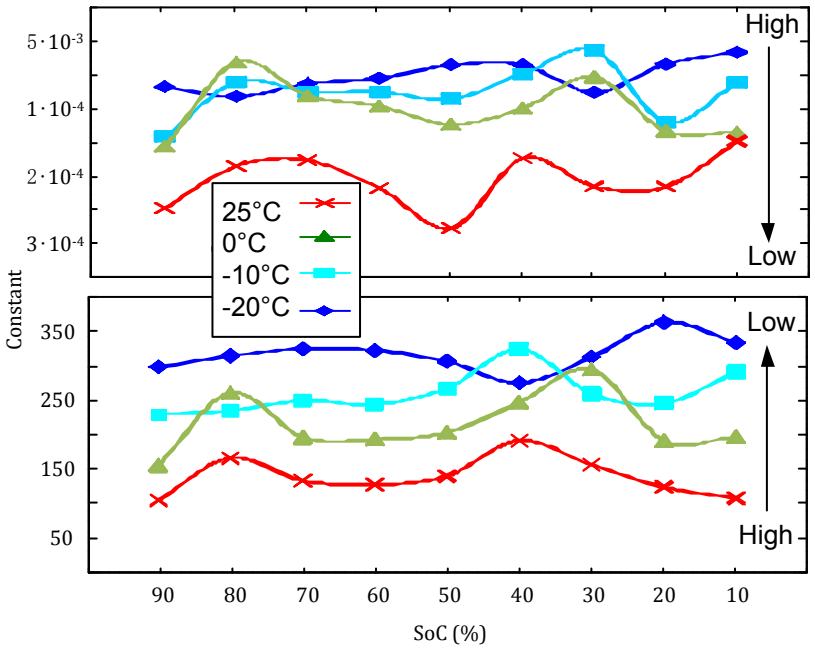

Figure 3.17 Time Constant a (top) and b (bottom) vs. SoC

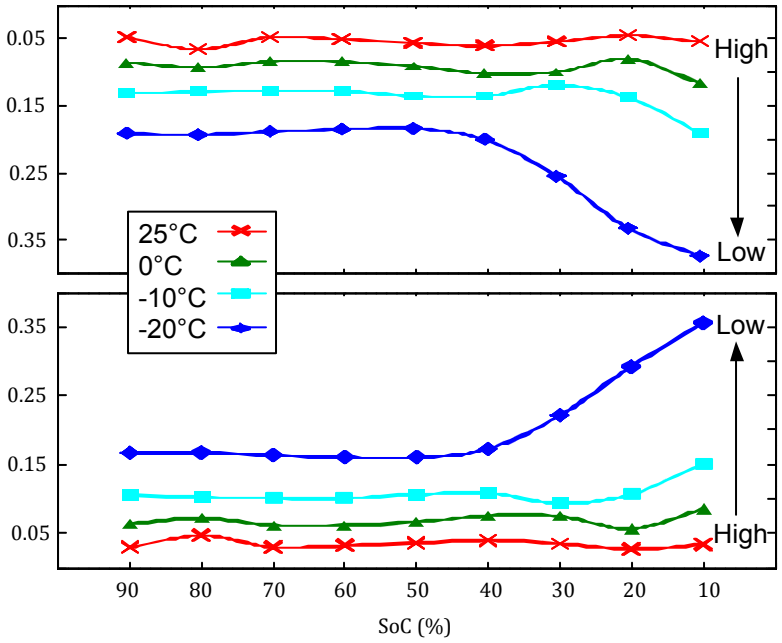

Figure 3.18 Time Constants τ1 (top) and τ2 (bottom) vs. SoC

As shown in Fig. 3.17, parameters *b* and *a* increase linearly with temperature. It indicates that the polarization voltage is in inversely proportional to temperature. It confirms the conclusion in Chapter 3.2. From the aspect of SoC, the correlation between polarization voltage and SoC is not clear at moderate temperatures (above -10°C). However, at low temperatures, the polarization voltage become proportional to SoC when SoC is lower than 50%, as shown in the blue curve in the plot.

For depolarization process, Fig 3.18 also shows a linear relationship between the temperature and time constant τ_1 and τ_2. At high temperatures, the depolarization rate is slightly higher than at low temperatures. However, the relationship between SoC and depolarization rate is not clear.

True capacity loss at low temperature

As mentioned in previous sections, the capacity loss at low temperatures can be attributed to two parts: 1. the false capacity loss caused by internal resistance and polarization; 2. the real capacity loss due to the phase change of chemical material. To investigate the latter one, we conducted the low current ICA test. A tiny current (1/30C) is applied to charge and discharge the Li-ion battery. Thus, the early cutoff voltage reaching due to internal resistance and polarization effect can be minimized. Tests are conducted at three different temperatures: -20°C, 0°C, and 20°C, as shown in Fig. 3.19. At 20°C and 0°C, the charged capacities are very close: 31.001Ah (100%) and 30.975Ah (99.91%), respectively. However, the charged capacity decreases to 28.820 Ah (92.96% of 31Ah) at -20°C.

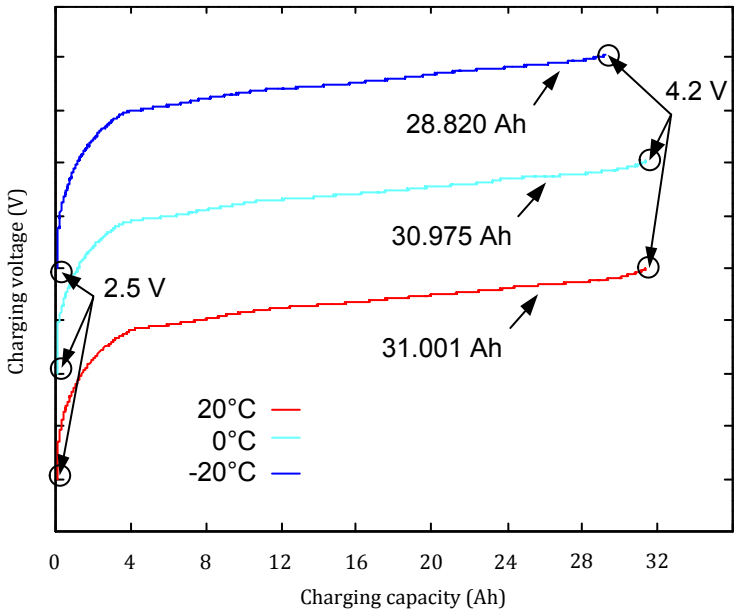

Figure 3.19 Voltage response at low current charging

It is hard to tell the OCV-SoC difference at different temperatures directly. Therefore, the voltage plateau on the charging voltage curve is derived from dQ/dV curve which can be used to identify the staging phenomenon and detect the minor change in OCV-SoC. It is difficult to apply numerical derivative to the raw voltage data directly due to the measurement noise. A series of filtering and fitting are needed to process the raw data. The detail of ICA test will be explained in Chapter 4.5. In this chapter, only the capacity loss part is discussed.

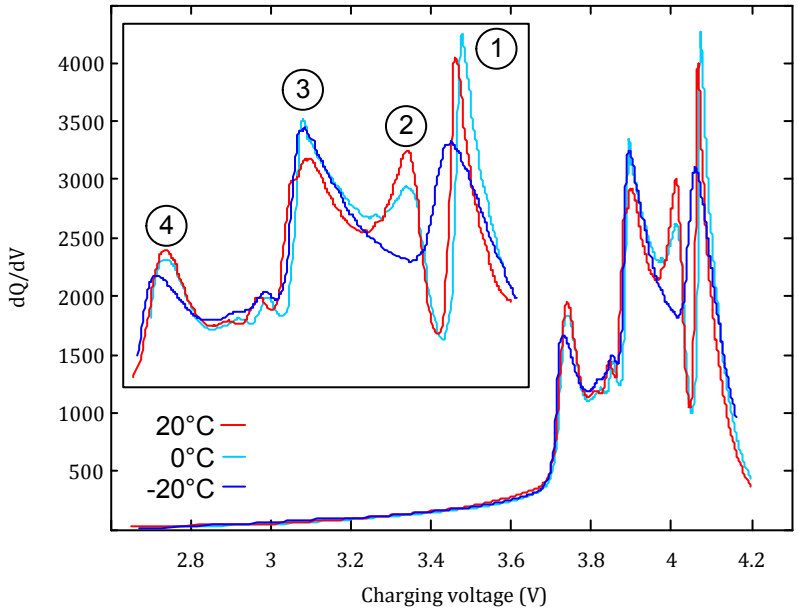

Figure 3.20 ICA test results at different temperature

The derived dQ/dV results are shown in Fig. 3.20. There are clearly 4 IC peaks in the plot at 20°C and 0°C, locate at 3.75V, 3.9V, 4.02V, and 4.07V. These four peaks represent four plateaus in the charging voltage curve, which is hard to observe directly from the

OCV-SoC curves. For ICA test result at -20°C, it shows that the IC peak #4 and IC peak #3 remain the same as the peaks at 20°C and 0°C. However, peak #1 and peak #2 are distorted and combined into one peak at 4.05V. The difference between these ICA results may be considered as the indications of real capacity difference. Unfortunately, there is no theoretical discussion about this phenomenon published.

Fast charging at low temperature

Some fast charging methods and standards such as the “Supercharger”, “SAE J1772 DC level III” and “CHAdeMo”, are developed to improve the charging speed. They claim that more than 80% capacity can be charged within 30 minutes [8]. A series of charging tests is carried out to investigate the temperature influence on fast charging. The charging current is set to 2C and charging time is limited to 30 minutes. Ideally, 100% capacity can be charged into the battery.

As shown in Fig. 3.21, more than 90% capacity can be charged into the battery at 25°C. At lower temperatures, the charging capacity reduced significantly: only 63% capacity is charged into battery. It can be explained that increased DC internal resistance and polarization effect made the battery reaches the cut-off voltage earlier and limited the charging current. From the battery chargers aspect, constant voltage (CV) charging mode will be applied earlier, so that the output power will drift away from the optimum operation point.

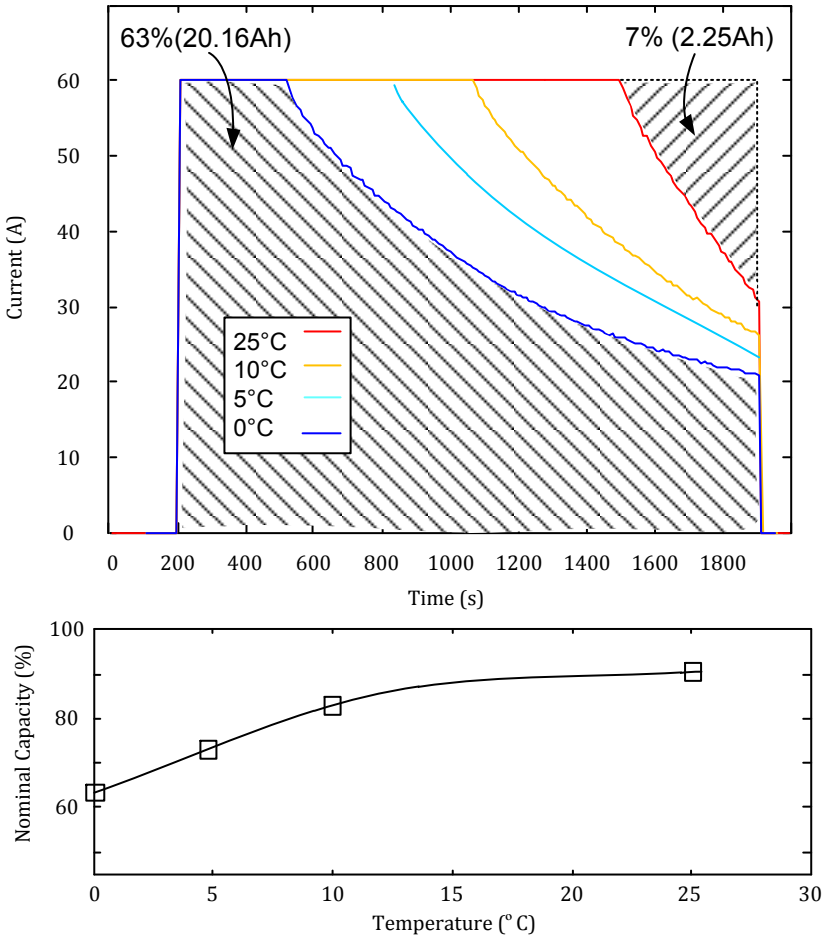

Figure 3.21 Charged capacity by using 2C fast charging tests at different temperature

3.4 Summary

In this chapter, we focus on the study of temperature influence to Li-ion battery. First, the temperature dependent performance of the battery is studied through EIS tests and theoretical analysis. It suggests that the Ohmic resistance and charge transfer resistance increasing at low temperature are the major limitation factors. Next, a series of experimental test are conducted to find out the temperature consideration in equivalent

circuit modeling and to build temperature compensation functions. It is found that the temperature influence to OCV-SoC curves is highly nonlinear and SoC dependent. Both internal resistance and polarization resistance are increased significantly at low temperature. The fast charging ability of Li-ion at difference temperatures is also investigated.

CHAPTER 4

Aging effect in Li-ion Battery Modeling and State-Of-Health Estimation

4.1 Background

As the vehicle service time increase, the performance of EV will gradually decrease due to the Li-ion battery aging/degradation problem. In general, the capacity and power capability are the main indicators to evaluate the performance of Li-ion battery. For EV applications, capacity losses cause the reduced available mileage and the decreasing of power capability harms vehicle's acceleration and regenerative brake ability. The Li-ion battery aging problem not only involves with the fault diagnostic, prognostic and maintenance of vehicles but also is related to vehicle control strategy and power management.

As we discussed in Chapter 2, the performance of SoC estimation algorithm mainly relies on the accuracy of Li-ion battery model. Models considering the aging effect could dramatically improve estimation accuracy results and robustness of the algorithm. To do that, the SoH which is used to describe the aging level of Li-ion battery must be provided. SoH is usually defined as the actual battery capacity divided by the nominal capacity [14] provided by manufacturers. However, this simple definition is not applicable in EV applications.

Capacity measurement, impedance measurement, parameter estimation, and the coup de fouet methods have been used to estimate the SoH. Capacity measurement requires

discharging and charging the battery to 0%/100% SoC, which is impractical for the EV applications. Battery impedance measurement has been widely used in industry. It employs dedicated hardware and software to measure the DC or AC impedance of the battery [44, 45] directly. The battery impedance is correlated to SoH. However, the cost and invasiveness of impedance measurement prevent its use in the EV applications. Coup de fouet [46, 47] is observed in Lead-Acid batteries that have been fully charged, rested and then pulse discharged. During the first discharge pulse, the voltage dips, increases, levels off at a plateau voltage and then decreases steadily. The voltage dip or undershoot has been shown empirically to be proportional to the battery capacity and SoH [48, 49]. The electrochemical mechanism behind coup de fouet is still not understood [46] and the requirement of full charge followed by rest limits its utility. Parameter estimation methods are suitable for dynamic applications such as EV applications. The estimated parameters are for specific simplified models of the cell electrochemistry so that they are explicitly related to the geometric, material, and electrochemical parameters of the underlying model. Thus, changes in the parameter estimates are explicitly correlated to specific degradation mechanisms and empirically correlated to the SoH. A variety of parameter estimation methods, including Subspace Identification [50, 51], Kalman Filtering [33, 52], Fuzzy Logic [53], and Least Squares [54], have been applied to Li-ion [36, 54], Ni-MH [33], and Lead-Acid [50, 52] batteries. The Least Squares Method (LSM) [55] is used in the present work because of its simplicity, computational efficiency, and guaranteed convergence. In [54], this method is used to estimate the coefficients of a

reduced order Li-ion battery model [56] and track the evolution of multiple parameters, including the capacity, diffusion time constant, and impedance.

4.2 Li-ion Battery Aging Mechanism

It not only requires lots of experimental data to build the practical models considering the aging effect but also the theoretical understanding of aging mechanism. Schlasza et al. [17] presented a review of known Li-ion battery aging mechanisms using the failure mode and effects analysis method, which categorized them and established the relationship between failure effects and causes. Wang et al. [18] summarized the failure modes in three types of batteries in electric vehicle applications. Vetter et al. [19] discussed the main aspects of Li-ion battery aging mechanisms, which include aging of carbonaceous negative electrodes, lithium metal oxide positive electrodes and electrolyte. These researchers indicated that the key of understanding the aging process is the various aging aspects in both chemical side and physical side.

A Li-ion battery has to work within a certain electrochemical window to ensure the chemical stability. That is the voltage of Li-ion battery should not exceed the certain upper and lower limits. The upper cutoff voltage is determined by the electrochemical window of organic electrolyte [20]. The lower cutoff voltage is determined by the reduction potential of positive electrode material. When overcharge occurs, the organic electrolyte solvent decomposes at the positive electrode due to oxidization. It lowers the ion conductivity of electrolyte and causes server polarization. Furthermore, the

decomposition of electrolyte generates the heat and gasses. From the point view of the electric vehicles, the battery power capability is reduced due to the polarization. When the Li-ion battery is over-discharged, the over reduction reaction happens to the transition metal ions at the positive electrode. The original lattice structure is damaged, which cause the capacity loss [21]. Fig. 4.2 shows the main aspects of Li-ion battery aging mechanisms.

During the normal use, the strain of lattice is the leading cause of Li-ion battery degradation [22]. The lattice defect also lowers the ion diffusion rate. At the carbon graphite negative electrode, the layer lattice structure is only bonded by the Van der Waals' force. The intercalation and deintercalation of ions could easily damage the lattice structure and cause the loss of original SEI. The new SEI will grow on the surface of the electrode and consume the electrolyte. Moreover, the high temperature will cause the SEI accelerated growing and decomposition. Li-ion battery contains lots of flammable organic material. Once fire or explosion happens to one cell, the entire battery pack can be burnt down in a short time [23]. Fig. 4.1 shows the photo of failed NCM battery and

LFP battery.

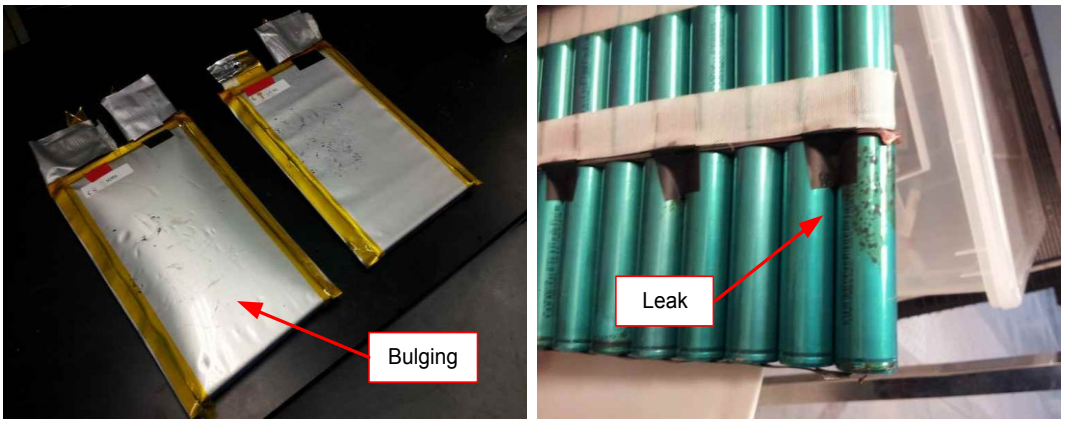

Figure 4.1 Failed NCM battery (left) and LFP battery (right)

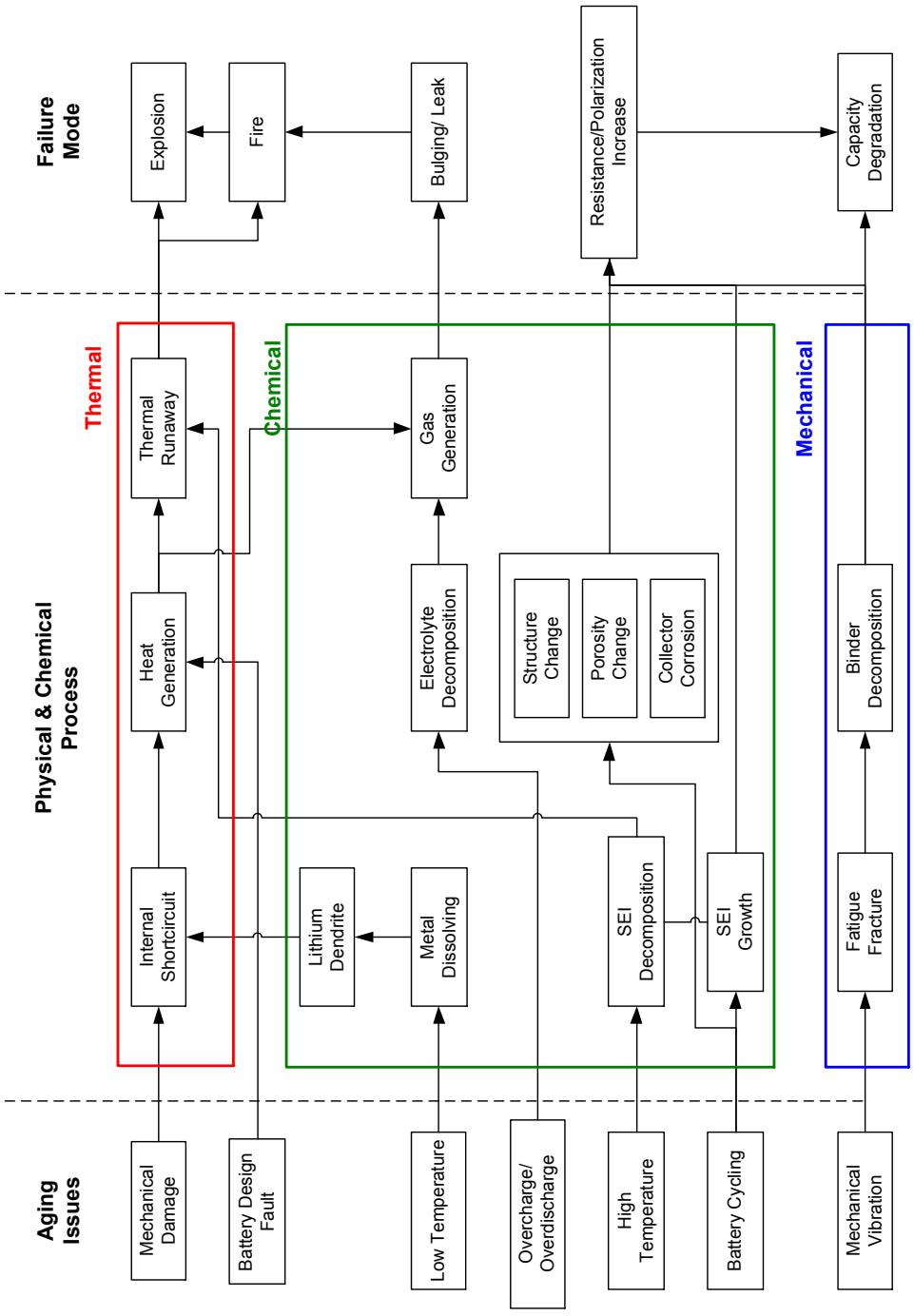

Figure 4.2 Main aspects of Li-ion battery aging mechanisms

4.3 Experimental Study of Li-ion Batteries Aging Tests

In this study, five types of Li-ion batteries are selected as the experimental subjects, as shown in Table 4.1 and Fig. 4.3. Three main Li-ion battery chemistry types including Lithium Iron Phosphate, Lithium Ni-Co-Mn Oxide, and Lithium Manganese Oxide are included. All of these batteries are designed for EVs application. Particularly, part of the LFP batteries (A) and NCM batteries (D) are disassembled from used EVs that have been tested for more than two years. These aged batteries are great experimental subjects to investigate the aging problem and verify the states estimation algorithms.

A series of aging tests are designed and carried out to collect the aging data of Li-ion battery. The test plan is described in the flow diagram shown in Fig. 4.4. First, the characteristics of the fresh battery are identified through a set of tests, including capacity test, internal resistance test, HPPC test, UDDS test and incremental capacity test. Then the Li-ion battery impedance is obtained by using IVIUM n-stat electrochemical workstation. Finally, three different aging tests are carried out to explore the influence of operating patterns to the battery aging. The aging test repeats until reaching a certain cycle number or the appearance of significant capacity loss.

A. Valence
(d)18mm*65mm
40 g

B. A&S
7.3mm*65.5mm*132.5mm
150 g

C. EIG
217mm * 129mm * 7.2mm
428 g

D. Electrovaya
240mm * 140mm * 10mm
928 g

E. AESC
290mm * 216mm * 9mm
790 g

Figure 4.3 Experimental Li-ion batteries A~E

Table 4.1 Datasheets of 5 different Li-ion batteries

	Chemistry Type	Capacity	Voltage Range	Package
A	Lithium iron phosphate (LPF)	1.2Ah	2.5V to 3.65V	18650
B	Lithium iron phosphate (LPF)	5Ah	2.0V to 3.65V	Prismatic
C	Lithium Ni-Co-Mn Oxide (NCM)	20Ah	3.0V to 4.15V	Prismatic
D	Lithium Ni-Co-Mn Oxide (NCM)	30Ah	3.0V to 4.05V	Prismatic
E	Lithium Manganese Oxide (LMO)	32Ah	2.5V to 4.2V	Prismatic

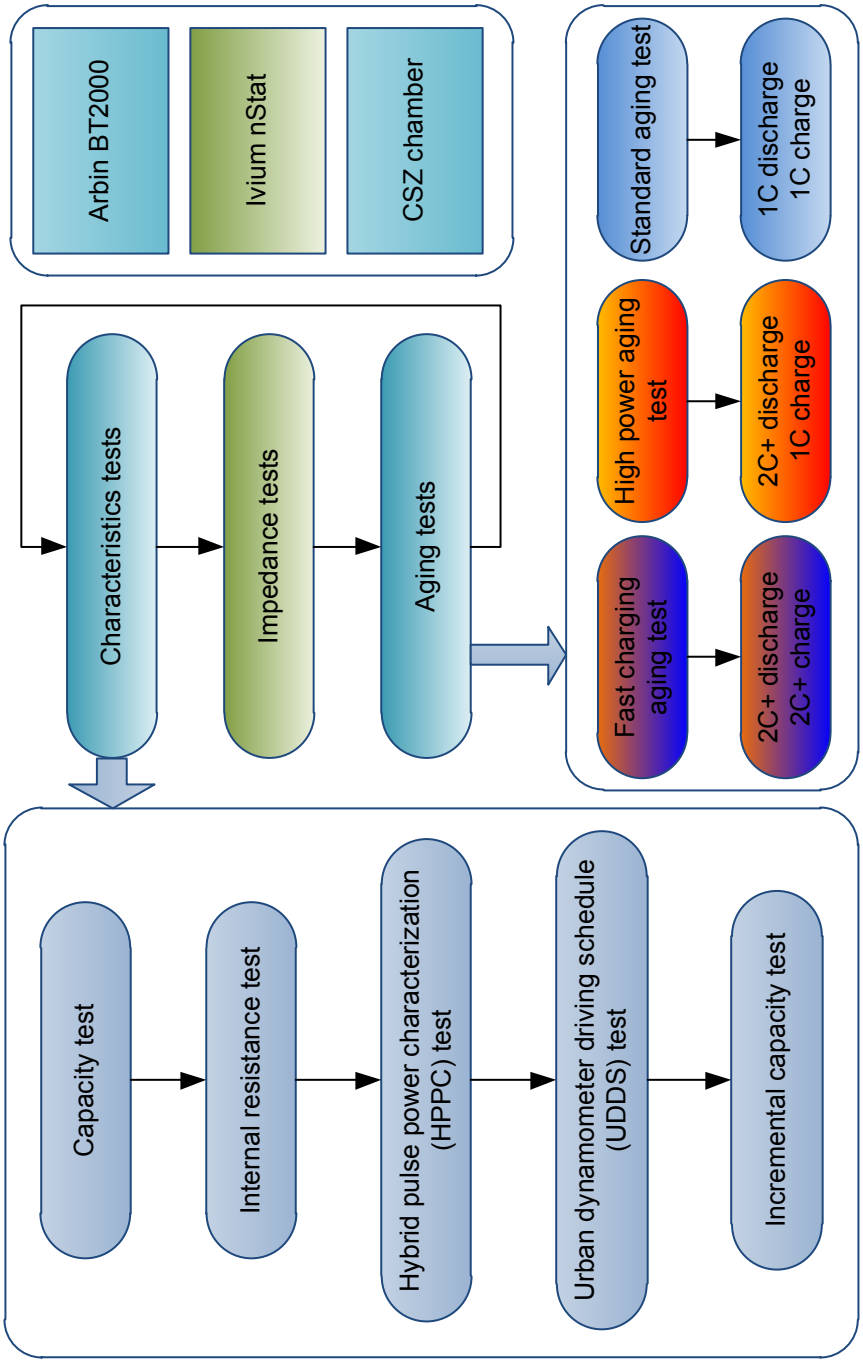

Figure 4.4 Li-ion battery aging tests flowchart

As demonstrated in Fig. 4.4, capacity test follows the standard test procedure in the datasheet of Li-ion battery. First, a fresh battery is discharged to the cutoff voltage at 0.5 C current to remove the initial residual capacity. The typical residual capacity is around 50% of nominal capacity due to the safety requirement of shipping and storage. Then charge the battery to full in CCCV (1/20 C cutoff current) mode after one-hour rest. Finally, repeat above test three times to obtain the average capacity of the battery.

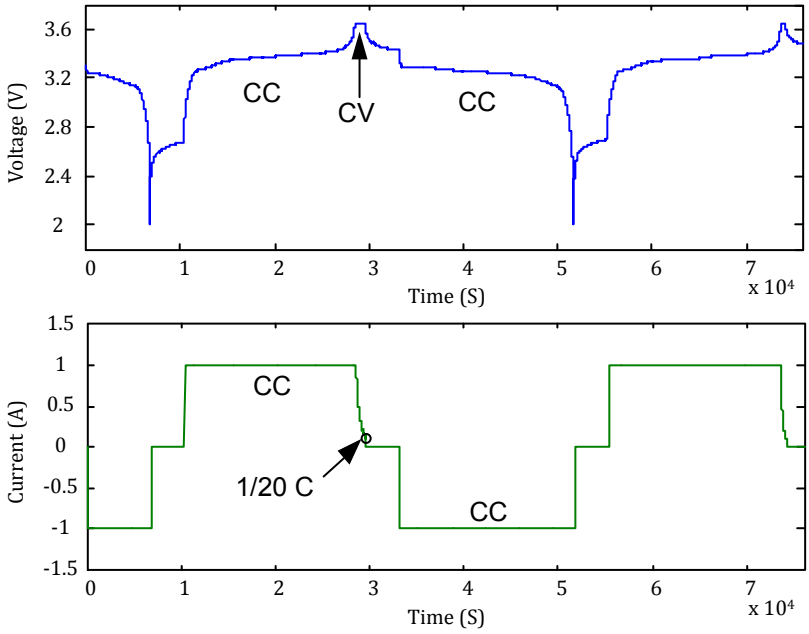

Figure 4.5 Voltage and current in the capacity test

The internal resistance test uses the pulse function of Arbin BT 2000 to measure the Ohmic resistance. Due to the very short pulse time (30 μs), the polarization resistance is eliminated from the measurement result, and the battery SoC is not changed. During the 0.5C constant current discharging, Ohmic resistance is measured every 15 seconds to

obtain the continuous Resistance-SoC function. Fig. 4.6 shows the voltage response and resistance measurement result of the test. Notice that the voltage impulse appears every 15 seconds and the impulse does not influence the voltage response during constant current discharging.

The incremental capacity (ICA) test uses extreme low current (e.g. 1/20 C) to charge or discharge the battery and obtain the approximate dQ/dV curves for SoH estimation. The detail of ICA test will be discussed in chapter 4.5. The sampling rate should be high (>5Hz) in this test due to the low charging current.

When all characteristics tests are finished, the Li-ion battery is moved to the IVIUM nStat electrochemical workstation to conduct EIS test. The detail of EIS test has been discussed in Chapter 3.2.

There are three different aging tests, including standard aging test, high power aging test and fast charge test. The standard aging test follows the test procedure described in the datasheet, which is to cycle the battery at 1C rate for CC discharge and CCCV charge. The high power aging test discharge the battery with high current rate (2~5C) and use 1C current to charge the battery without CV stage. In the fast charging aging test, both discharge current and charge current are set to the maximum allowed value in the datasheet.

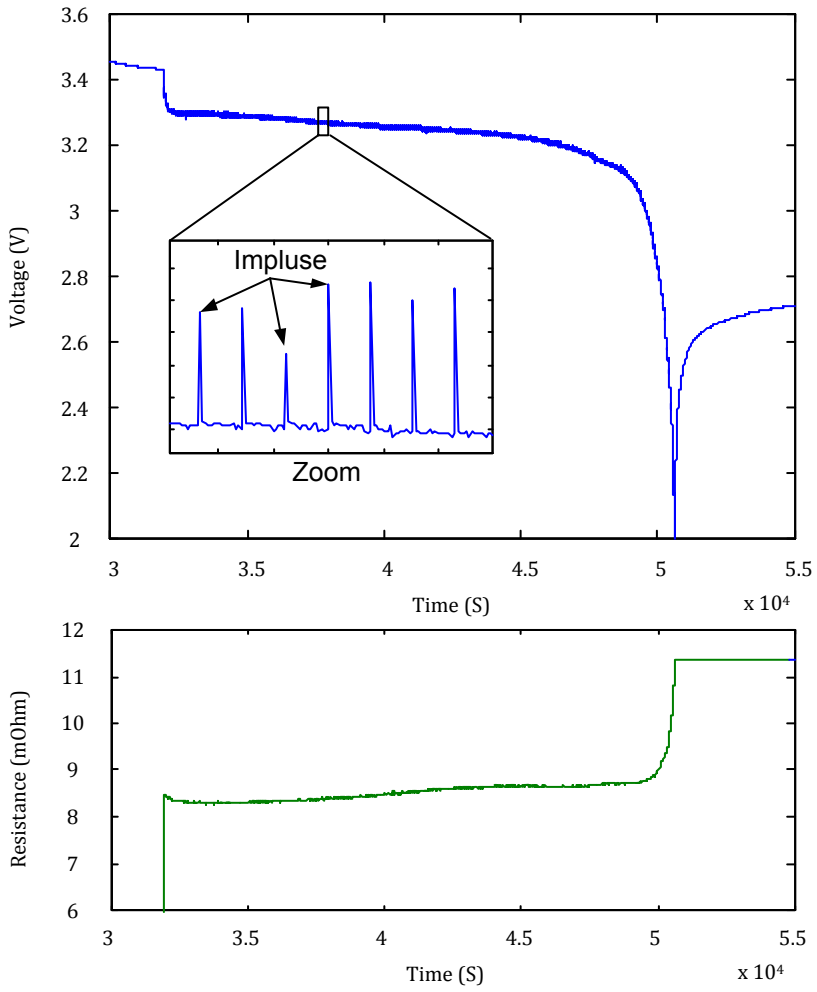

Figure 4.6 Ohmic resistance measurement based on current pulse method

A piece of typical voltage and current data of A&S LFP Li-ion battery (5Ah) under standard aging test are plotted in Fig. 4.7. First, the battery is discharged to cutoff voltage (2.0V) at 1C (-5A) rate. After 5 minutes rest, 0.5C (2.5A) rate is used to charge the battery in CCCV mode.

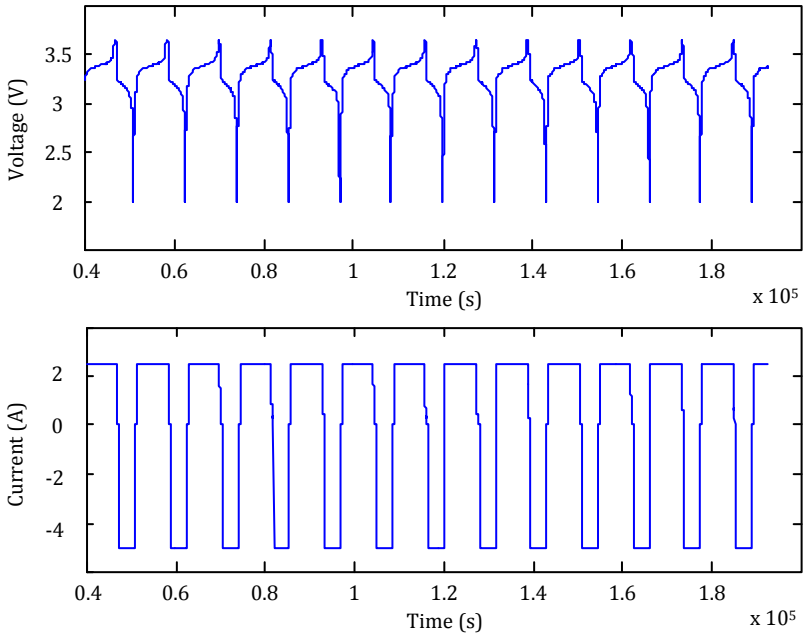

Figure 4.7 Voltage and current in standard aging tests

Results and Discussion

The general status of aging test plan is illustrated in Table 4.2. It is noticed that only a few aging tests are carried out on type A and type E batteries.

Table 4.2 Summary of Li-ion battery aging tests

Battery Type	Capacity	Standard aging	High power	Fast charge
AESC (LMO)	32Ah	400 cycles	500 cycles	N/A
Valence (LFP)	1.5Ah	650 cycles	N/A	N/A
A&S (LFP)	5 Ah	1200 cycles	N/A	N/A
EIG (NCM)	20 Ah	1300 cycles	1300 cycles	350 cycles
Electrovaya (NCM)	30 Ah	100 cycles	N/A	N/A

For the EIG NCM battery, five cells (#1, 2, 3, 4, and 5) are selected to conduct all three aging tests separately. Cell #1 and #2 are cycled 1300 times of high power aging tests. The capacity degradation during cycling is shown in Fig. 4.8. Notice the high power aging tests only charge the battery in CC mode without CV stage. Therefore, the depth of discharge (DoD) in this test is around 85% (17Ah/20Ah).

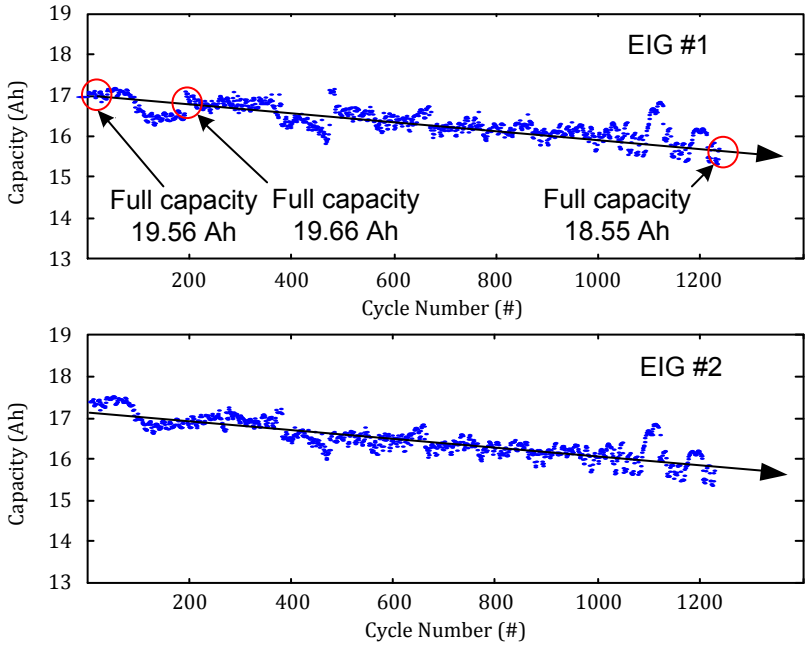

Figure 4.8 Capacity vs. cycles of cell EIG #1and #2, 1C charge 2C discharge.

The full capacity (0.5C discharge, 0.5C charge CCCV) of the fresh cell EIG #1 before cycling was 19.56 Ah. After 200 cycles, the full capacity slightly increased to 19.66 Ah, which is due to the electrode material are being slowly activated at the beginning stage of life. After 1300 cycles, the full capacity of EIG #1 remains 18.55 Ah. The capacity loss is within 10% compare with the fresh cell (18.55Ah / 19.56Ah). The

internal resistance-SoC curves of fresh and aged EIG #1 are plotted together in Fig. 4.9. It shows that, after 1300 cycles, the internal resistance of EIG #1 remains similar to the fresh state.

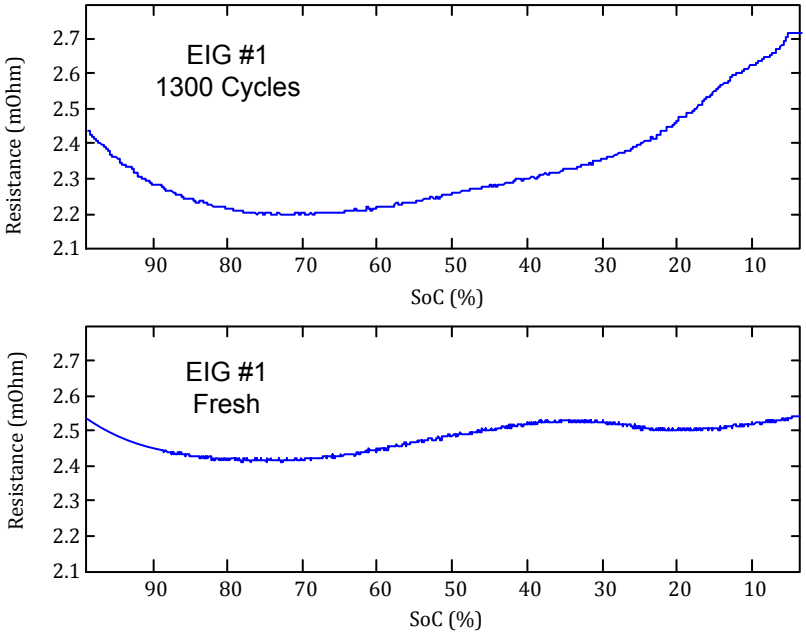

Figure 4.9 Internal resistance vs. SoC of EIG #1 after 1300 cycles and fresh state.

Cell EIG # 3 is cycled 1300 times of standard aging tests. Fig 4.10 plots the capacity of each cycle in the tests. Notice that the capacity is increased at the first 200 cycles, which is similar to EIG#1 and #12. After 300 cycles, capacity gradually decreased to 16 Ah. Then the capacity starts to drop quickly after 1200 cycles, as shown in the red circle in Fig. 4.10. Because of the significant capacity loss, the cycling test of EIG #3 stopped at 1250 cycles when the rest capacity is around 9 Ah. The internal resistance of EIG #3 at 900, 1100, 1200 and 1250 cycles are plotted in the Fig. 4. 11. The internal resistance

increasing only happens after 900 cycles and the increasing rate also becomes larger when the battery approaches the end of life. The increased internal resistance from cycle 1100 to 1200 (0.4 mOhm) is larger than the total increment from cycle 0 to 1100 (0.2 mOhm). Finally, the internal resistance becomes four times larger (8 mOhm) than the fresh battery.

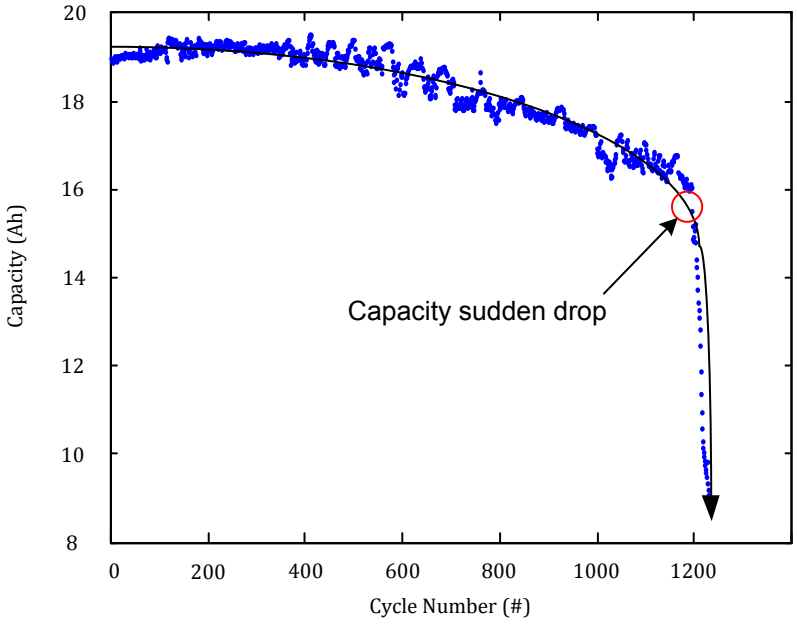

Figure 4.10 Capacity vs. cycles of cell EIG#3, 1C charge, and 1C discharge.

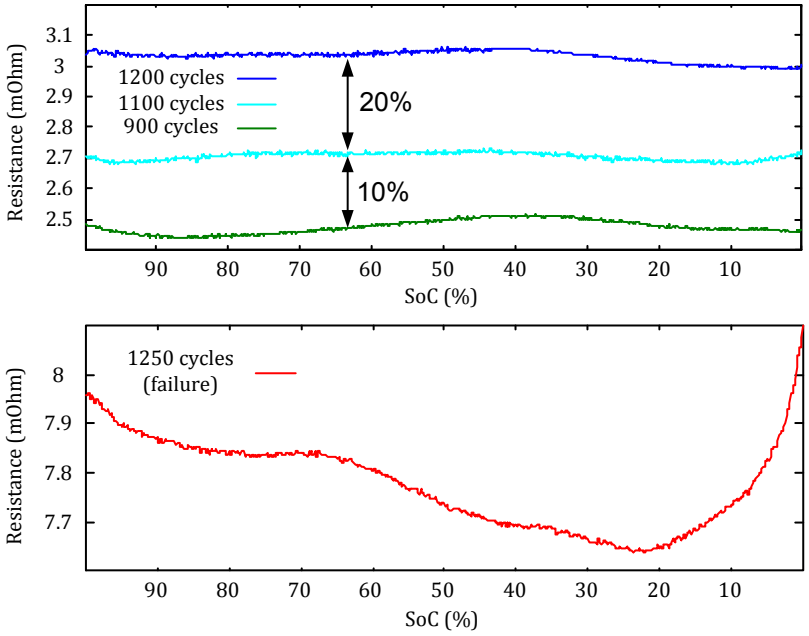

Figure 4.11 Internal resistance vs. SoC of EIG#3 at 900, 1100, 1200 and 1250 cycles.

Cell EIG#4 and EIG#5 are cycled 370 and 330 times of the fast charging test. Notice that the only difference between the fast charging test and high power test is the different charging current rate. The charging current in fast charging test is 2C without CV stage. Fig 4.12 plots the capacity of each cycle in the tests. The capacity degradation pattern is similar to the standard test in Fig. 4.10. In the fast charging tests, the capacity dropping happens at around 300 cycles for cells EIG#4 and #5.

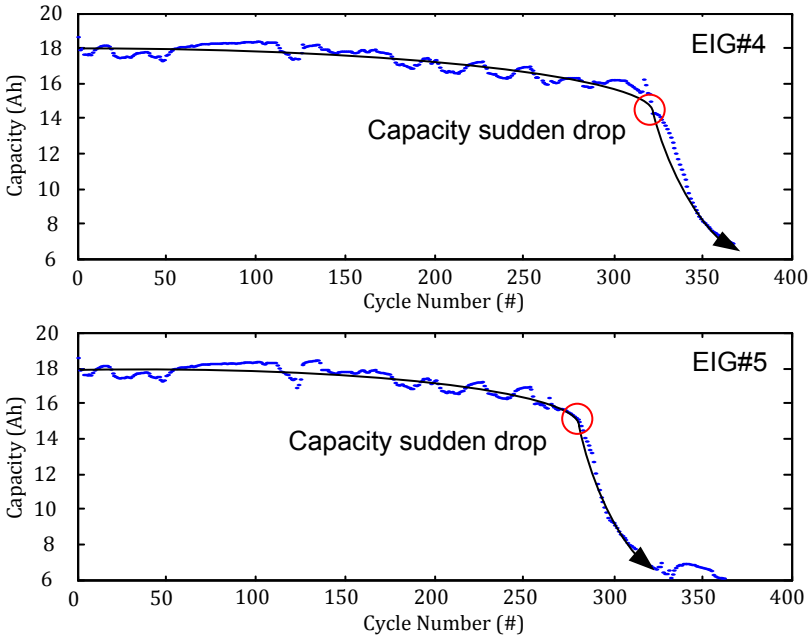

Figure 4.12 Capacity vs. cycle of cell EIG#4, #5, 2C charge and 2C discharge.

After all EIG battery aging tests are finished, it is found that the surfaces of batteries become wrinkle and the thickness increase significantly. Fig. 4.13 shows the photo of a fresh EIG battery cell and the EIG #3 after 1300 cycles. In the right side of Fig. 4.13, the measured thickness 9.44 mm of EIG #3 is about 30% higher than the fresh EIG battery. Thickness measurement results of all EIG cells are given in the Table. 4.3.

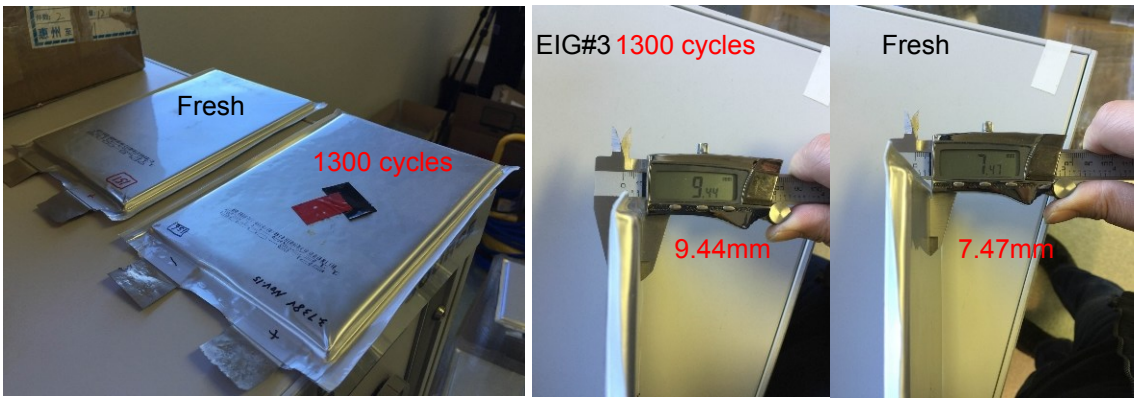

Figure 4.13 Thickness measurement of fresh EIG battery and after 1300 cycles

Table 4.3 Thickness measurement of all EIG cells

EIG #	Aging test	Thickness (mm)	
Fresh	N/A	7.2±0.2	100%
1	1300 cycles of 2C discharge/1C CC charge	7.72	107%
2	1300 cycles of 2C discharge/1C CC charge	7.67	106%
3	1300 cycles of 1C discharge/1C CCCV charge	9.44	131%
4	370 cycles of 2C discharge/2C CC charge	9.35	130%
5	330 cycles of 2C discharge/2C CC charge	8.74	121%

Other than NCM battery, the aging tests are conducted in other two LFP batteries, including one Valance 18650 cell and two A&S pouch cells (A&S #1 and #2). Due to the maximum current limitation, only standard aging tests are conducted. Fig 4.14 plots the capacity cycle curves of the aging tests. It is noticed that the capacities of all LFP batteries steadily decline from the beginning of the tests. The capacity drop is observed at

850 cycles in A&S cell #2. The degradation rate is lower than NCM battery in Fig. 4.10 and Fig. 4.12.

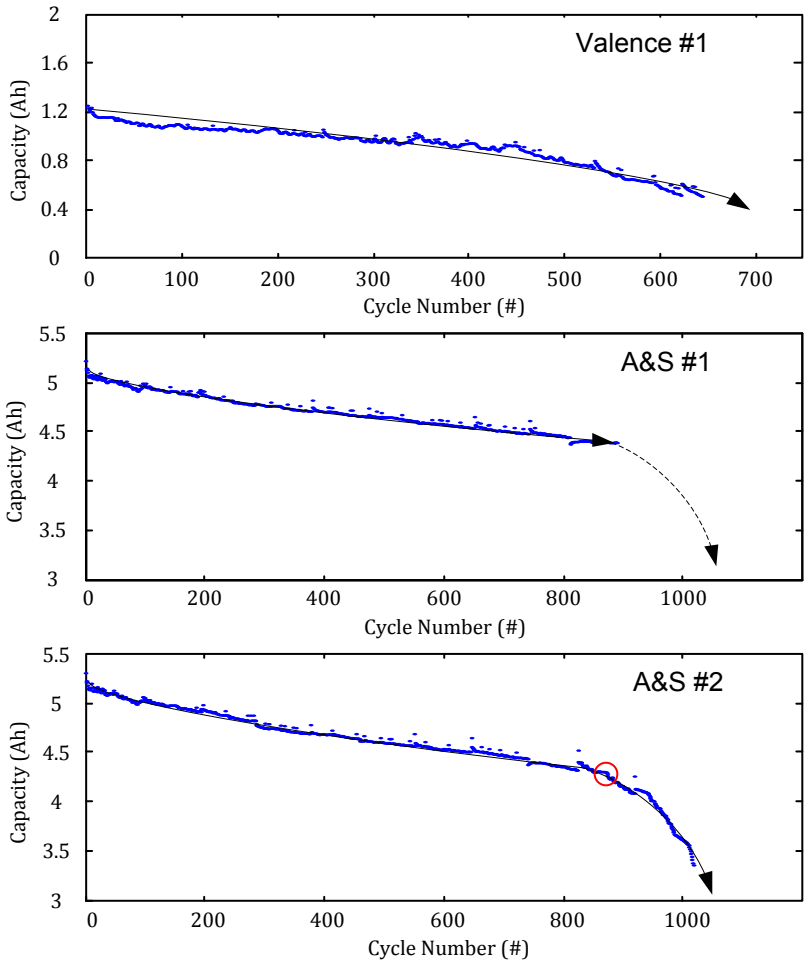

Figure 4.14 Capacity vs. cycle of Valence#1, A&S#1 and #2, at 1C charge/discharge.

The approximate A&S#2 OCV-SoC curves at different cycle are shown in Fig. 4.16. These curves reflect a interesting phenomenon, which is the capacity loss is not uniform over the entire range of SoC.

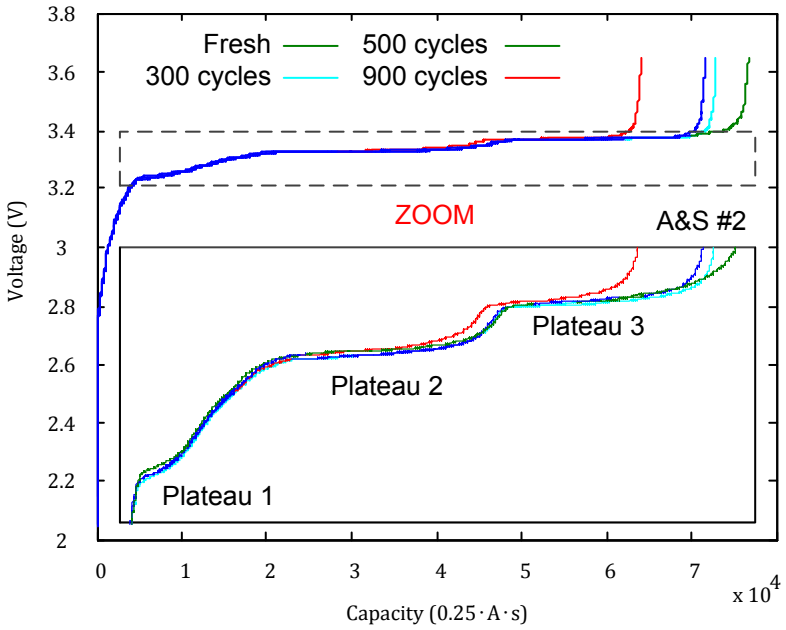

Figure 4.15 Voltage plateaus at different cycles (A&S #2)

For the LFP battery, there are three voltage plateaus in the OCV-SoC curves. These voltage plateaus are related to the characteristic of layer-structure graphite negative electrode. Researches [24-25] show that the voltage plateaus are corresponding to states of material microstructure. These states are essentially determined by the lowest material energy state. In different plateaus, the numbers of graphite layers that Lithium ions go through in intercalation/de-intercalation are different. The voltage plateaus and graphite associated reaction is shown in Fig. 4.16 and Table 4.4.

Table 4.4 Graphite intercalation reactions

Plateau #	Chemical reactions
I	$LiC_{12}+Li \leftrightarrow 2LiC_6$
II	$2LiC_{18}+Li \leftrightarrow 3LiC_{12}$
III	$2LiC_{27}+Li \leftrightarrow 3LiC_{18}$
IV	$LiC_{72}+Li \leftrightarrow 2LiC_{36}$
Overall	$Li+C_6 \leftrightarrow LiC_6$

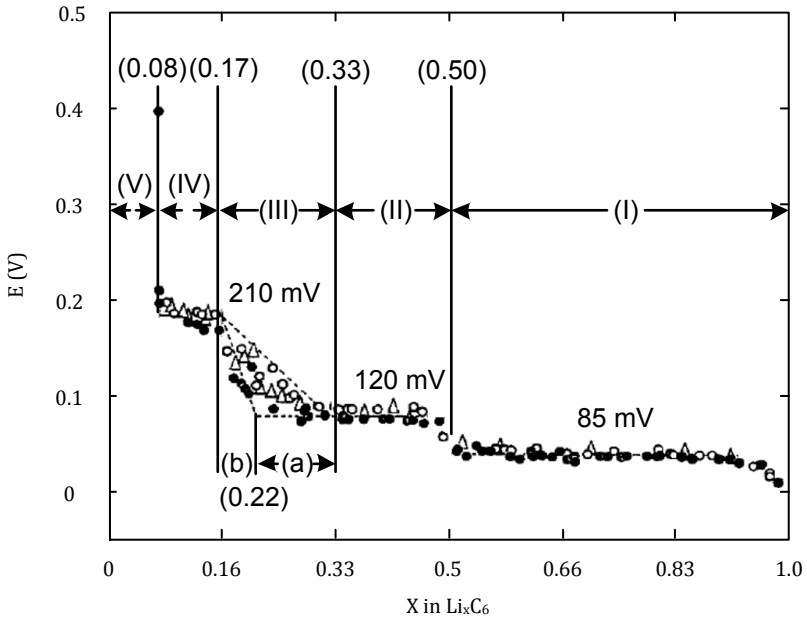

Figure 4.16 Voltage plateaus in graphite electrode

Three voltage plateaus shown in the zoom area of Fig. 4.15 are changed in the aging tests. Plateaus # 1 and #2 remain the same at the fresh (100% of nominal capacity), 300 cycles (95% of nominal capacity) and 500 cycles (92% of nominal capacity). It indicates

that the most of first 10% capacity loss happens at the plateau #1. Compare 500 cycles curve to 900 cycles (83% of nominal capacity) curve; it shows that the entire plateau #3 is shifted to the left side. It may claim that the capacity loss during this stage is mainly due to the shortened plateau #2. Differing from the conventional assumption of the uniform capacity loss over entire SoC range, the actual capacity loss is only related to certain SoC ranges, as demonstrated in Fig 4. 17. The OCV-SoC curve must be updated accordingly to build battery models considering the aging uncertainty. The shift of plateaus also causes some other problems. For example, Fig. 4.18 shows the entire polarization resistance-SoC curves of A&S#2 are shifted after the aging tests.

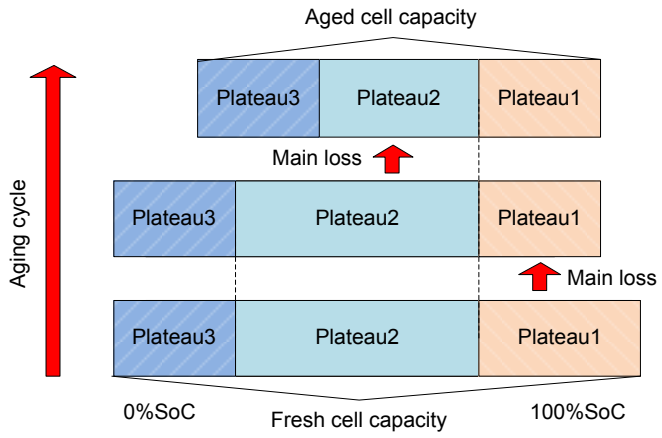

Figure 4.17 Capacity losses at different aging stages

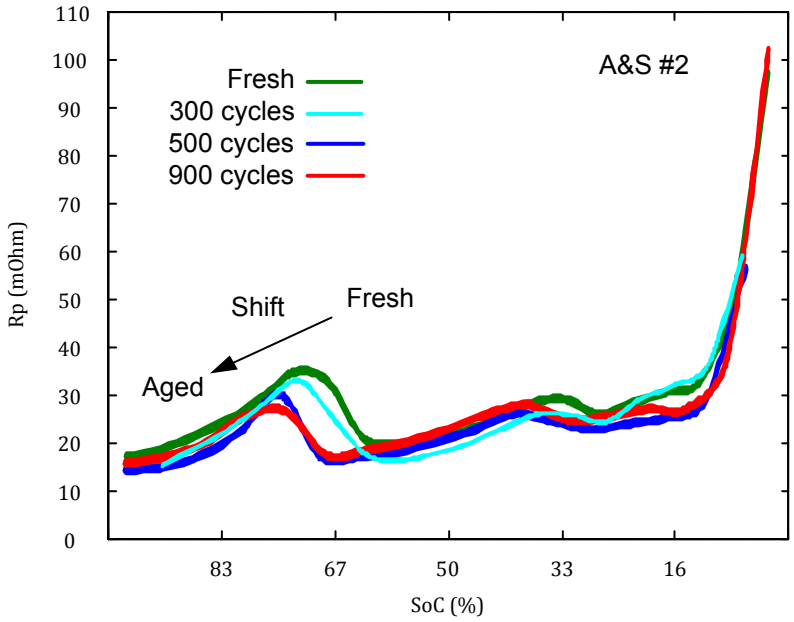

Figure 4.18 Polarization resistance vs. SoC at different cycles

All Electrovaya NCM battery cells are disassembled from a used electric pickup truck, and all AESC battery cells are disassembled from a Nissan LEAF EV, as shown in Fig. 4.19. Therefore, the usage histories of these battery cells are unknown. An Electrovaya battery cell with 29.5Ah capacity is selected to conduct the standard aging test. Two AESC battery cells (AESC#1 and #2) are selected to carry out the standard aging test and high power aging test.

Figure 4.19 Electrovaya battery and AESC battery packs

Test results in Fig. 4.21 and Fig. 4.22 show that the capacities of Electrovaya #1 and AESC #2 decrease to the 80% of their initial capacity within 150 and 200 cycles. The high power aging test result (AESC #1) shows that the capacity drops quickly after 100 cycles.

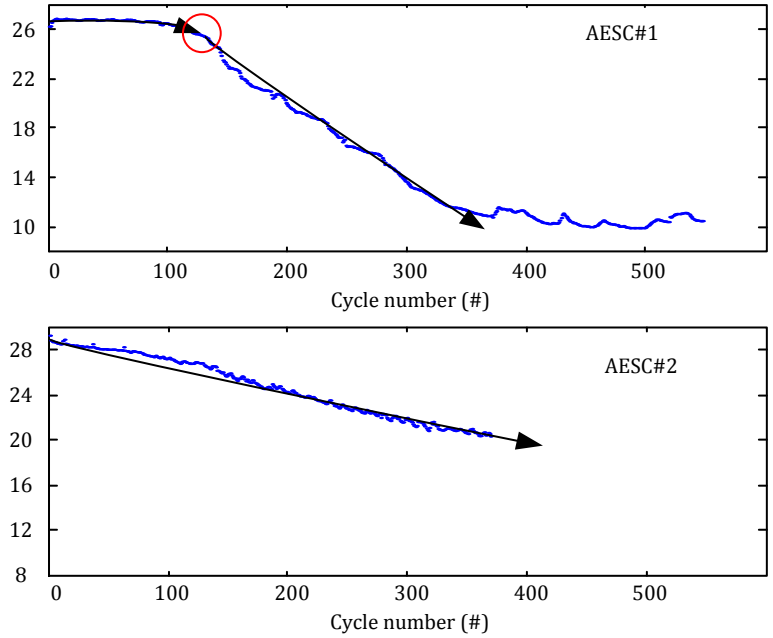

Figure 4.20 Capacity vs. cycle of AESC#1 and #2

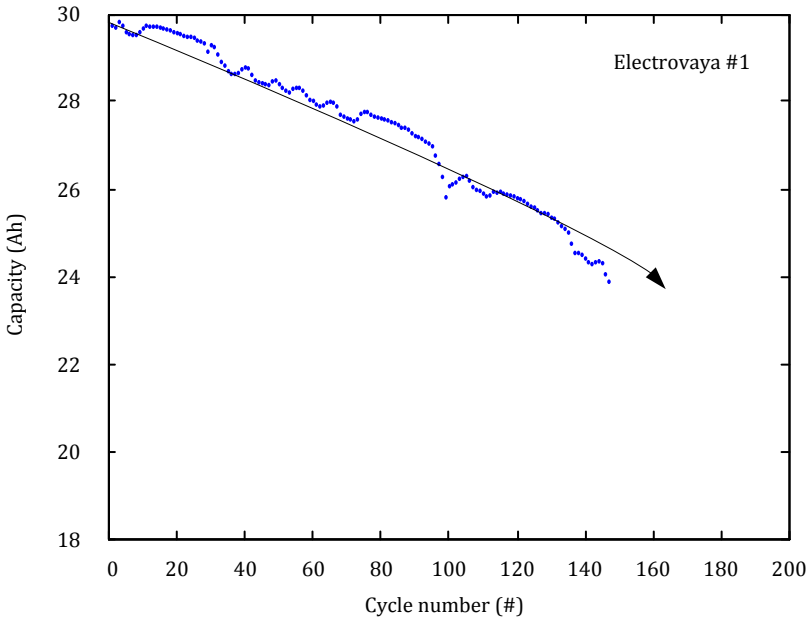

Figure 4.21 Capacity vs. cycle of Electrovaya#1

4.4 State-Of-Health Estimation via Incremental Capacity Analysis

In the previous chapter, we have discussed the Li-ion battery aging and modeling considerations. To utilize these modeling techniques in practice, one must be able to tell the SoH of Li-ion battery. SoH is used to describe the health level of Li-ion battery and is mainly presented in the degradation level of capacity and power. Capacity loss lowers the available mileage of EVs, and power degradation reduces the acceleration and regenerative brake abilities. Instead of using a single indicator such as the capacity, the SoH should be evaluated comprehensively. Direct capacity measurement, impedance measurement (EIS), battery model parameters identification, and incremental capacity analysis are major SoH estimation methods for Li-ion batteries.

Direct capacity measurement is to fully discharge/charge the battery and obtain its capacity. Typically, this method is used in electronics devices such as Laptop computers for battery calibration. However, it is impractical for EV applications due to the high capacity/power of the battery pack used in EVs. As introduced in Chapter 3, the EIS measurement use dedicated hardware (the electrochemical workstation) to investigate the frequency response characteristics related to SoH. Therefore, it is only practical in the laboratory [26, 27]. Parameters identification is a promising method for EV applications. Parameters are identified through specific Li-ion battery models and the collected data such as current, voltage and temperature. So the change of the identified parameters is explicitly correlated to specific degradation mechanisms and the SoH.

As mentioned in Chapter 4.4, the battery internal resistance are correlated with the cycle in the aging tests. Total 50 Electrovaya cells are disassembled from a used battery pack to build the correlation function of internal resistance and SoH. Capacities and internal resistance of all cells are plotted in Fig. 4.22. It clearly shows that, in general, cells with higher capacity have lower internal resistance. The internal resistance increment at low SoC is also higher when the battery is more aged. The average internal resistance value of each cell from 100% SoC to 0% SoC is calculated and plotted on the horizontal axis of Fig. 4.23, while the capacity of each cell is plotted on the vertical axis. We can draw the conclusion from the Fig. 4.23 that the internal resistance is in linear with capacities and can be used to determine the SoH. However, to obtain the averaged internal resistance in practical is a challenge. Another problem is that the internal resistance is highly temperature dependent, as discussed in Chapter3.

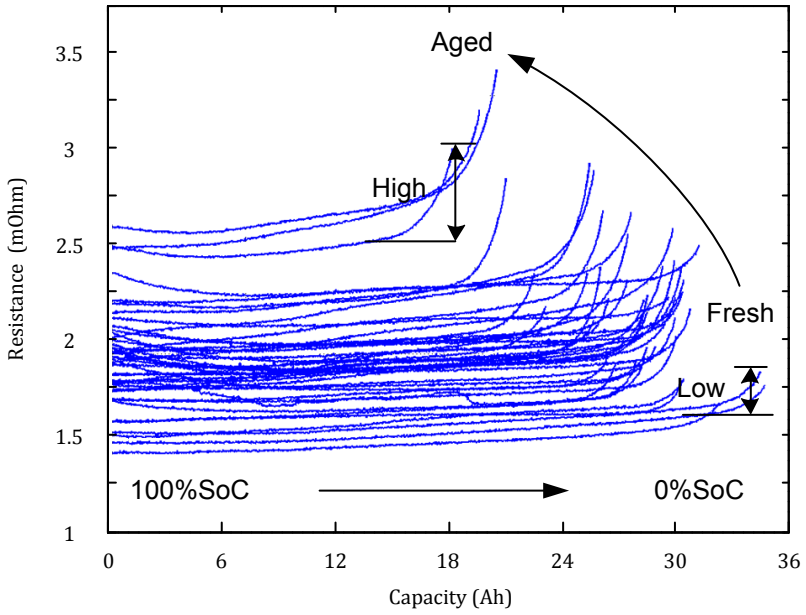

Figure 4.22 Internal resistance vs. capacities of all 50 Electrovaya cells

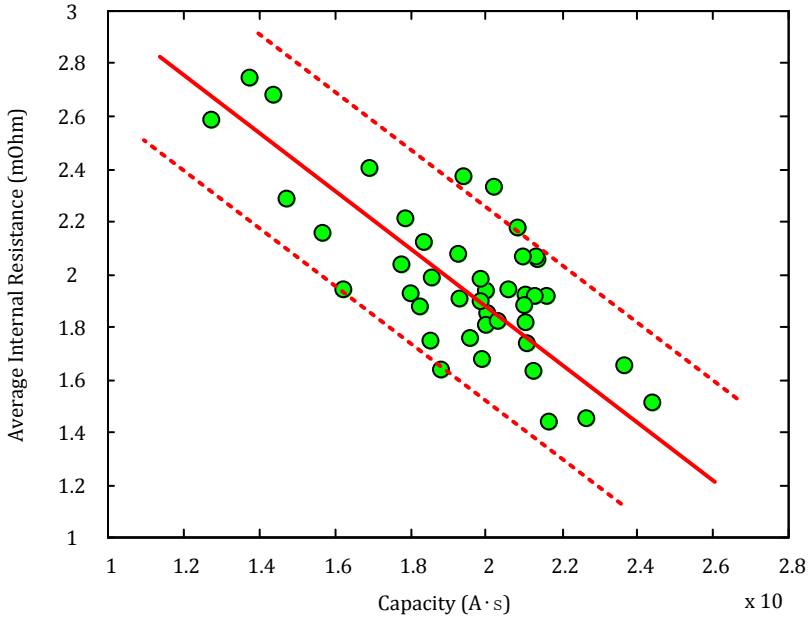

Figure 4.23 Average internal resistance vs. capacity of all 50 Electrovaya cells

Demonstrated in Fig. 4.15, the OCV-SoC curve is another characteristic that is related to the SoH. The changes in OCV-SoC curve often reflect the battery degradation [31]. Therefore, it may use the incremental capacity analysis (ICA), also called differential capacity analysis, to study the origin of degradation and estimate the SoH [32]. This method highlights the phase transitions of the battery voltage in charging or discharging. Therefore, we can use the current and voltage data during the battery charging to conduct the ICA. Therefore, the ICA based SoH estimation is a promising method for practical use. The differential capacity dQ/dV curve is obtained by differentiating the capacity versus voltage. It is defined in the discrete equation below:

$$\frac{dQ}{dV} = \frac{|Q_n - Q_{n-1}|}{V_n - V_{n-1}}, n = 2, \ldots, \text{length of data} \tag{4.1}$$

where Q_n, V_n are capacity and voltage measurement at a certain sampling point n. Ideally, the voltage data should be the approximately OCV, which can be obtained through low current charging/discharging tests or measuring the voltage after a long relaxation period.

Although ICA is an effective tool for SoH estimation, to calculate the $\mathrm{d}Q/\mathrm{d}V$ directly from raw data is difficult. That is because the measurement noise and quantization noise are unavoidable due to the limited bits and limited bandwidth in ADC. Therefore, a series of signal processing is needed before the ICA. First of all, it should notice that the sampling period of DAQ system, i.e. the Arbin BT 2000, is not uniform. For example, set the sampling period to be 0.5s, the actual sampling periods varies from 0.51s to 0.58s

randomly, as shown in Fig. 4.24. It is critical to use the correct sampling period in ICA test, especially in the flat voltage plateau region.

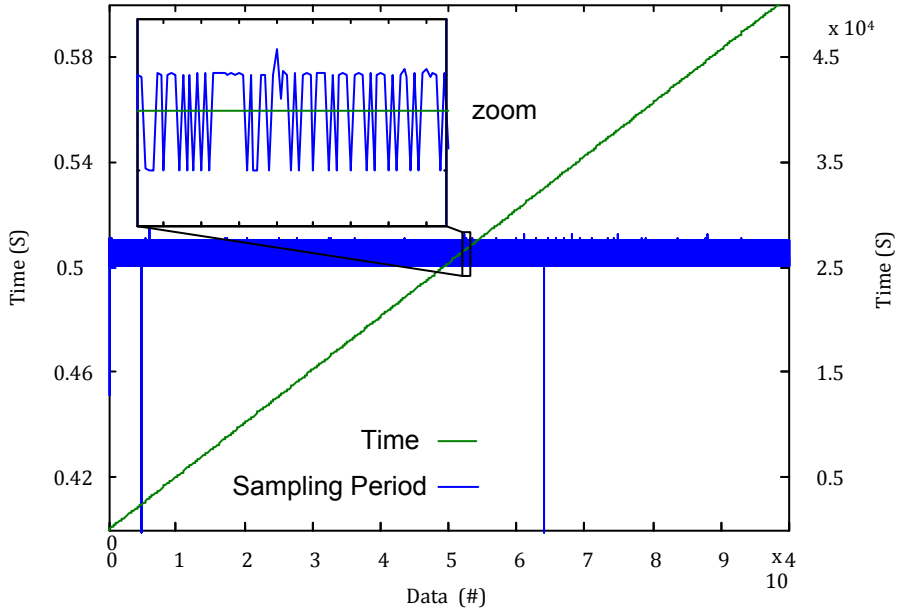

Figure 4.24 Sampling problem of Arbin BT 2000

The second challenge is the quantization noise. Although the Arbin BT2000 use a 16 bits ADC to collect data; the resolution is not high enough when the dv/dt rate is very small at plateau region. Fig 4.25 plots the zoomed voltage with 2 Hz sampling rate. The minimum voltage resolution is around 0.3 mV. If we calculate dQ/dV curve directly from the raw data by using diff function in the MATLAB, the result is entirely distorted due to quantization noise, as shown in Fig. 4.26 top part. Setting the differentiation interval from 0.5s to 500 s, the calculated dQ/dV curve is better, as shown in Fig. 4.26 bottom part. However, the resolution is still not insufficient to present the ICA peaks clearly.

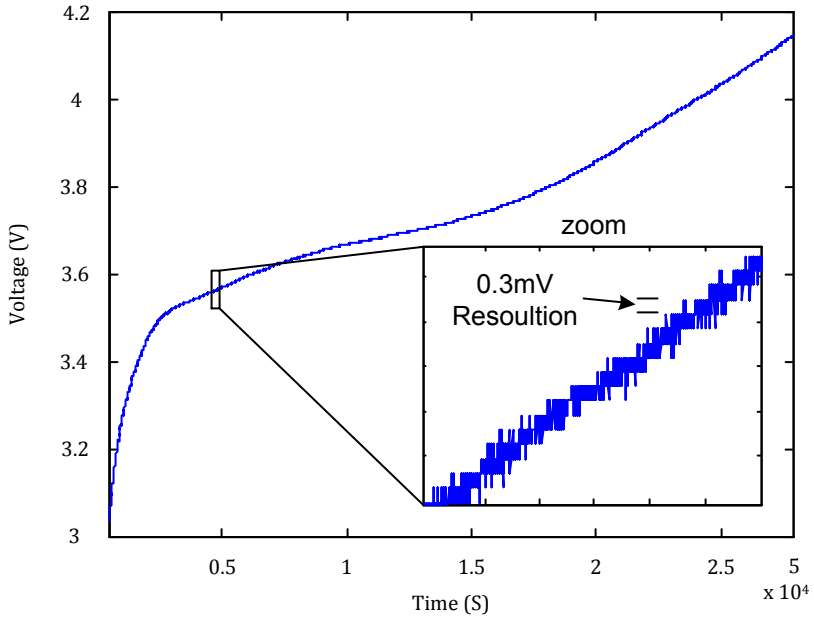

Figure 4.25 Raw voltage data when battery is in charging.

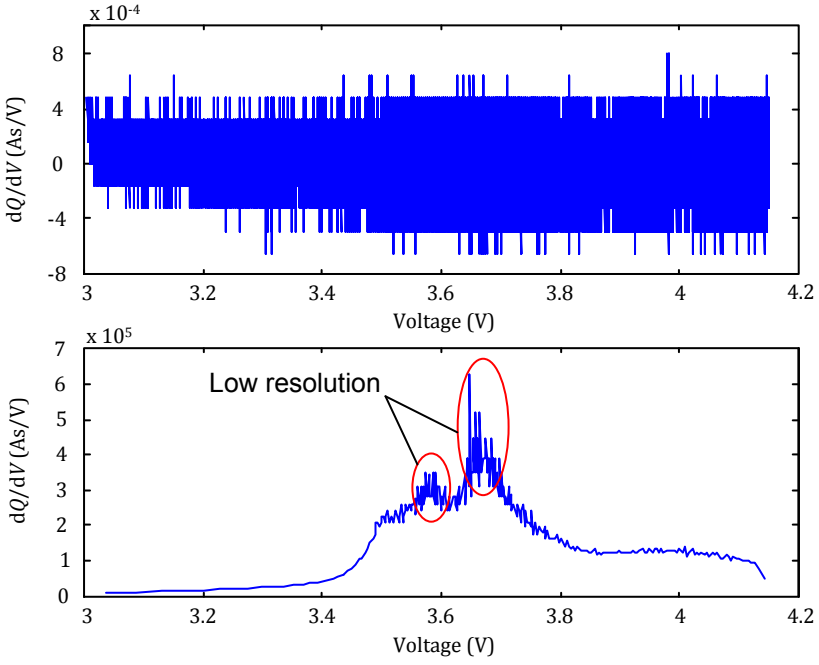

Figure 4.26 dQ/dV curves by using diff function (up) and modified diff function (bottom)

A series of filtering and fitting process is needed to obtain the clear dQ/dV curves for SoH estimation. As known, smooth data can be obtained by increasing the order of the filter. However, the high order filters also cause the over-fitting problem and attenuate the true data. Therefore, the desired filtering method for ICA should be able to adjust its order and filter coefficients automatically. In this study, an adaptive filtering algorithm is developed to process raw data and calculate the dQ/dV. The flow chart of this algorithm is shown in Fig. 4.27.

First, the entire raw data is processed by a two degree Savitzky–Golay filter with a span of 1/10 data length for the smoothing purpose. By doing this, most of the quantization noise is removed at low voltage variation ΔV region. However, the over-fitting problem occurs at high voltage variation ΔV region. Then it needs to subtract processed data from raw data to obtain the removed noise. Known the minimum voltage resolution of Arbin BT 2000 is 0.3 mV, any removed noise higher than 0.6mV should be considered as the over-fitting. The over-fitting usually occurs at the beginning or ending of charge/discharge where voltage variation ΔV rate is high. By comparing with the 0.6mV threshold, the over-fitted data can be found. Repeat these filtering processes to the over-fitted data with lower orders until the removed noise is lower than the threshold. Finally, it can reorganize the data for the final dQ/dV calculation.

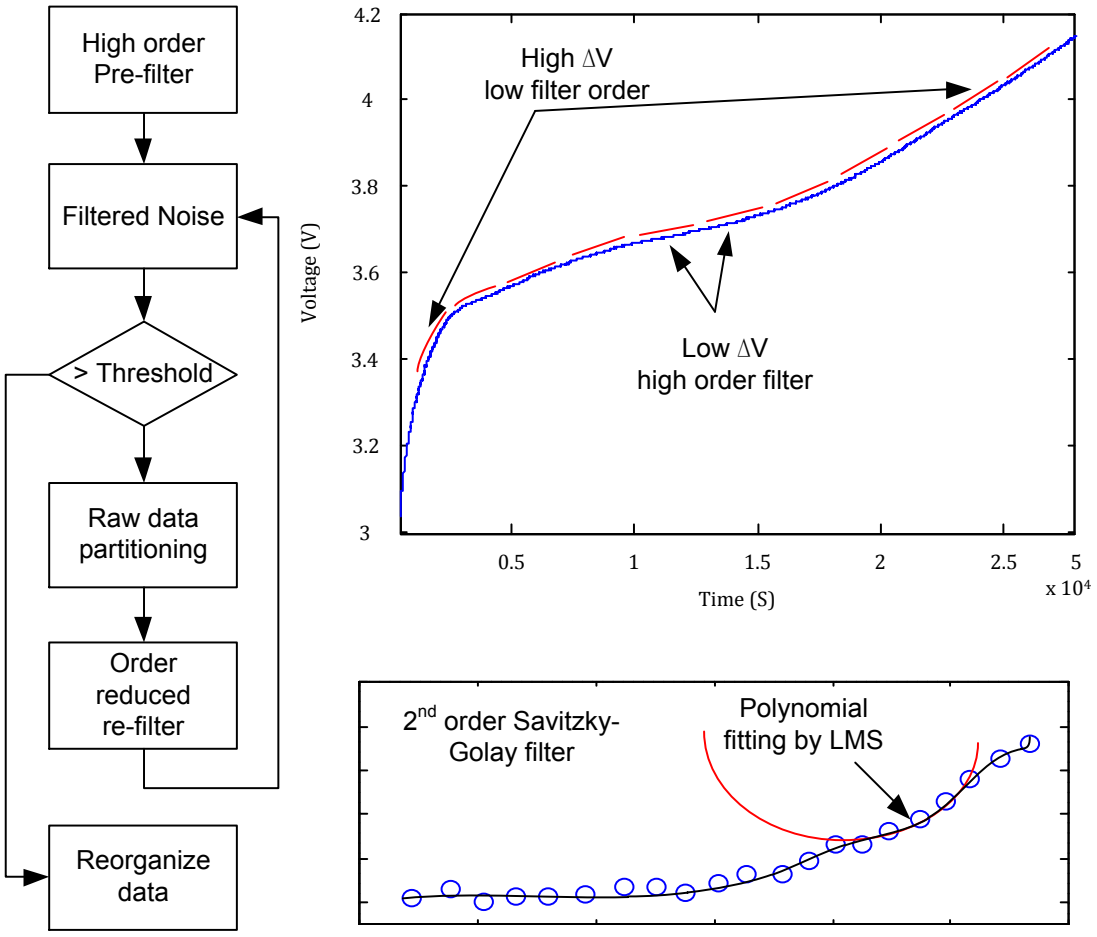

Figure 4.27 Adaptive filtering process for ICA

In conventional ICA in the electrochemical study, the charging current is set to be very low (1/20C) to eliminate the polarization effect. However, for EV applications, the battery charging time is usually less than 8 hours when using an onboard AC charger, or less than 2 hours when using a DC charging station. In this study, the charging current in the ICA tests is set to be 0.3C~2C. The comparison of 1/20C and 1/2C ICA tests (A&S #2)

are plotted in Fig.4.28 and Fig. 4.29. The dQ/dV curves obtained from 1/20C current charging has very high IC peaks #2 at 3.33V due to the flat plateau. The flat plateaus not only create difficulty in the smoothing process but also eliminate the internal resistance difference. As shown in Fig. 4.28 up part, the horizontal difference in ICA peak #3 of all dQ/dV curves is too small to identify, and the IC peak 2# is not smoothed at all. The dQ/dV curves obtained from 1/2C current charging show that both IC peak #1 and #3 have good correlations with cycles, which is more suitable for SoH estimation.

Other than LFP batteries, voltage plateaus of NCM and LMO batteries are much less flat, as plotted in Fig. 4.30 and Fig. 4.31. Both IC peak #1 and #2 in EIG NCM battery show the possibility for SoH estimation. Notice that when EIG#3 is considered to as a failed battery after 1300 cycles, the corresponding dQ/dV curve become extremely flat and all IC peaks disappeared. For AESC LMO battery, three of total four IC peaks in the dQ/dV curves (#1, #3 and #4) are capable of SoH estimation. The correlation between IC peak #2 and the SoH is not clear. The peak #2 also disappears at low temperatures, as discussed in Chapter 3.3.

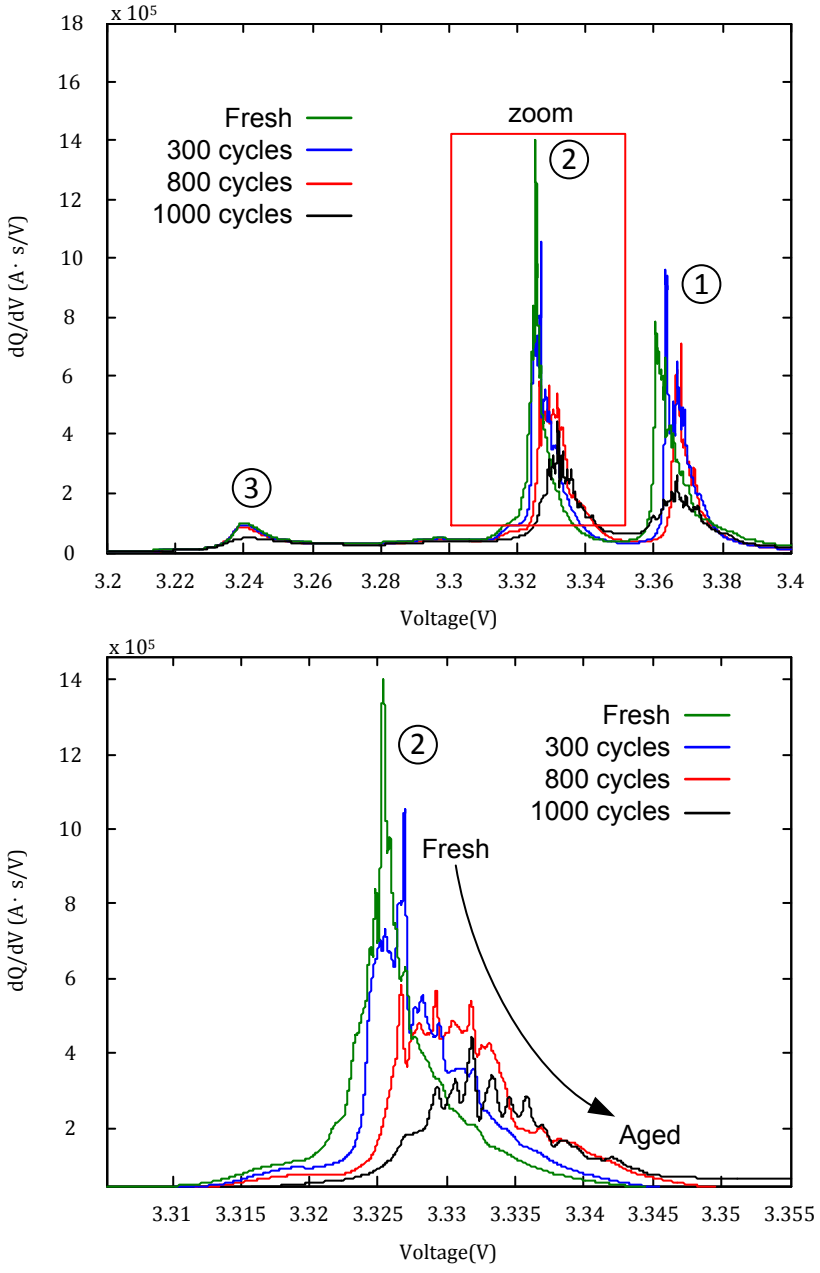

Figure 4.28 d*Q*/d*V* curves of A&S#2 using 1/20 C current

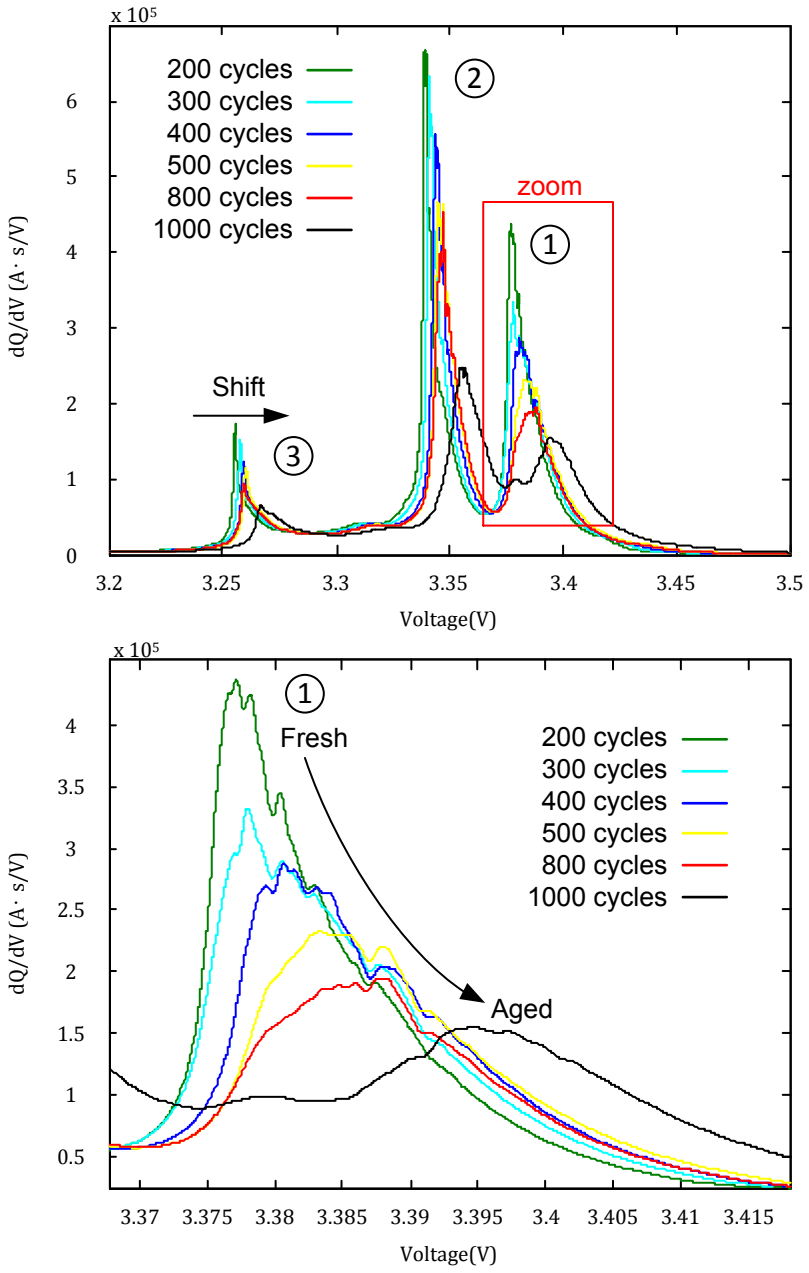

Figure 4.29 dQ/dV curves of A&S#2 using 1/4 C current

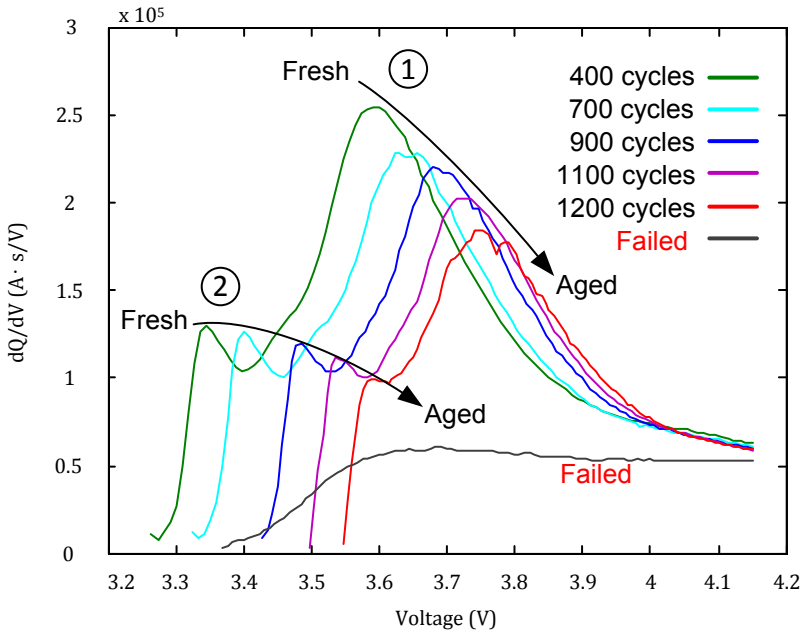

Figure 4.30 dQ/dV curves of EIG#2 using 1/2 C current

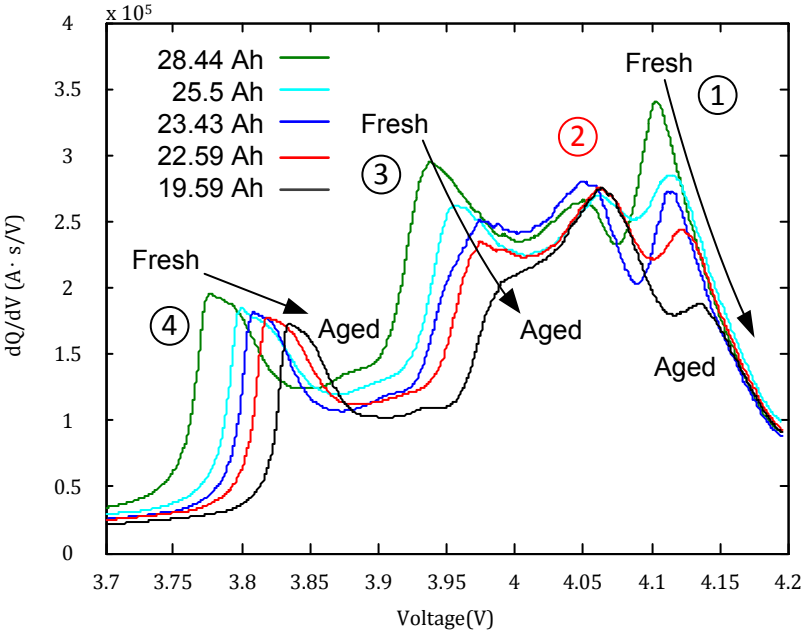

Figure 4.31 dQ/dV curves of AESC#2 using 1/3 C current

4.5 Bias Correction Modeling Method for Aged Li-ion battery

Based on the conclusion in previous sections, the inconsistency of Li-ion battery cells can be summarized as the difference of capacities, OCV~SoC, internal resistance, and polarization. Each cell model in the Li-ion battery pack can be built based on the reference model with bias functions, as demonstrated in Fig. 4.32. First, select a standard cell from the battery pack to build the reference battery model. Then apply the ICA based SoH estimation method to each cell and use the estimation result to build the bias correction function. Finally, the modified models can be obtained from each cell by combining the reference model and bias correction function.

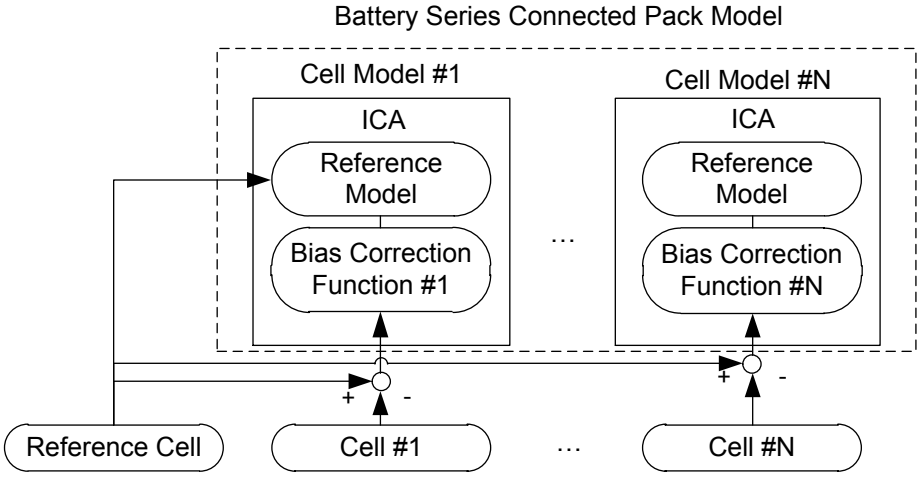

Figure 4.32 Overview of pack modeling based on bias correction and ICA method

Select the Electrovaya NCM battery as an example, the bias correction modeling procedure is given below. Three dQ/dV curves from a standard reference cell and two target cells are obtained from 0.5C constant current charging, as shown in Fig. 4.33. Two

IC peaks #1 and #2 locating at the voltage range from 3.5V to 3.8V denote the two plateaus on the charging voltage curves.

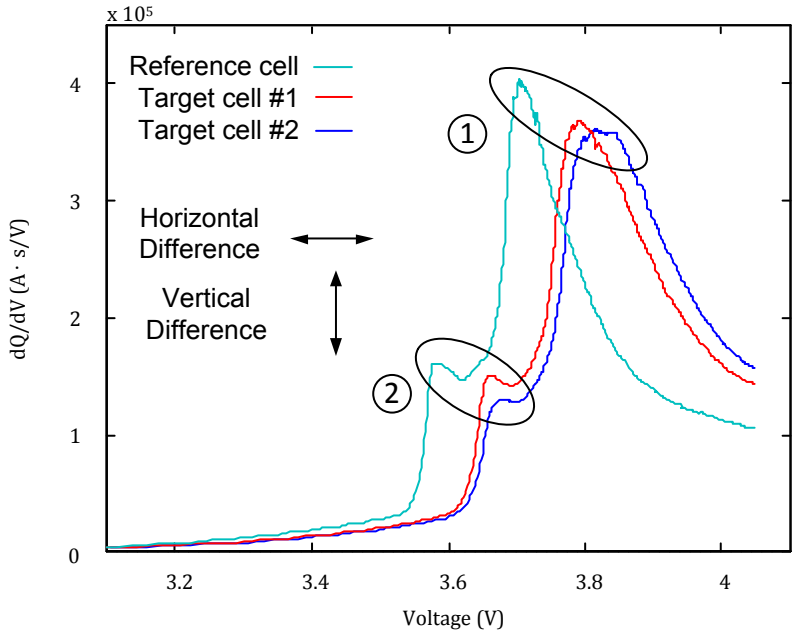

Figure 4.33 dQ/dV curves of reference cell and two aged target cells

Plateau happen at the same OCV range with the same electrode material, the horizontal differences in IC peak #2 can be used to represent the resistance inconsistency. Set the identification results from the HPPC test as the reference, the goodness of estimation results based on the ICA method is up to 87%. Both vertical and horizontal difference of IC peaks #1 and #2 are used jointly to build the capacity and OCV bias functions. Based on the ICA tests results, the improved model with bias correction functions $f_n(ICA_n,ICA_0)$ can be written as:

$$\begin{cases} R_o'(SoC) = R_o(SoC) + f_{R_o}(ICA_n, ICA_0, SoC) \\ R_P'(SoC) = R_P(SoC) + f_{R_P}(ICA_n, ICA_0, SoC) \\ C_P'(SoC) = C_P(SoC) + f_{C_P}(ICA_n, ICA_0, SoC) \\ OCV'(SoC) = OCV(SoC) + f_{OCV}(ICA_n, ICA_0, SoC) \end{cases} \tag{4.2}$$

where ICA_0 and ICA_n denote the ICA peaks of reference battery and target battery respectively; R_O, R_P, C_P and R_O', R_P', C_P' denote the model parameters of the reference battery and target battery. These bias correction functions $f(ICA_n, ICA_0, SoC)$ as follow:

$$\begin{cases} f_{R_O} = a_1\left(V_{ICA_n} - V_{ICA_0}\right)^2 + a_2\left(V_{ICA_n} - V_{ICA_0}\right) \cdot f(SoC) \\ V \in \left(\frac{dQ}{dV} > \frac{dQ}{dV_{max}}\right) \\ f(SoC) = a_3 + a_4 \cdot SoC - a_5 \cdot SoC^2 \end{cases} \tag{4.3}$$

$$\begin{cases} f_{R_P} = \frac{1}{n}\sum_{i=1}^{n}(V_{ICA_n} - V_{ICA_0}) \cdot b_1 \\ 3.71 < V < 3.96 \end{cases} \tag{4.4}$$

$$\begin{cases} f_{ocv} = c_1\left(V_{ICA_n} - V_{ICA_0}\right)^2 + c_2\left(V_{ICA_n} - V_{ICA_0}\right) \cdot f(SoC) \\ V \in \left(\frac{d^2Q}{dV^2} < c_3\right) \\ f(SoC) = c_4 + c_5 \cdot SoC + c_6 \cdot SoC^2 \end{cases} \tag{4.5}$$

where V_0 denotes ICA peak #2 voltage in the reference model, V_n denotes ICA test peak #2 voltage in the target model. As shown in functions f_{Ro}, f_{RP}, f_{OCV}, the Ohmic resistance difference is represented by a quadratic polynomial of lateral voltage shifting of ICA peak #2, where $\mathrm{d}Q/\mathrm{d}V$ reaches the maximum value. Capacity and OCV difference are also represented by a quadratic polynomial of the position difference of both IC peak#1 and peak#2 in the $\mathrm{d}Q/\mathrm{d}V$ curves. For relaxation processes difference, a simple empirical function drawn from the average voltage difference at IC peak #1from 3.7V to 3.96V is applied.

Table 4.5 Parameters in bias correction functions

Parameters	Value	Parameters	Value	Parameters	Value
a_1	23	b_1	0.27	c_1	0.03
a_2	1.7			c_2	0.95
a_3	0.507			c_3	127
a_4	0.0107			c_4	0.418
a_5	$5.87 \cdot 10^{-4}$			c_5	0.0353
				c_6	0.00383

An example of internal resistance modeling based on the bias correction method is shown in Fig. 4.34. In this example, the horizontal voltage difference of the main IC peaks #1 between the target cell and reference cell is 188 mV (3.889V - 3.701V). The calculation of corresponding bias function at 50% SoC and bias corrected/measured Ohmic resistances are given below and in Table 4.6.

The Federal Urban Driving Schedule (FUDS) is applied to all 50 cells to collect voltage and current data to evaluate the performance of bias correction method. The cell with the highest capacity is selected as the benchmark to build the reference model. Compared with the voltage prediction results from the HPPC based one order RC battery model, the voltage prediction result of bias correction method remains good. The average voltage errors of all 50 Li-ion battery cells are within 12 mV. The voltage prediction results by using both the bias correction method and the HPPC modeling method are displayed in Fig. 4.35.

$$\begin{cases} f_{R_O}(0.5) = 23 \cdot (3.889 - 3.701)^2 + 1.7 \cdot 10^{-1} \cdot (3.889 - 3.701) \cdot f(0.5) \\ V \in \left(\frac{dQ}{dV} > \frac{dQ}{dV_{max}}\right) \\ f(0.5) = 0.507 + 0.0107 \cdot 0.5 - 5.87 \cdot 10^{-4} \cdot 0.5^2 = 0.512 \end{cases} \quad (4.6)$$

$$f_{R_O}(0.5) = 23 \cdot 0.188^2 + 1.7 \cdot 10^{-1} \cdot 0.512 = 0.82927\ mOhm$$

Table 4.6 Corrected Ohmic resistance and measured value

SoC (%)	Corrected resistance (mOhm)	Measured resistance (mOhm)	Error (%)
100	3.35	3.27	2.39
50	3.4	3.39	0.5
10	3.78	3.81	0.79

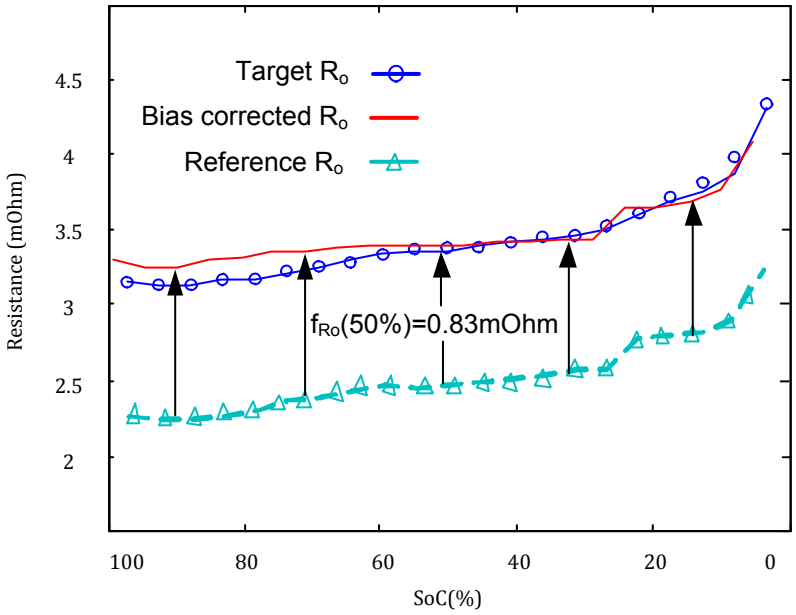

Figure 4.34 Example of Ohmic resistance correction. Measured resistance and bias corrected resistance calculated based on reference model.

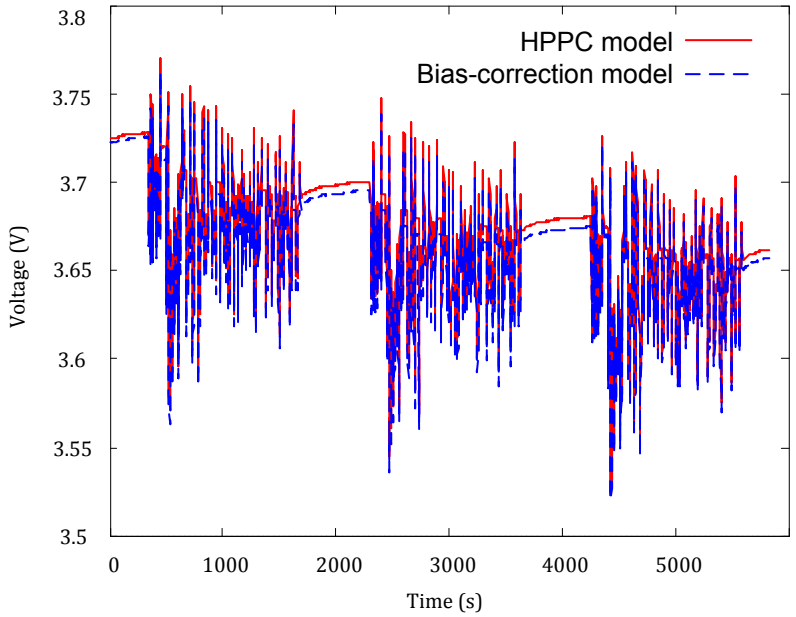

Figure 4.35 Voltage predictions in the FUDS tests.

The pack model is the combination of 50 bias corrected individual cell models together. The voltage prediction error comparison of the proposed method and the uncorrected single cell method shows that the error of the proposed modeling method is much lower, as illustrated in Fig. 4. 36. It is noted that the prediction error of each cell is less than 45mV, which is close to the standard HPPC method. However, the model error increases when SoC reaches 85% and higher. The dQ/dV peak # 3 in the high voltage range (3.8~4.05V) is distorted at the 0.5C high charging current. It is expected to improve the accuracy by adding the SoC as a state variable in functions f_2/f_3, and to consider the correlation between the temperature, aging, polarization effect and IC peaks.

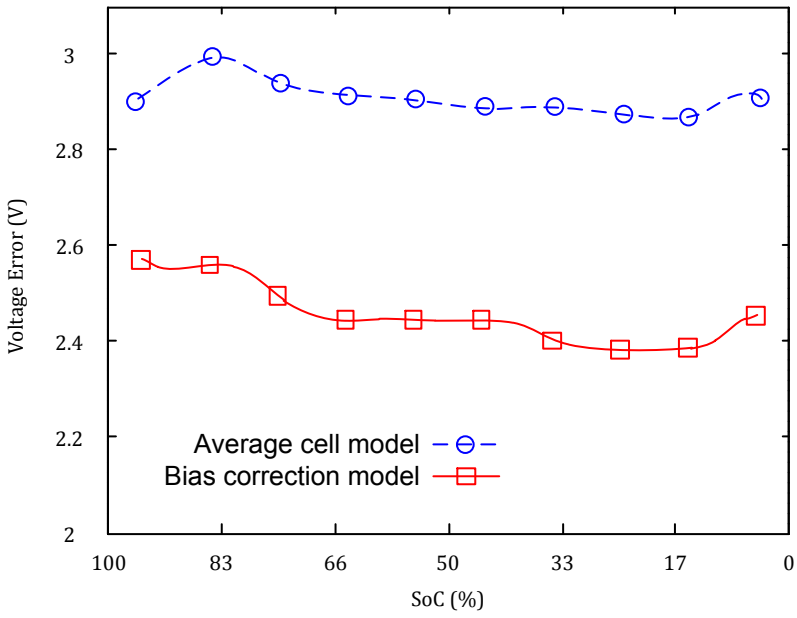

Figure 4.36 Voltage prediction error in average cell model and bias correction model.

4.6 Summary

In this chapter, Li-ion battery aging mechanism is studied first. It shows that the aging is caused by both physical and chemical process in the battery. Then, a series of aging tests are designed and carried out to understand the degradation path. It shows that the high charging current with deep DoD are the major aging factors. The incremental capacity analysis is applied to experimental data to estimate the SoH. It shows that the incremental capacity peaks in dQ/dV curve can track the SoH accurately. Finally, a bias correction modeling method using the SoH is proposed. It can model the entire aged battery pack by using the model of a reference cell and bias functions.

CHAPTER 5

Modeling of Battery Packs with Parallel-Connected Cells

The power and energy demands of PHEVs and EVs are usually higher than HEVs' due to their full electric driven powertrain. The peak power requirement of a typical four-seat passenger EV can be up to 80~150 kW [9], compare with the 50kW in similar HEV. Hundreds of Li-ion battery cells are connected in series and parallel [10] to compose the battery pack to satisfy the demands. For examples, the battery pack in a Nissan Leaf EV consists of 192 LMO cells with two cells in parallel [11]; a Chevrolet Volt PHEV's battery pack is composed of 288 NCM Li-ion battery cells with three cells in parallel [12].

For series connected Li-ion battery cells, it is feasible to monitor the voltage and current of each cell. However, there are tremendous difficulties to monitor the current in parallel connected cells. Ideally, the current of each cell can be obtained through divide the total current by the number of cells in parallel. However, in practice, the inconsistency problem of Li-ion battery cells may cause unbalanced current and further aging issue. This chapter focuses on the study of the characteristics of parallel-connected Li-ion battery. A series of experimental tests are designed and conducted to investigate the cell inconsistency problem together with influence on parallel connected Li-ion battery pack for EVs application. Based on the experimental results and analyses, unbalanced current

in the 2, 3 and 4 Li-ion battery cells in parallel are discussed and simulated through MATLAB/Simulink based battery pack model.

5.1 Cell Inconsistency Problem

The cell inconsistency problem limits the overall performance of Li-ion battery packs. Once multiple Li-ion battery cells are assembled into a battery pack, this pack cannot be regarded as the sum of individual cells. Based on the Cannikin Law (Wooden Bucket Theory), the poorest cell determines the battery pack performance, as shown in Fig. 5.1. Individual cells with the lowest and highest SoCs are used to determine the SoC of the entire battery pack. As discussed in Chapter 4, severe polarization effect more likely happens to aged cells, which generate more heat and then cause accelerated battery degradation [13]. As the increase of operating time, the inconsistency problem will become worse.

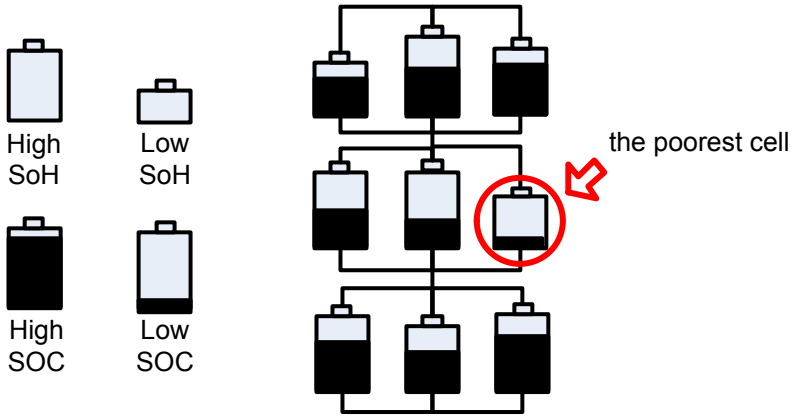

Figure 5.1 Inconsistency problem in battery pack

A variety of factors causes the cell inconsistency problem. During the battery manufacturing stage, technique faults, impurity of electrode materials, and human operation errors can result in the initial cell characteristics differences, such as the different initial capacities and internal resistance. Different operating conditions, such as various environmental temperatures and charging/discharging power rate, may cause further different degradation rates, and then make the inconsistency problem worse.

By improving the manufacturing technique and reinforcing the quality control, the initial cell characteristics differences can be reduced. The balancing circuit in the battery pack can inhibit the initial SoC variation and prolong the lifetime of the battery pack at some level. However, cell inconsistency problem in parallel connected Li-ion battery pack remains a significant challenge.

5.2 Parallel connected Li-ion Cells Experimental Setup and Design

Test Bench Setup and Noise Filtering

To investigate the cell inconsistency problem in parallel connected Li-ion battery packs, we build a test bench system capable of measuring the current of each cell, as shown in Fig. 5.2. The Arbin BT2000 battery test system conducts the charging/discharging tests to battery packs and records the voltage, total current, and temperature data. For each branch of parallel connected cells, the voltage and current data are measured and recorded by Hall Effect current transducers (LEM LC 300-S), precision

isolation amplifiers (Analog Device AD210) and dSPACE DS1104 R&D controller boards.

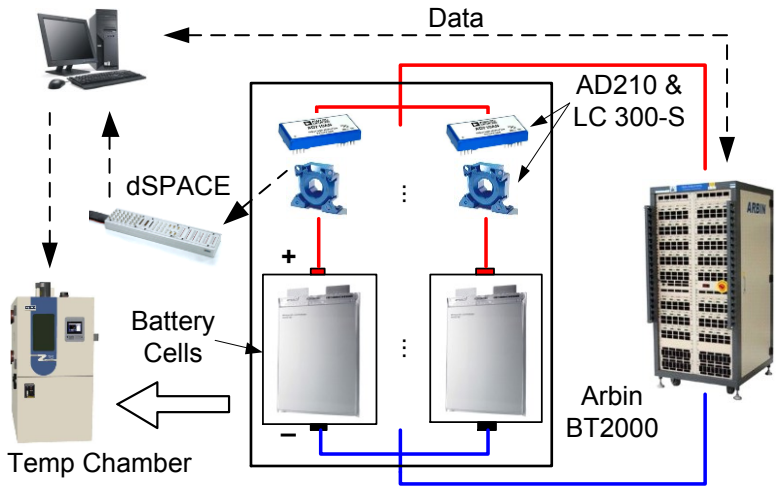

Figure 5.2 Schematic of parallel connected Li-ion cells experimental setup

Notice that the primary current measuring range of the LEM LC 300-S is 0~700A, which is greatly higher than the branch current (0~30A) in these experiments. Therefore, 5 turns multiple winding of connector wire are used to adapt the actual current range and increase the measurement accuracy. For voltage acquisition, although the Analog AD210 have wide bandwidth (20kHz @ -3 dB) and high CMR (120 dB), the recorded voltage data contain lots of noise, as shown in Fig. 5.3. These low-frequency noises are usually discrete and have much higher or lower magnitude than correct voltage data, while the right voltage data is continuous and current determines the variation rate (dV/dt) in the Li-ion battery.

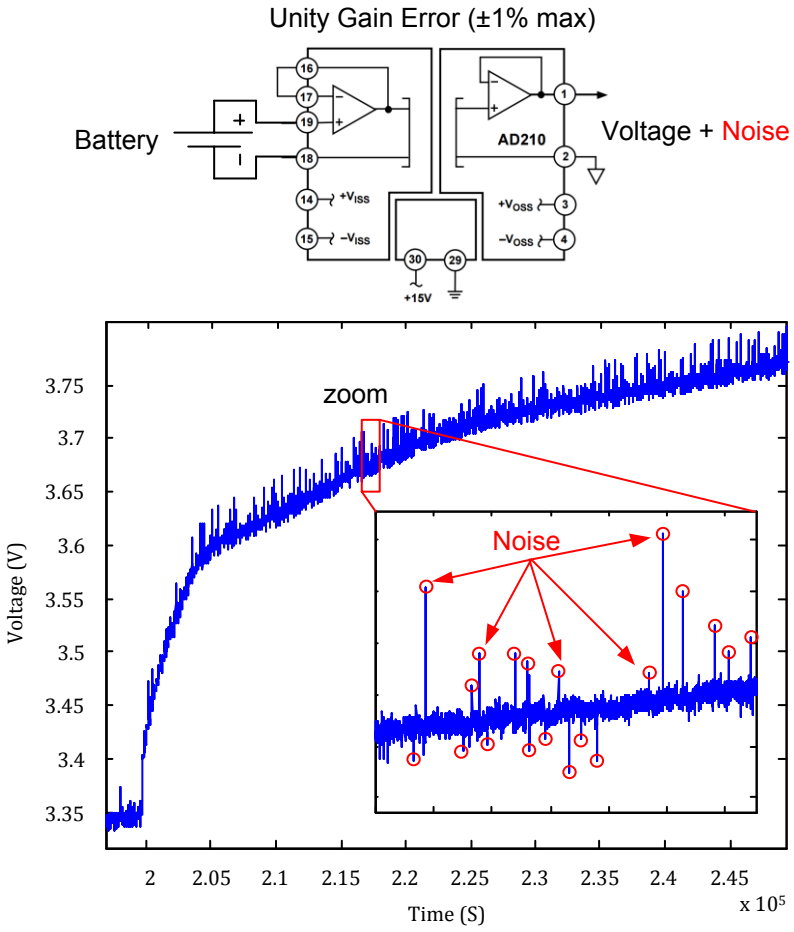

Figure 5.3 Recorded raw voltage data. Red circles indicate the low-frequency discrete measurement noise from AD210 isolation amplifier.

An adaptive filter algorithm capable of identifying these noises is designed to process the raw voltage data. In this algorithm, the t+2th value is compared with previous t+1th value and next t+3th value to obtain two voltage differences. If the both differences are greater than the threshold dV/dt rate, the t+2th value is considered as the corrupted data.

By comparing with multiple data points from both current and voltage, it avoids considering mistakenly the voltage step response caused by current as the noise data. Fig 5.4 shows the correct data is successfully restored from raw data by using the adaptive filter algorithm, and the magnitude of removed noise is within 50mV

Table 5.1 Adaptive Filter Algorithm Flow Chart

Algorithm Adaptive Filter to eliminate measurement noise

Require: *t, V(t), I(t), Length(V), dv/dt*$_{max}$

loop

while (*t<(Length(V)-2)*) **do**

if (||*V(t+2)-V(t+1)*||> *dv/dt*$_{max}$) **and** (||*V(t+3)-V(t+2)*||> *dv/dt*$_{max}$)

V(t+2)=0.25·(V(t+4)+V(t+3)+V(t+1)+V(t))

end if

t=t+1

end while

end loop

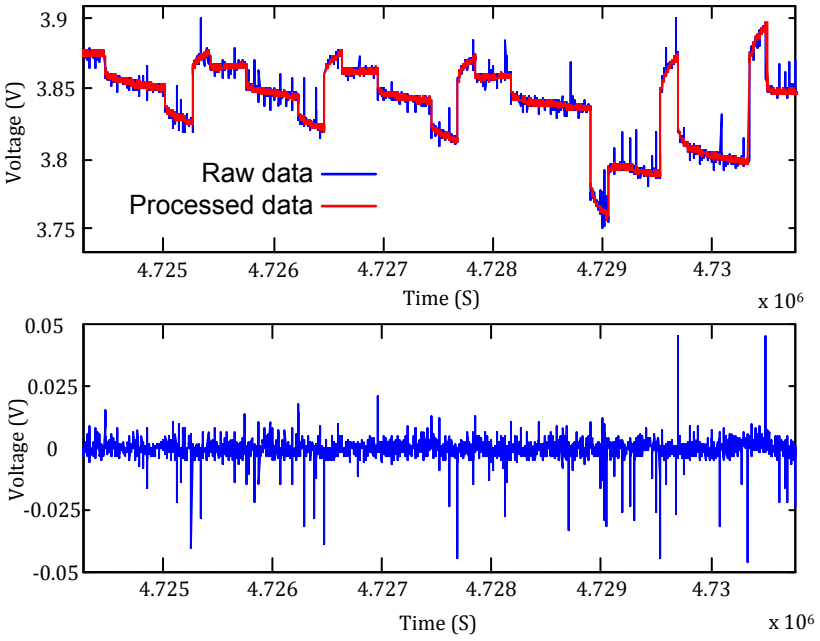

Figure 5.4 Comparison of raw data, processed data, and filtered noise

Experiment Design

A total number of 34 used NCM Li-ion battery cells with various degradation levels are selected for the experiment. These battery cells have been used in a prototype Chrysler electric pickup truck for more than four years. As show in Fig. 5.5, all cells are connected originally in series to compose the battery pack, which means the current in all battery cells are same. The nominal battery voltage is 3.7V with nominal capacity 32 Ah. The upper cut-off voltage is 4.05V; the lower cut-off voltage is 3.0 V.

Figure 5.5 Battery pack disassembled from the prototype pickup EV

First, each Li-ion battery cell is disassembled from the pack to measure the capacity through 3 cycles of fully CCCV charging/CC discharging at 0.5 C (16A) current at room temperature (25°C). Capacities of all 34 cells are in the range of 58% to 99% of the nominal capacity of the maximum 31.7 Ah and the minimum 18.7 Ah. Most cells remain 80% or higher capacity, as shown in Fig. 5.6.

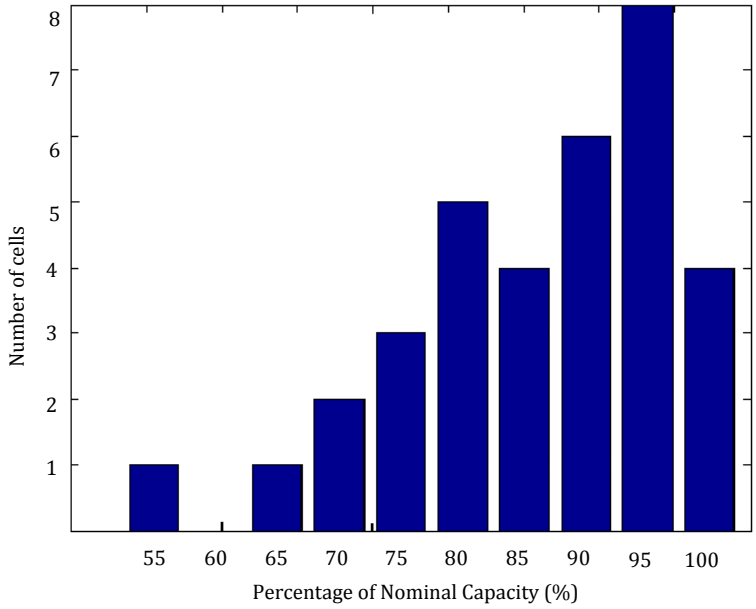

Figure 5.6 Cells capacity statistical distribution

All cells are assembled into 27 groups with two, three and four cells in parallel. A series of tests are carried out for model parameters identification and validation. These tests include capacity test, Hybrid Pulse Power Characterization (HPPC) test, Dynamic Stress Test (DST), Urban Dynamometer Driving Schedule (UDDS) test and Federal Urban Driving Schedule (FUDS) test. The capacity test consists of three cycles of CCCV charge/discharge patterns between 3V to 4.05V with charge/discharge rates of 0.5C and CV to 0.05C in about the sum of capacities. The DST, HPPC test are used to examine the dynamic power capability incorporating both discharge and regenerative current pulses and provide the data for parameters identification. The UDDS test and FUDS test are based on real world drivers in midsized vehicles and used to simulate the actual road

driving. For consistency, all experiment except capacity test begins with the battery at 90% SoC for charging ability test.

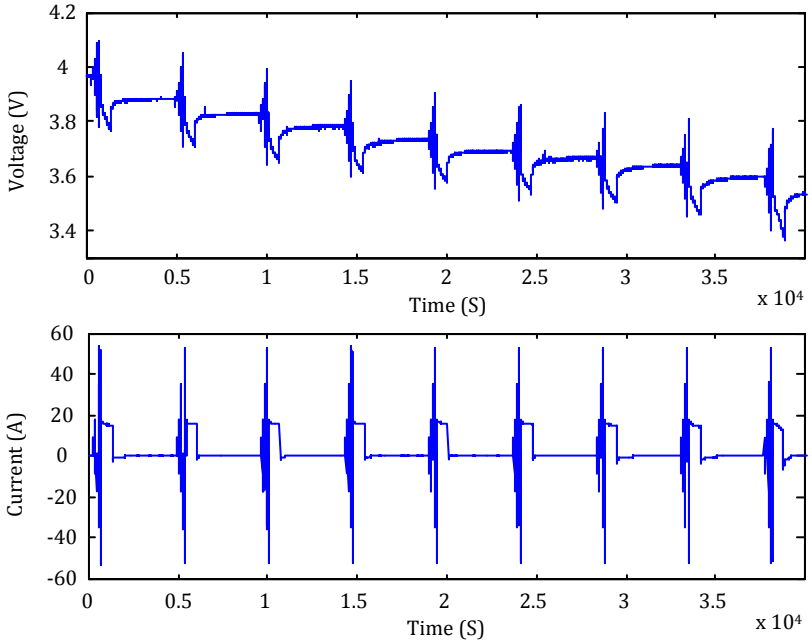

Figure 5.7 Voltage and current in HPPC test

Three cells (#15, #19 and #13) with similar capacity and one cell (#24) with much lower capacity are selected to compose group 1 and group 2 of two cells in parallel. Three cells (#06, #13, and #25) and four cells (#05, #06, #13, and #27) with similar capacity difference are selected to compose the group #3/#4 of three/four cells in parallel. As shown in Table 5.1, group #1 and group #2 each has two cells in parallel with 0.5 Ah and 10.5 Ah capacity difference; Group #3 has three cells with 4 Ah capacity difference; Group #4 has four cells with 2.5 Ah capacity difference.

Table 5.2 Summary of tested Li-ion battery cells

Group Number	Cell number and capacity (Ah)				Capacity difference (Ah)
#1	#15 (31.7)	#19 (31.2)			0.5
#2	#13 (31.7)	#24 (21.2)			10.5
#3	#06 (22.7)	#13 (31.7)	#25 (27.3)		4
#4	#14 (29.7)	#15 (31.7)	#31 (30.1)		1
#5	#04 (31.5)	#11 (31.1)	#20 (24.9)		6
#6	#05 (28.7)	#06 (22.8)	#13 (31.7)	#27 (26.3)	9
#7	#14 (29.7)	#15 (30.7)	#16 (30.2)	#31 (30.1)	1
#8	#02 (24.9)	#03 (29.8)	#18 (29.4)	#26 (29.4)	5.4

Also, EIS of cells #15, #19, #13 and #24 are obtained to verify the aging level of each cell. The EIS test is conducted through the electrochemical workstation ZAHNER IM6 with 10 mV AC excitation from 25 mHz to 1 kHz, as shown in Fig. 5.8. The EIS result indicates that the degradation level of cell #24 is highest among four cells.

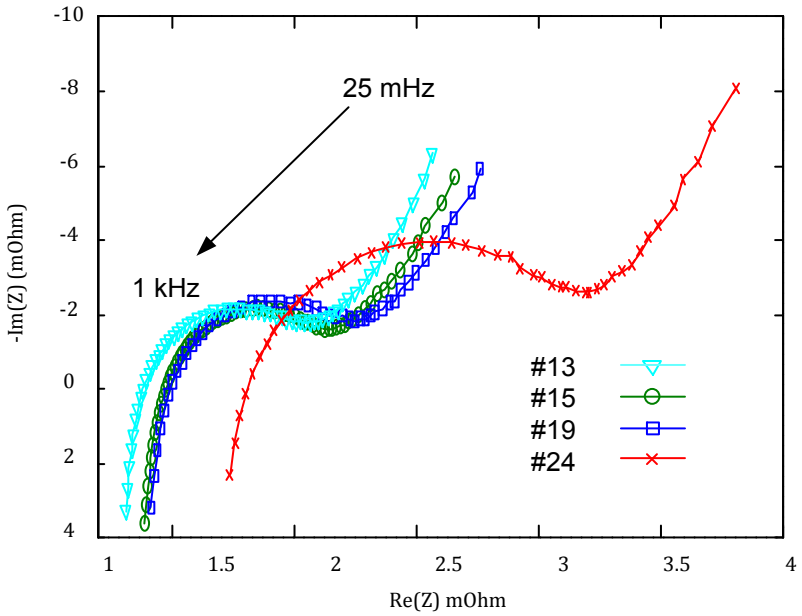

Figure 5.8 EIS test result of Cell # 13, 15, 19, and 24

5.3 Two Cells Connected in Parallel

For two cells connected in parallel, the measured capacities are significantly lower than the sum of individual cells, as the static result shown in Fig. 5.9. The capacity losses range from the minimum 0.5Ah to the maximum 3.5Ah.

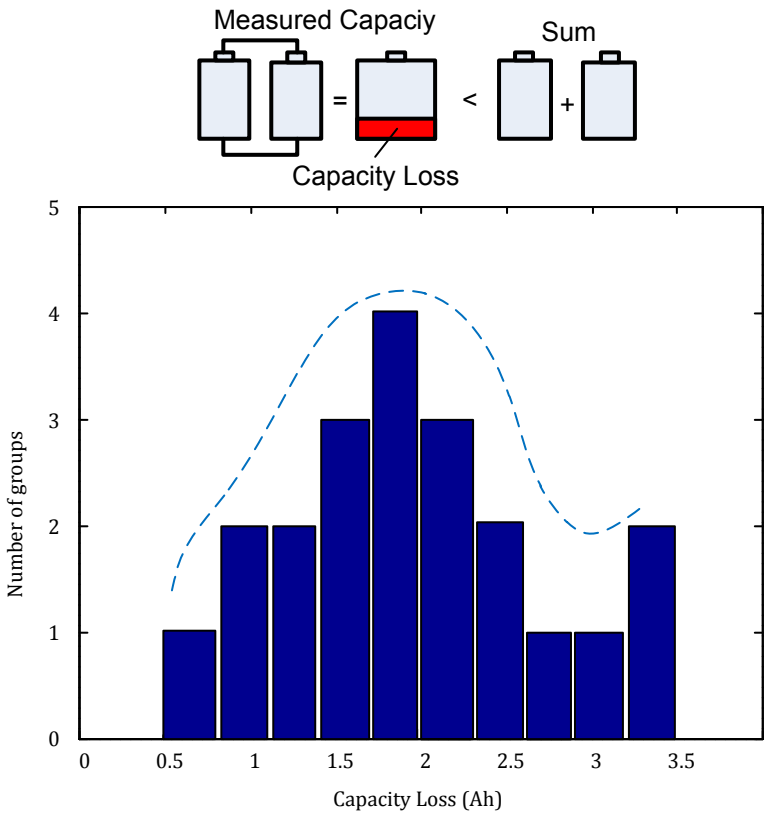

Figure 5.9 Statistics of capacity loss in 2 cells in parallel

Fig 5.10 ~ 5.11 display the discharge current distribution in the capacity tests of 1C (32A)/2C (64A) for group #1 and group #2. Compare with group #2, the current difference between cells in group #1 (<2A) is much lower than group #2. It indicates that the internal resistance or potential difference in group #2 is larger than group #1. According to test results in Chapter 3, the internal resistance of Li-ion battery is an approximate constant at a fixed environmental temperature, unless the SoC approaches nearly 0%. Moreover, we may see the current are still flowing between cells when the discharging is finished after reaching the cut-off voltage. It verifies that the potential

difference between cells is the major factor that causes the current difference, especially at low SoC. The current difference in Group #2 becomes larger near the discharging terminal stage. It indicates that the SoC of cell #24 reaches zero earlier than #13, which causes cell #24 OCV dropping quickly. Then cell #13 is forced to flow more current to maintain same voltage. When discharging current increase, the current difference turns to become larger at the end of discharge and the circulating current increase too. The cells impedance measurement results in Fig 5.8 indicate that significant differences exist in cell #24 and #13, #15, #19. Both imaginary and real part of the impedance of cell #24 are higher than other cells, which shows that the degradation level of #24 is highest among cells.

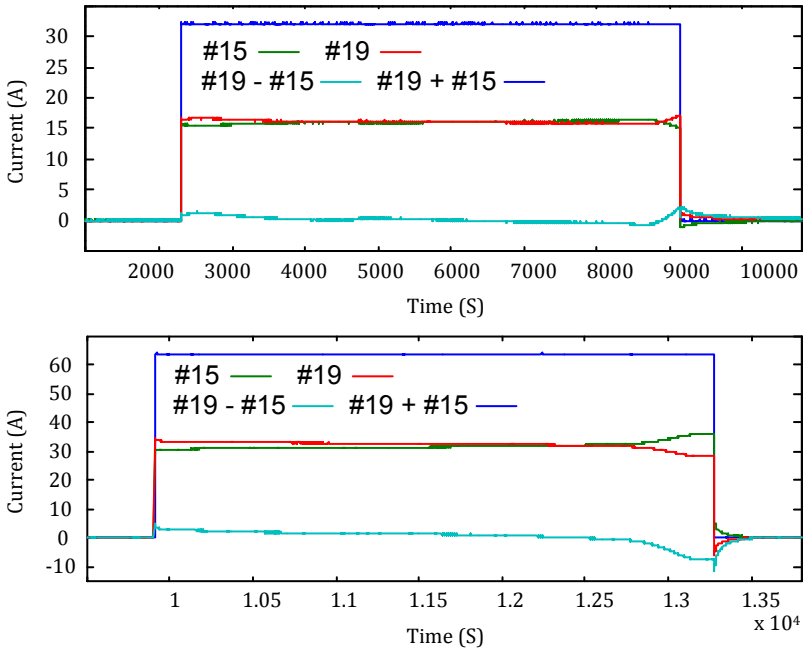

Figure 5.10 Discharge current of cell #15 and #19 at 1C rate (up) and 2C rate (bottom)

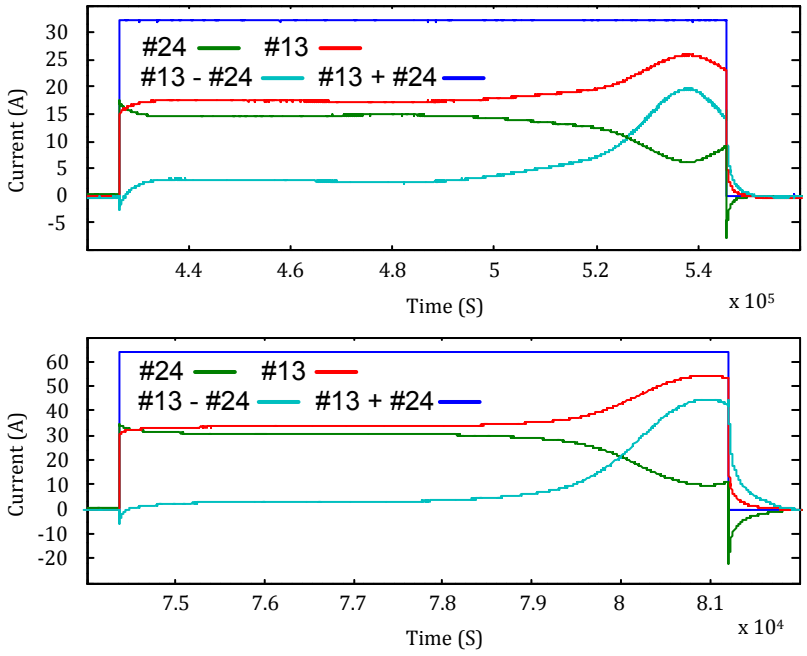

Figure 5.11 Discharge current of cell #13 and #24 at 1C rate (up) and 2C rate (bottom)

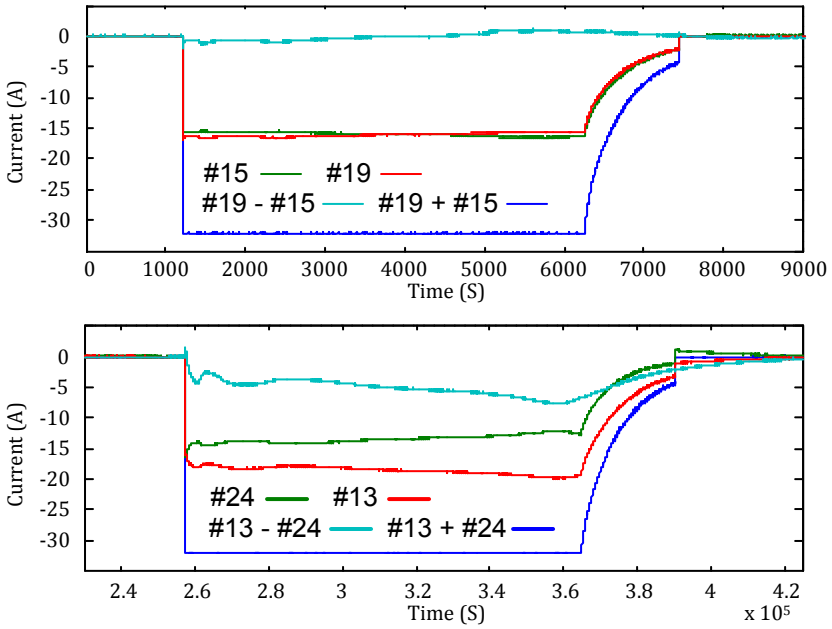

Figure 5.12 Charge current of cell #19 and #15 at 0.5C rate (up); #13 and #24 (bottom)

Dynamic Lumped Model of 2 Cells Connected in Parallel

To further analyze and predict the characteristics of cells parallel-connected packs, the lumped one order equivalent RC circuit model of the battery pack is built in MATLAB/Simulink. The current difference between i_{L1} and i_{L2} is mainly due to the potential difference which is related to the internal parameters in the model such as Ohmic resistance R_o, polarization capacitance C_p , resistance R_p, and *OCV-SoC*. The voltage response of the lumped parameter model can be expressed as:

$$\begin{cases} \dot{U}_k = -\frac{U_k}{R_k C_k} + i_{Lk}/C_k \\ U_{t,k} = OCV_k - U_k - i_{Lk} R_{o,k} \end{cases} (k = 1,..) \quad (5.1)$$

These SoC dependent parameters are identified through the HPPC test data. Select group #1 and #2 as examples; the parameters identification results are plotted in Fig 5.13. The Ohmic resistance R_o difference between #13 and #24 is around 0.8 mOhm in most of the SoC range. The Ohmic resistance difference between cell #19 and #15 is much smaller, within 0.4 mOhm. The polarization capacitance C_p and resistance R_p has the similarity at a constant level.

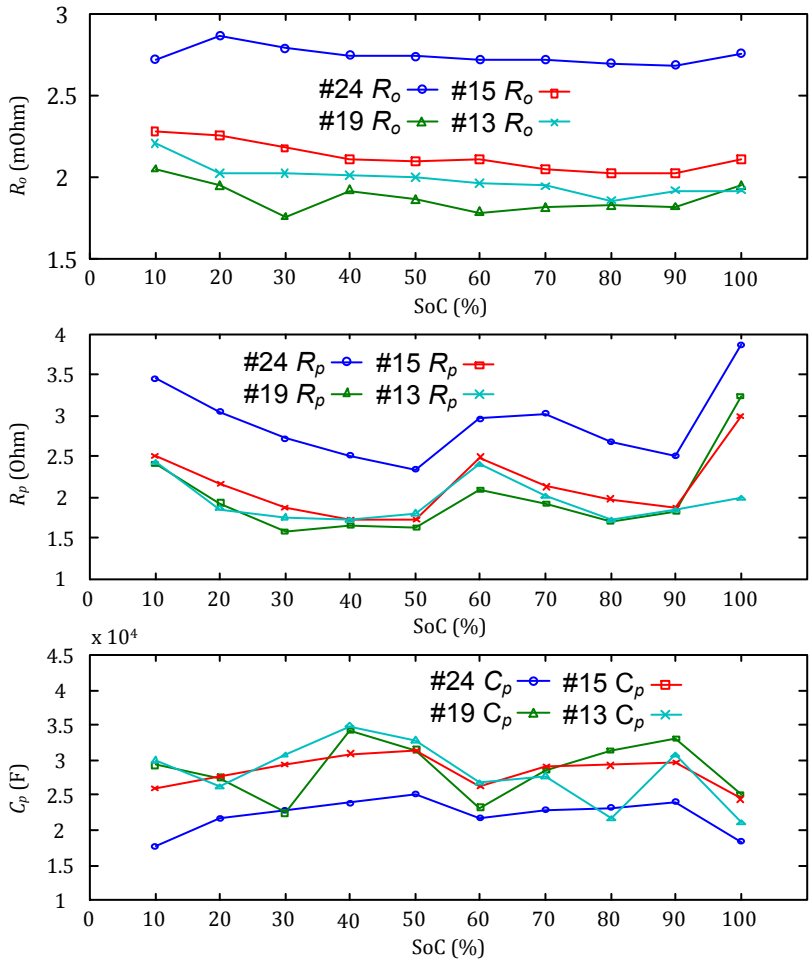

Figure 5.13 SoC dependent parameters identification results of the one order RC equivalent model

Fig. 5.16 shows the dynamic lumped parameter model of the battery pack with two cells in parallel by using MATLAB/Simulink. In this model, two cell models are connected in parallel with a controlled current source as the load. Two same resistors are added into models to present the wire resistance to avoid the algebraic loop problem in the simulation. The SoC calculation of each cell is based the Coulomb counting method.

The initial SoC(0) and nominal capacity can be set separately. Fig 5.17 shows the one order RC equivalent circuit model used in the upper battery pack model. These SoC dependent parameters, OCV, R_p, R_o, and C_p are updated by using look-up tables when SoC changes at the upper pack model.

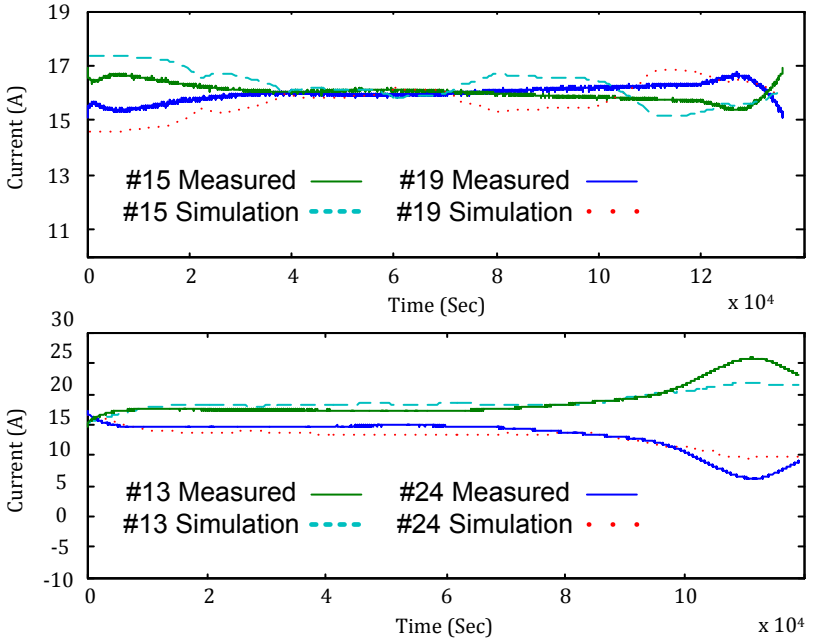

Figure 5.14 Experimental and simulated current distribution at 1C discharging

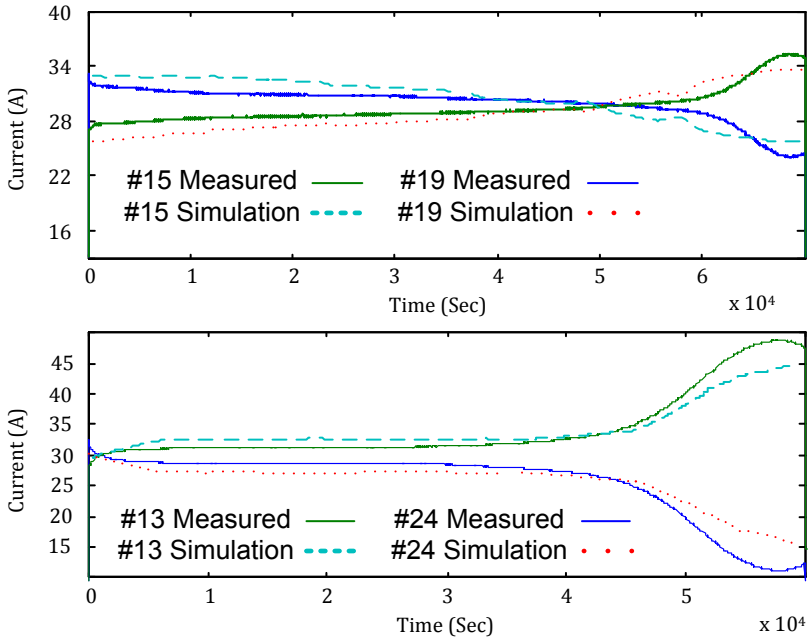

Figure 5.15 Experimental and simulated current distribution at 2C discharging

Simulation results of group #1 and group #2 at 1C and 2C rate are shown in Fig. 5.14 and Fig. 5.15. The current in simulation match the measured current very well at the most range of SoC, except when SoC approaches 0%. The reason is that the OCV and other parameters are highly non-linear especially at the end of discharging. Moreover, HPPC used to identify these parameters only covers 10% to 100% SoC. The thermal effect of Li-ion battery at continuous discharging is also not considered.

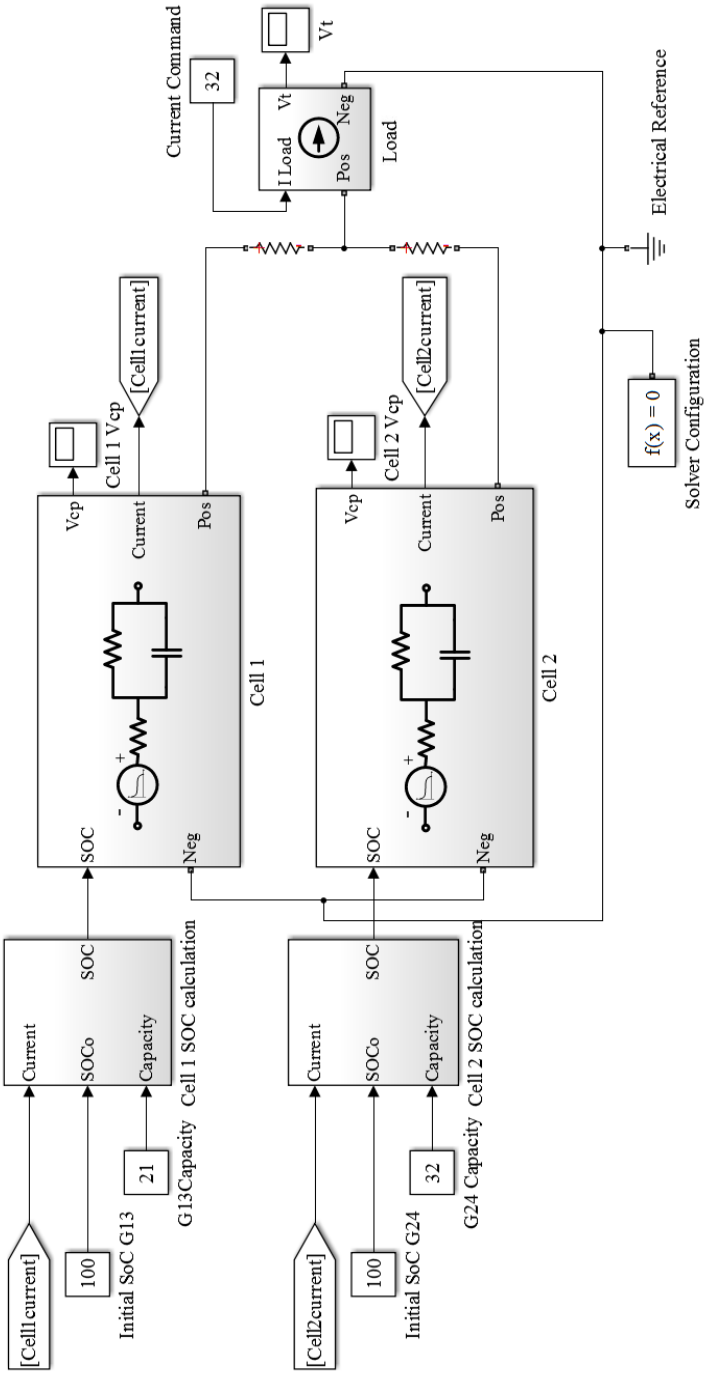

Figure 5.16 Parallel connected battery pack model based on MATLAB/Simulink

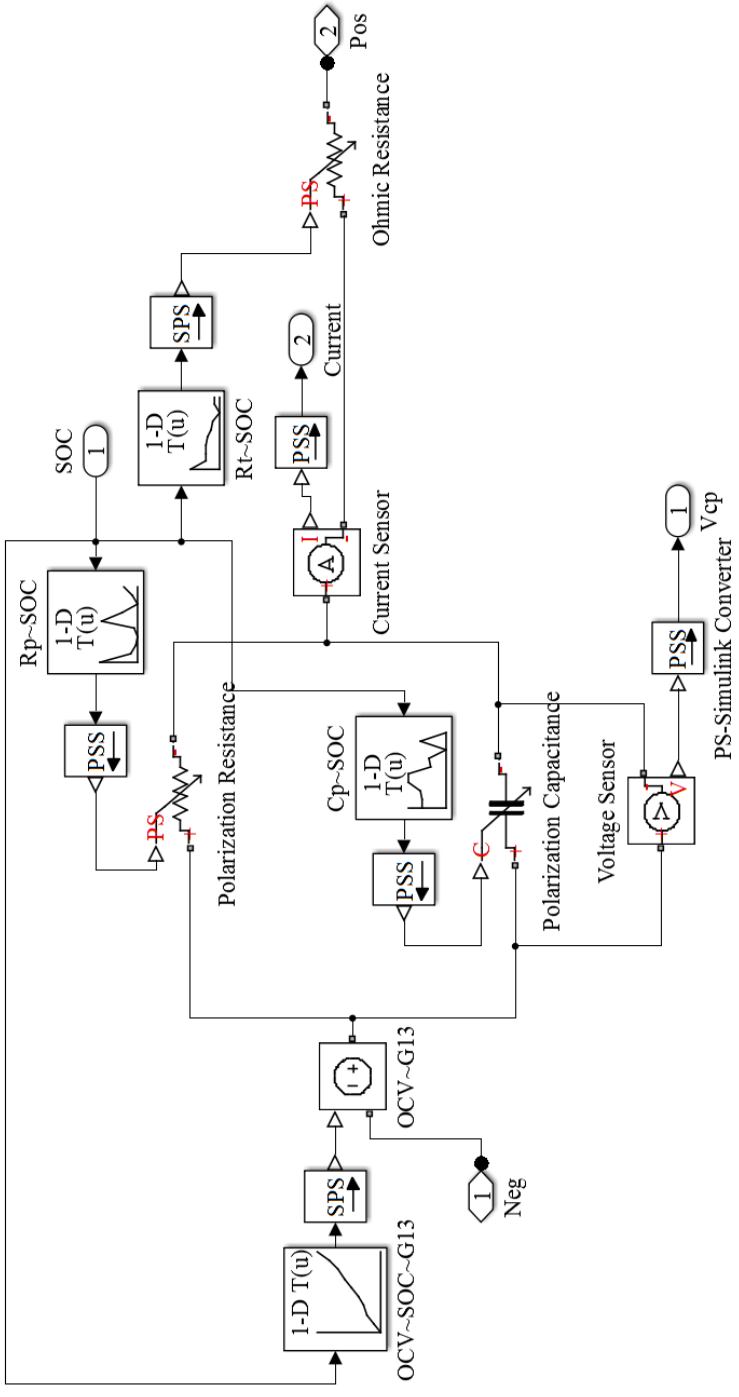

Figure 5.17 One order RC equivalent circuit model used in the pack model

5.4 Three and Four Cells in Parallel

By increasing the number of cells in parallel, the current average difference between each cell is decreased. The discharge current of Group #3~#8 is shown in Fig. 5.18 and Fig. 5.19. The capacity difference between the highest and the lowest remains around 10 Ah, same as Group #2. With 3 Ah capacity difference between each cell in Group #4, the discharging current difference is around 2 A. The distribution shows that the current of each cell is proportional to capacity, except when SoC is close to zero.

It is also noticed that group #5 and group #8 are composed of cells with similar aging levels. The current of each cell is very even at most of the time during discharging and charging. However, unbalanced current in cells increase when SoC is lower than 15%. The current in cell #15 increase to 125% of the ideal current and cell# 16 current increase to 130%. Therefore, it may come a conclusion that the final 10%~15% SoC capacity of parallel connected cells should be avoided to use to prevent the high unbalancing current.

5.5 Summary

This chapter mainly studies the characteristics of parallel connected battery packs composed of cells with different aging levels. The characteristics of parallel connected battery packs are discussed based on experimental tests and simulation. Cells in parallel can lead to accelerated degradation process due to the unbalanced current distribution.

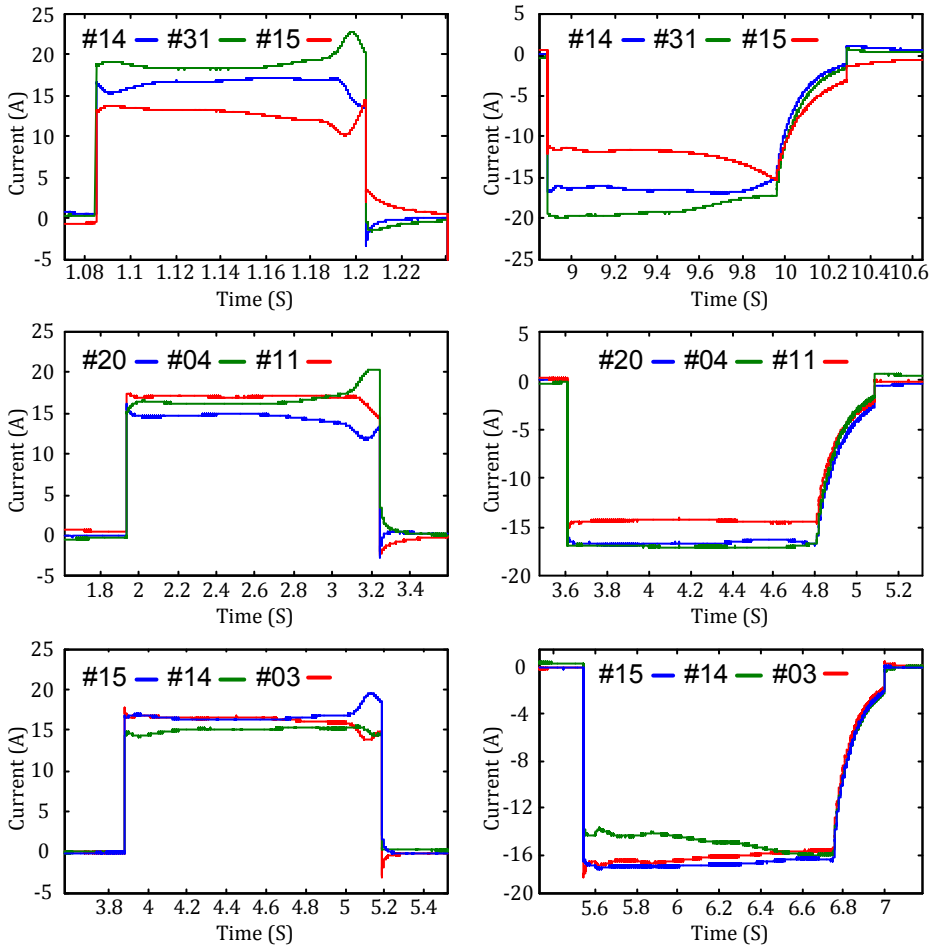

Figure 5.18 Discharge current (left) and charge current (right) distributions in three cells in parallel (Group #3, #4 and #5).

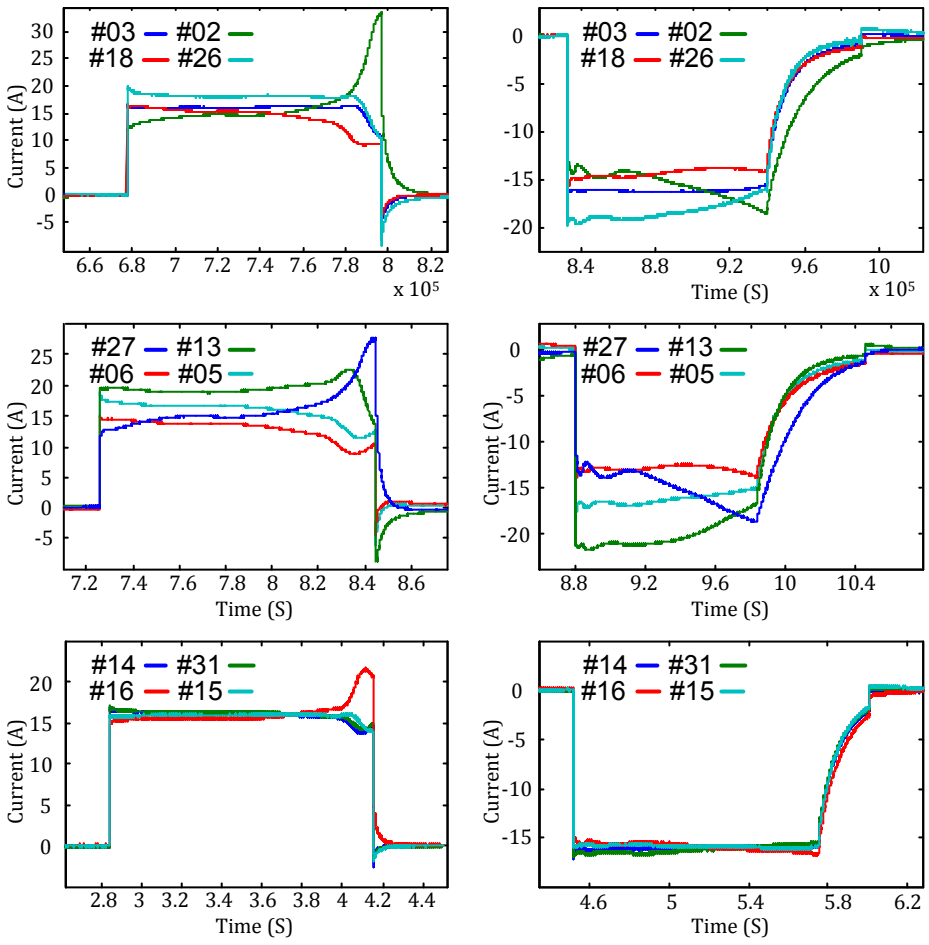

Figure 5.19 Discharge current (left) and charge current (right) distributions in four cells in parallel (Group #3, #4 and #5).

CHAPTER 6

Conclusions and Future Work

6.1 Conclusion

The Li-ion modeling methods and states estimation algorithms proposed in this dissertation provide a systematic methodology for analyzing and solving the temperature and aging uncertainties in battery management systems. In particular, these techniques are applied to build the model for used Li-ion battery pack from in electric vehicles under different temperature environment.

Chapter 2 introduces the basic knowledge of Li-ion battery modeling and SoC estimation. First, the thesis focuses on the equivalent circuit model and associated parameters identification. A two RC network circuit model is selected to demonstrate the goodness of prediction results. Next, the battery model based SoC estimation using AEKF algorithm is presented. This method uses the error between the calculated voltage and measured voltage to correct the SoC estimation obtained through coulomb counting. The experimental results show the closed-loop AEKF SoC estimation method can solve the initial SoC value problem and provide good estimation result.

In Chapter 3, the thesis focuses on the understanding of temperature dependent performance of Li-ion battery. First, the temperature influence is investigated through EIS experimental tests and theoretical analysis. The increased charge transfer polarization is the major factor that limits the battery performance under low temperature. The model

compensation functions for equivalent circuit model are derived from some experimental tests data to increase the model adaptability for different temperatures.

In Chapter 4, the battery aging mechanism is revisited first; it shows that the major aging effect happens at the negative electrode and electrolyte. Then a series of aging tests is carried out to enhance the understanding of the degradation path. The wide SoC range and high charge current can exacerbate the Li-ion aging problem. In the latter part of Chapter 4, the SoH estimation method based incremental capacity analysis is presented. Moreover, the method is applied to experimental data to estimate SoH and results show it can track the SoH for different Li-ion batteries including NCM, LFP, and LMO. Finally, a bias correction modeling method using the SoH is developed for the modeling of the aged battery.

Study of parallel-connected battery packs is presented in Chapter 5. The inconsistency problem in battery cells with different aging level and its influence to parallel-connected packs are discussed. The parallel connected battery pack model is developed to simulate the current distribution in parallel connected cells. Both simulation and experimental test results show that the current difference in parallel connected cells increases when the SoC is close to 0%, despite the aging level and the number of cells in parallel.

This dissertation provides five distinct contributions toward the Li-ion battery modeling and states estimation for electric vehicle applications. In the present work, we:

1. Study the equivalent circuit model based Li-ion battery modeling methods and SoC estimation. Develop AEKF based SoC estimation algorithm and apply it to RC circuit model to solve the initial SoC value problem and provide excellent robustness in SoC estimation. (Chapter 2)
2. Study the temperature influence to Li-ion battery through the EIS tests and theoretical analysis. Build analytical compensation functions to enhance the equivalent circuit model adaptability for different temperatures. (Chapter 3)
3. Study the Li-ion battery aging mechanism, including various SoH degradation metrics. Conduct a series of aging tests in different batteries to understand the critical degradation factors and paths. (Chapter 4).
4. Develop the novel SoH estimation method and bias-correction modeling method based on ICA peaks in the dQ/dV curves. This bias-correction modeling method can update the battery model by using the voltage data during constant charging and track the SoH in real-time. (Chapter 4)
5. Study the characteristics of parallel connected battery packs composed of cells with different aging levels. Understand the current distribution phenomenon in parallel connected cells due to the cells inconsistency. Build the parallel connected cells model to predict current in cells. (Chapter 5)

6.2 Future Work

The proposed modeling method and resulting algorithms make notable steps towards developing BMS with enhanced ability against temperature and aging uncertainties. Nonetheless, there exist several opportunities to advance the work presented here.

In this study, we use forced air cooling/heating temperature chamber in the experimental test. So the heat generation and thermal effect from Lithium-ion battery itself are ignored. We can conduct research on the thermal effect from the battery itself by using heat insulation material (adiabat) in the test and analyze the heat generation from physical and electrochemical sides. Furthermore, we can build correlation functions between heat generation and SoH to increase the functionality of BMS.

As we discussed in Chapter 4, model parameters identification is a promising method to estimate the SoH of Li-ion battery. This approach does not need any additional equipment and can be integrated to BMS easily. The critical problems in this approach are which specific battery model we should use for identification and how to identify these parameters based on actual data collected from EVs. Another issue is that these model parameters are usually influenced by hysteresis effect and temperature effect. The parameters identification can be implemented if we can decouple the battery model from these effects. Additional, the requirement of fast and accurate data acquisition and high computation task also raise challenges in the BMS hardware design part.

APPENDICES

APPENDIX A

MATLAB source code of data processing in ICA test in chapter 4

```
data_v_raw=v;
data_time_raw=t;
data_current=i;
data_chargecap_arbin=cap;
data_chargecap_arbin=data_chargecap_arbin-min(data_chargecap_arbin);
data_time_raw=data_time_raw-min(data_time_raw);
data_chargecap=data_time_raw.*data_current;
size=length(data_v_raw);

dv1=[];dv2=[];dv3=[];dv4=[];dv5=[];
v_axis=[];c_axis=[];
j=[];
k=fix(size/100);
l=[];
data_v_1=smooth(data_v_raw,size/20,'sgolay',2);

for i=(k+1):size

j=(data_v_1(i)-data_v_1(i-k))/(data_chargecap(i)-data_chargecap(i-k));
    dv1=[dv1 j];
    v_axis=[v_axis 0.5*(data_v_1(i)+data_v_1(i-k))];
    c_axis=[c_axis
0.5*(data_chargecap_arbin(i)+data_chargecap_arbin(i-k))];
end

clear j; j=[];
subplot (4,3,1);plot(v_axis,1./dv1);title('³õ´Î');

err_raw=data_v_1-data_v_raw;
subplot (4,3,2);plot(data_time_raw,err_raw);
err=smooth(err_raw,k,'sgolay',2);
hold on;plot(data_time_raw,err,'r');

for i=length(err)-10000:-1:1
if abs(err(i))>0.0004
    l=i+500;break
end
end
l
data_v_2raw=data_v_raw(1:l);
stem(data_time_raw(l),err(l),'linewidth',5);
hold off;title('×¢Òâ·ùÖµ¹ý´óµÄ²¿·Ö');
size2=length(data_v_2raw);
```

```
subplot (4,3,3);
for i=5:size2
    data_v_2=smooth(data_v_2raw,size2/i,'sgolay',2);
    err2=data_v_2-data_v_2raw;
    plot(err2,'r');hold on;
    if mean(abs(err2))<0.001
        i
    break
    end
    i
end
hold off;
data_v_3=[data_v_2; data_v_1(l+1:end)];

subplot (4,3,4);plot(data_time_raw,err_raw,'r');hold
on;plot(data_time_raw,data_v_3-data_v_raw);
title('¶Ô±ÈÐÂ¾ÉÈ¥³ýµÄÔëÉù');
subplot (4,3,5);plot(data_time_raw,data_v_raw,'r');hold
on;plot(data_time_raw,data_v_3);stem(data_time_raw(l),data_v_3(l),'lines
tyle','none');


clear v_axis c_axis;
v_axis=[]; c_axis=[];

for i=(k+1):size

j=(data_v_3(i)-data_v_3(i-k))/(data_chargecap(i)-data_chargecap(i-k));
    dv3=[dv3 j];
    v_axis=[v_axis 0.5*(data_v_3(i)+data_v_3(i-k))];
    c_axis=[c_axis
0.5*(data_chargecap_arbin(i)+data_chargecap_arbin(i-k))];

end

clear j; j=[];

subplot (4,3,6);plot(v_axis,1./dv3,'b');hold on;plot(v_axis,1./dv1,'r');
plot(v_axis,smooth(1./dv3,k,'sgolay',2),'k');
hold off;title('×îÓÕ');

err_raw2=data_v_3-data_v_raw;
subplot (4,3,7);plot(data_time_raw,err_raw2);
err2=smooth(err_raw2,k,'sgolay',2);
hold on;plot(data_time_raw,err2,'r');

for i=l+1:1:size
if abs(err2(i))>0.0004
    m=i-500;break
```

```
end
end
m
data_v_4raw=data_v_raw(m:end);
stem(data_time_raw(m),err2(m),'linewidth',5);
hold off;title('×¢Òâ·ùÖµ¹ý´óµÄ²¿·Ö');
size3=length(data_v_4raw);

subplot (4,3,8);
for i=5:size3
    data_v_4=smooth(data_v_4raw,size3/i,'sgolay',2);
    err3=data_v_4-data_v_4raw;
    plot(err3,'r');hold on;
    if mean(abs(err3))<0.001
        i
    break
    end
    i
end
hold off;
data_v_5=[data_v_3(1:m-1);data_v_4];

subplot (4,3,9);plot(data_time_raw,err_raw2,'r');hold
on;plot(data_time_raw,data_v_5-data_v_raw,'k');hold off;
title('¶Ô±ÈÐÂ¾ÉÈ¥³ýµÄÔëÉù');
subplot (4,3,10);plot(data_time_raw,data_v_raw,'r');hold
on;plot(data_time_raw,data_v_5);stem(data_time_raw(m),data_v_5(m),'lines
tyle','none');hold off;

clear v_axis c_axis;
v_axis=[]; c_axis=[];

for i=(k+1):size

j=(data_v_5(i)-data_v_5(i-k))/(data_chargecap(i)-data_chargecap(i-k));
    dv4=[dv4 j];
    v_axis=[v_axis 0.5*(data_v_5(i)+data_v_5(i-k))];
    c_axis=[c_axis
0.5*(data_chargecap_arbin(i)+data_chargecap_arbin(i-k))];

end


clear j; j=[];

subplot (4,3,11);plot(v_axis,1./dv4,'b');hold on;plot(v_axis,1./dv1,'r');
plot(v_axis,smooth(1./dv4,k,'sgolay',2),'k');
hold off;title('×îÕÕ');
```

```
dvdq_final=smooth(1./dv4,k,'sgolay',2);

savefile = 'dvdq_4.9080_24_nov_2014.mat';
save(savefile, 'v_axis','c_axis', 'dvdq_final');
```

APPENDIX B

MATLAB source code of AEKF SoC estimation in chapter 2

```
% Adaptive Extended Kalman Filter for SOC and C Estimation
function [SOCEst,CEst,YEst,ComTime] =
EKF_SOC_C_Sim_v2(Y,I,T,C,THETA,OCVData,SOCData,dOCVdSOCData)

%% Define Noise Level
% For Simulation Data
W1 = 0.001^2;         % Variance of noise for z (state): SOC
W2 = 0.0002;          % Variance of noise for C (state): capacity

V1 = 0.1^2;           % Variance of noise for y (meas.): SOC
V2 = 0.1^2;           % Variance of noise for y (meas.): capacity

rand('state',sum(100*clock));    % Shuffle the pack!
randn('state',sum(100*clock));   % Shuffle the pack!

%% Initialize Variables
Eta = 1.0;                % Initial value for columbic efficiency eta
nT = length(T);           % Time length for SOC estimation

% Initilization
SOC_ekf = 0.90;           % EKF estimate of the mean of SOC.
SOC_ekf_pred = SOC_ekf;   % EKF one-step-ahead estimate of the mean of SOC.

SIGSOC = W1;              % EKF estimate of the variance of SOC.
SIGSOC_pred = SIGSOC;     % EKF one-step-ahead estimate of the variance
of SOC.

C_ekf = C - 0.5;          % EKF estimate of the mean of capacity
C_ekf_pred = C_ekf;       % One-step-ahead predicted values of capacity

SIGC = W2;                % EKF estimate of the variance of capacity.
SIGC_pred = SIGC;         % EKF one-step-ahead estimate of the variance of
capacity.

Y_pred = 4;               % Predicte measurement value


%% Initilize ESC Model States
% Initialize Hysterisis State
h = zeros(1,1);

% Initialize Filter State
nf  = (length(THETA(5:end))+1)/2;
```

```
f = zeros(nf,1);


SOCEst(1) = SOC_ekf;
CEst(1) = C_ekf;
YEst(1) = Y_pred;

DgDC_k_1 = 0;
DSOCPredDC_k_1 = 0;
DSOCDC_k_1 = 0;
LSOC_k_1 = 0;

 ComTime = zeros(2,nT);
%% Start Loop
for k = 2:nT
    tic
%     k
    % Prediction Step for Capacity
    C_ekf_pred = C_ekf;
    SIGC_pred = SIGC + W2;

    % Prediction Step for SOC
    delta_SOC = Eta*(T(k)-T(k-1))/3600./C_ekf_pred*I(k-1);
    SOC_ekf_pred = SOC_ekf + delta_SOC;
    ASOC = 1;          % df/dSOC
    SIGSOC_pred = ASOC*SIGSOC*ASOC' + W1;

    ComTime(1,k) = toc;

    % Correction Step for SOC
    [Y_pred,h,f] = YEstESC_EKF(THETA,I(k-1:k),T(k-1:k),....
        SOC_ekf_pred,Eta,C_ekf_pred,h,f,OCVData,SOCData);
    CSOC = interp1(SOCData,dOCVdSOCData,SOC_ekf_pred,'line'); % dg/dSOC
    tic
    MSOC = CSOC*SIGSOC_pred*CSOC' + V1;               % Innovations
covariance.
    LSOC_k = SIGSOC_pred*CSOC'/MSOC;                 % Kalman gain.
    SOC_ekf = SOC_ekf_pred + LSOC_k*(Y(k)-Y_pred);     % Measurement update
    SIGSOC = SIGSOC_pred - LSOC_k*CSOC*SIGSOC_pred;     % Variance update
    ComTime(1,k) = ComTime(1,k) + toc;

    PgPC = 0;             % Partial deriviative of g w.r.t. C

    tic
    % Correction Step for C
    % Recursively Compute dg/dC
    DSOCDC_k_1 = DSOCPredDC_k_1 - LSOC_k_1*DgDC_k_1;
    DSOCPredDC_k = -delta_SOC/C_ekf_pred + DSOCDC_k_1;
    PgPSOC = CSOC;         % Partial deriviative of g w.r.t. SOC
```

```
    DgDC_k = PgPC + PgPSOC*DSOCPredDC_k;
    CC = DgDC_k;          % dg/dC
    % Update Previous Values for Recursively Computing dg/dC
    DgDC_k_1 = DgDC_k;
    DSOCPredDC_k_1 = DSOCPredDC_k;
    LSOC_k_1 = LSOC_k;

    ComTime(2,k) = toc;

    tic

    % Update C
    MC = CC*SIGC_pred*CC' + V2;                % Innovations covariance.
    LC = SIGC_pred*CC'*inv(MC);                % Kalman gain.
    C_ekf = C_ekf_pred + LC*(Y(k)-Y_pred);       % Measurement update
    SIGC = SIGC_pred - LC*CC*SIGC_pred;         % Variance update

    ComTime(1,k) = ComTime(1,k) + toc;

    % Data Log
    CEst(k) = C_ekf;
    SOCEst(k) = SOC_ekf;
    YEst(k) = Y_pred;
end

function [YEst,h,f] =
YEstESC_EKF(THETA,I,T,SOC,Eta,C,h_his,f_his,OCVData,SOCData)
nData = length(SOC);

%% Compute OCV
OCV = interp1(SOCData,OCVData,SOC','line');

%% Compute Ohmic Loss
if I(2) > 0
    OL = I(2)*THETA(1);  % Charge I*R+
else
    OL = I(2)*THETA(2);  % DisCharge I*R-
end

%% Compute Hysterisis
% Compute h matrix
F = exp(-abs(Eta*I(1).*THETA(4).*(T(2)-T(1))/3600./C));
h = F.*h_his' + (1 - F)*sign(I(1));

% Compute hysterisis
HYST = THETA(3)*h;

%% Compute Filter Voltage
```

```
if length(THETA) == 4 % No filter
    FILT = zeros(nData,1);
    f = zeros(nData,1);
else
    % Extract Af and G
    nf  = (length(THETA(5:end))+1)/2;
    Af = THETA(5+nf-1:5+2*nf-2);
    G(1:nf-1) = THETA(5:5+nf-2);
    G(nf) = - (1 - Af(nf))*sum(G(1:nf-1)./(1 - Af(1:nf-1)));
    Bf = ones(1,nf)*1e-4;

    % Compute f
    f = repmat(Af,nData,1).*f_his' + repmat(Bf,nData,1)*(-I(1));

    % Compute filter pole voltage
    FILT = f*G';
end

YEst = OCV + OL + HYST + FILT;
YEst = YEst';
h = h';
f = f';
```

BIBLIOGRAPHY

1. Q. Zhuang, S. Xu, X. Qiu, Y. Cui, L. Fang, and S. Sun, “Diagnosis of Electrochemical Impedance Spectroscopy in Lithium Ion Batteries,” *Progress in Chemistry*, vol. 22, No. 6 Jun 2010.
2. F. Nobili, M. Mancini, S. Dsoke, R. Tossici, R. Marassi, “Low-temperature behavior of graphite–tin composite anodes for Li-ion batteries,” *Journal of Power Sources*, vol. 195, pp. 7090–7097.
3. S. S. Zhang, K. Xu, J. L. Allen, and T. R. Jow, “Effect of propylene carbonate on the low temperature performance of Li-ion cells,” *Journal of Power Sources*, vol. 110, pp. 216–221.
4. Z. Ma, J. Jiang, C. Mi, W. Shi, W. Zhang, “Investigation of path dependence in commercial lithium-ion cells for pure electric bus applications: aging mechanism identification,” *Journal of Power Sources*, vol. 274, pp. 29–40.
5. D. Zhang, B.S. Haran, A. Durairajan A, et al. “Studies on capacity fade of lithium-ion batteries,” *Journal of Power Sources*, vol. 91, pp. 122–129.
6. Levi M D，Aurbach D. “Simultaneous Measurements and Modeling of the Electrochemical Impedance and the Cyclic Voltammetric Characteristics of Graphite Electrodes Doped with Lithium,” *Journal of Physical Chemistry B*, vol. 101, pp. 4630–4640.
7. http://www.chademo.com
8. C. Mi, A. Masrur, and D. W. Gao, “Hybrid Electric Vehicles: Principles and Applications with Practical Perspectives,” Wiley, 2011
9. R. Xiong, F. Sun, X. Gong and H. He, "Adaptive state of charge estimator for lithium-ion cells series battery pack in electric vehicles," *Journal of Power Sources*, vol. 242, pp. 699–713.
10. U.S. Department of Energy, Idaho National Laboratory, “2011 Nissan Leaf – VIN 0356 Advanced Vehicle Testing – Beginning-of-Test Battery Testing Results”, http://www1.eere.energy.gov/vehiclesandfuels/avta/pdfs/fsev/battery_leaf_0356.pdf.
11. U.S. Department of Energy, Idaho National Laboratory, “2013 Chevrolet Volt Advanced Vehicle Testing – Beginning-of-Test Battery Testing Results”, http://avt.inel.gov/pdf/EREV/fact2013chevroletvolt.pdf.
12. S. Piller, M. Perrin and A. Jossen, “Methods for state-of-charge determination and their applications,” *Journal of Power Sources*, vol. 96, pp. 113–120.
13. C. Rahn and C. Wang, “Battery Systems Engineering,” *Wiley*, 2013.

14. Berndt, D., E. Meissner, and W. Rusch, “Aging effects in valveregulated lead-acid batteries,” in *Telecommunications Energy Conference*, INTELEC ’93. 15th International, vol. 2, pp. 139 –145.

15. P. Ruetschi, “Aging mechanisms and service life of lead acid batteries,” *Journal of Power Sources*, vol. 127, pp. 33–44.

16. C. Schlasza, “Review on the aging mechanisms in Li-ion batteries for electric vehicles based on the FMEA method,” *Transportation Electrification Conference and Expo (ITEC)*, 2014 IEEE, pp. 1–6.

17. H. Dai, X. Zhang, W. Gu, X. Wei, Z. Sun, “A Review of the Life Studies on Lithium-ion Batteries for EV Applications,” *Energy Procedia*, vol. 75, pp. 1920–1925.

18. J. Vetter, P. Novák, M. R. Wagner et al., “Ageing mechanisms in lithium-ion batteries,” *Journal of Power Sources*, vol. 147, pp. 269–281, 2005.

19. K. Xu, “Nonaqueous liquid electrolytes for lithium-based rechargeable batteries,” *Chemical Reviews*, vol. 104, pp. 4303–4417.

20. M. Takahashi, S. Tobishima, K. Takei, et al. “Reaction behavior of LiFePO4 as a cathode material for rechargeable lithium batteries,” *Solid State Ionics*, vol. 148, pp. 283–289.

21. R Malik, D. Burch, M. Bazant, et al. “Particle Size Dependence of the Ionic Diffusivity,” *Nano Letters*, vol. 10, pp.4123–4127.

22. G. Beauregard, “Report of Investigation NRECA Plug-in HEV Fire,” Phoenix: ETEC, 2008.

23. T. Ohzuku, Y. Iwakoshi, K. Sawai, “Formation of Lithium-Graphite Intercalation Compounds in Nonaqueous Electrolytes and Their Application as a Negative Electrode for a Lithium Ion (Shuttlecock) Cell,” *Journal of the Electrochemical Society*, vol. 140, pp. 2490–2498.

24. S. Flandrois, B. Simon, “Carbon materials for lithium-ion rechargeable batteries,” *Carbon*, vol. 37, pp. 165–180.

25. Blanke, H., O. Bohlen, S. Buller, R. W. D. Doncker, B. Fricke, A. Hammouche, D. Linzen, M. Thele, and D. U. Sauer “Impedance measurements on leadCacid batteries for state-of-charge, stateof-health and cranking capability prognosis in electric and hybrid electric vehicles,” *Journal of Power Sources*, vol. 144, pp. 418–425.

26. Ala A. Hussein. “Capacity fade estimation in electric vehicles Li-ion batteries using artificial neural networks,” *Energy Conversion Congress and Exposition (ECCE)*, 2013 IEEE, pp. 677–681.

27. W. He, N. Williard, M. Osterman, M. Pecht, “Prognostics of lithium-ion batteries based on Dempster–Shafer theory and the Bayesian Monte Carlo method,” *Journal of Power Sources*, vol 196, pp. 10314–10321.

28. J. P. Wang, L. Xu, J. G. Guo, L. Ding, “Modelling of a battery pack for electric vehicles using a stochastic fuzzy neural network,” *Journal of Automobile Engineering*, vol. 223, pp. 27–35.

29. M. A. Roscher, J. Assfalg, and O. S. Bohlen, “Detection of utilizable capacity deterioration in battery systems,” *IEEE Transactions on Vehicular Technology*, vol. 60, pp. 98–103.

30. I. Bloom, “Differential voltage analyses of high-power, lithium-ion cells: 1. Technique and application,” *Journal of Power Sources*, vol 139, pp 295–303.

31. J. C. Forman, S. J. Moura, J. L. Stein, and H. K. Fathy, “Parameter Identification of the Doyle-Fuller-Newman Model Based on Experimental Cycling of a Li-ion LiFePO4 Battery Using a Genetic Algorithm,” *2011 American Control Conference*, 2011.

32. S. Buller, M. Thele, R. Doncker, E. Karden, “Impedance-Based Simulation Models of Supercapacitors and Li-Ion Batteries for Power Electronic Applications,” *IEEE Transactions on Industry Applications*, vol. 41, pp. 742–747.

33. E. Karden, P. Mauracher, F. Schöpe, “Electrochemical modelling of lead/acid batteries under operating conditions of electric vehicles,” *Journal of Power Sources*, vol. 64, pp. 175–180.

34. B.Y. Liaw, G. Nagasubramanian, R.G. Jungst, D.H. Doughty, “Modeling of Lithium ion cells—A simple equivalent-circuit model approach,” *Solid State Ionics*, vol. 175, pp. 835–839.

35. Y.H. Chiang, W.Y. Sean, J.C. Ke, “Online estimation of internal resistance and open-circuit voltage of lithium-ion batteries in electric vehicles,” *Journal of Power Sources*, vol. 196, pp. 3921–3932.

36. T. Kim T, A.W. Qiao, “A hybrid battery model capable of capturing dynamic circuit characteristics and nonlinear capacity effects” *IEEE Transactions on Energy Conversion*, vol. 26, pp. 1172–1180.

37. Cho. S, H. Jeong, C. Han, S. Jin, J.H. Lim, J. Oh, “State-of-charge estimation for lithium-ion batteries under various operating conditions using an equivalent circuit model,” *Computers & Chemical Engineering*, vol. 41, pp.1–9.

38. G. L. Plett, “Extended Kalman filtering for battery management systems of LiPB-based HEV battery packs, Part 3: State and parameter estimation,” *Journal of Power Sources*, vol. 134, no. 2, pp. 277–292.

39. B. Bamieh and L. Giarré. “Identification of Linear Parameter Varying Models,” *International Journal of Robust and Nonlinear Control*, 2002, pp. 841–853.

40. V. Verdult, M. Verhaegen, “Subspace identification of multivariable linear parameter-varying systems,” *Automatica*, vol. 38, pp. 805–814.

41. J. Chiasson and B. Vairamohan, “Estimating the state of charge of a battery,” *IEEE Transactions on Control Systems Technology*, vol. 13, no. 3, pp. 465–470.

42. J Xu, CC Mi, B Cao, J Deng, S Chen, S Li, “The State of Charge Estimation of Lithium-Ion Batteries Based on a Proportional Integral Observer,” *IEEE Transactions on Vehicular Technology*, vol. 63, pp. 1614–1621.

43. D. Aurbach, K. Gamolsky, B. Markovsky, “The Study of Surface Phenomena Related to Electrochemical Lithium Intercalation into Lix MO y Host Materials (M = Ni, Mn),” *Journal of Electrochemical Society*, vol. 147, pp. 1322–1333.

44. M.D Levi, D. Aurbach, “Simultaneous Measurements and Modeling of the Electrochemical Impedance and the Cyclic Voltammetric Characteristics of Graphite Electrodes Doped with Lithium,” *The Journal of Physical Chemistry B*, vol. 101, pp. 4630–4640.

45. C. Mi, M. A. Masrur, and D. W. Gao, Hybrid Electric Vehicles: Principles and Applications with Practical Perspectives, *John Wiley & Sons*, 2011.

46. US-DOE, “2013 Annual Energy Report”, Retrieved from http://www.eia.doe.gov/

47. Wärtsilä Corporation, Retrieved from http://www.wartsila.com/.

48. Toyota Motor Corporation, Retrieved from http://www.toyota.com/.

49. Nissan Motor Corporation, Retrieved from http:// www.nissan-global.com/.

50. General Motors Company, Retrieved from http:// www.gm.com/.

51. D. Linden, T.B. Reddy, eds. Handbook of Batteries, 3rd Edition, *New York: The McGraw-Hill Companies, Inc.*; 2002.

52. United States Advanced Battery Consortium. Goals for Advanced Batteries for EVs. Retrieved from http://www.uscar.org/guest/article_view.php?articles_id=85, 2012.

53. Harris W. “Electrochemical Studies in Cyclic Esters,” *dissertation*, California: University of California, Berkeley, 1959.

54. R.A. Huggins, Advanced batteries: materials science aspects, *Springer*, 2009.

55. J. Cho, G. Kim, “Enhancement of Thermal Stability of LiCoO2 by LiMn2O4 Coating,” *Electrochemical and Solid-State Letters*, vol. 2, pp. 253–255.

56. A.K. Padhi, K.S. Nanjundaswamy, J.B. Goodenough, “Phospho-olivines as positive-electrode materials for rechargeable lithium batteries,” *Journal of the Electrochemical Society*, 1997, vol. 144, pp. 1188–1194.

57. M.M Thackeray, W. David, P.G. Bruce, et al. “Lithium Insertion into Manganese Spinels,” *Materials Research Bulletin*, 1983, vol. 18(4), pp. 461–472.

58. http://www.nissanusa.com/electric-cars/leaf/

59. http://www.mitsubishicars.com/imiev/specifications

60. http://www.ford.com/cars/focus/trim/electric/

61. https://www.hyundaiusa.com/sonata-hybrid/

62. https://www.teslamotors.com/cn/models

63. http://mobile.autonet.com.tw/cgi-bin/file_view.cgi?b1120348111214

64. J. S. Newman. Electrochemical Systems, Second edition, Englewood Cliffs: *Prentice-Hall*, 1991.

65. T. Fuller, M. Doyle, J. Newman, “Simulation and optimization of the dual lithium ion insertion cell,” *Journal of the Electrochemical Society*, vol. 141, pp. 1–10.

66. M. Doyle, T. Fuller, J. Newman, “Importance of the lithium ion transference number in lithium/polymer cells,” *Electrochimica Acta*, vol. 39, pp. 2073–2081.

67. T. Fuller, M. Doyle, J. Newman, “Relaxation phenomena in lithium-ion-insertion cells,” *Journal of the Electrochemical Society*, vol. 141, pp. 982–990.

68. C. Y. Wang, V. Srinivasan, “Computational battery dynamics (CBD)-electrochemical/thermal coupled modeling and multi-scale modeling,” *Journal of Power Sources*, vol. 110, pp. 364–376.

69. M. Doyle, Y. Fuentes, “Computer simulations of a lithium-ion polymer battery and implications for higher capacity next-generation battery designs,” *Journal of the Electrochemical Society*, vol. 150, pp. 706–713.

70. V. R. Subramanian, V. Boovaragavan, V. Ramadesigan, M. Arabandi, “Mathematical model reformulation for lithium-Ion battery simulations: Galvanostatic Boundary Conditions,” *Journal of the Electrochemical Society*, vol. 156, pp. 260–271.

71. J. P. Wang, Q. S. Chen, B. G. Cao, “Support vector machine based battery model for electric vehicles,” *Energy Conversion and Management*, vol. 47, pp. 858–864.

72. J. P. Wang, L. Xu, J. G. Guo, L. Ding, “Modelling of a battery pack for electric vehicles using a stochastic fuzzy neural network,” *Journal of Automobile Engineering*, vol. 223, pp. 27–35.

73. M. Chen, G. A. Rincon-Mora, “Accurate electrical battery model capable of predicting runtime and I-V performance,” *IEEE Transactions on Energy Conversion*, vol. 21, pp. 504–511.

74. G. L. Plett, “Extended Kalman filtering for battery management systems of LiPB-based HEV battery packs, Part 2. Modeling and identification,” *Journal of Power Sources*, vol. 134, pp. 262–276.

75. C. Weng, Y. Cui, J. Sun, H. Peng. “On-board state of health monitoring of lithium-ion batteries using incremental capacity analysis with support vector regression,” *Journal of Power Sources*, vol. 235, pp.36–44.

76. A.A. Hussein, “Capacity fade estimation in electric vehicles Li-ion batteries using artificial neural networks,” *Energy Conversion Congress and Exposition (ECCE)*, 2013 IEEE, pp. 677 – 681.

77. W. He, N. Williard, M. Osterman, M. Pecht, “Prognostics of lithium-ion batteries based on Dempster–Shafer theory and the Bayesian Monte Carlo method,” *Journal of Power Sources*, vol. 196, pp. 10314–10321.

78. Y. Ji, Y. Zhang and C. Wang, “Li-Ion Cell Operation at Low Temperatures,” *Journal of the Electrochemical Society*, vol. 160, pp. 636–649.

79. N. Sato, “Thermal behavior analysis of lithium-ion batteries for electric and hybrid vehicles,” *Journal of Power Sources*, vol. 99, pp. 70–77.

80. J. Yi, U.S. Kim, C.B. Shin, T. Han, S. Park, “Modeling the temperature dependence of the discharge behavior of a lithium-ion battery in low environmental temperature,” *Journal of Power Sources*, vol. 244, pp. 143–148.

81. S.S. Zhang, K. Xu, T.R. Jow, “The low temperature performance of Li-ion batteries,” *Journal of Power Sources*, vol. 115, pp. 137–140.

82. C. R. Gould, C. M. Bingham, D. A. Stone, P. Bentley, “Novel battery model of an all-electric personal rapid transit vehicle to determine state-of-health through subspace parameter estimation and a Kalman Estimator,” *International Symposium on Power Electronics, Electrical Drives, Automation and Motion*, 2008, pp. 1217–1222.